Iranian Journal of Materials Science and Engineering

VOLUME 14 / NUMBER 2 / June 2017

Published four times a year for The Iran University of Science and Technology (IUST), Iranian Metallurgical Society (IMS) and Iranian Ceramic Society (ICerS).

ICerS IUST IMS

[DOI: 10.22068/ijmse.14.2.41]

IRANIAN JOURNAL OF MATERIALS SCIENCE & ENGINEERING

Licence Holder:
The Vice-Chancellery for Research and Technology, Iran University of Science and Technology, Tehran, Iran

[DOI: 10.22068/ijmse.14.2.41]

IRANIAN JOURNAL OF MATERIALS SCIENCE & ENGINEERING

Published four times a year by the Iran University of Science and Technology (IUST), Iranian Metallurgical Society (IMS) and Iranian Ceramic Society (ICerS).

Submissions:

Authors should submit their papers online to: http://ijmse.iust.ac.ir. [Instructions to authors appear regularly on the inside back cover and are available on the IJMSE website].

Address: IJMSE Office, Iran University of Science and Technology, Narmak 16844, Tehran, Iran.
Tel: +98-21-77240274
Fax: +98-21-77240276
Email: ijmse@iust.ac.ir
Web site: http://ijmse.iust.ac.ir

[DOI: 10.22068/ijmse.14.2.41]

Volume 14 Number 2 June 2017

Contents:

[DOI: 10.22068/ijmse.14.2.41]

Experimental and Theoretical Study of the Structural, Magnetic and Electronic Properties of the Ba_2GdSbO_6 Perovskite

R. Moreno Mendoza, D. A. Landínez Téllez, R. Cardona, L. A. Carrero Bermúdez and J. Roa-Rojas*

* *jroar@unal.edu.co*

Received: April 2016 Accepted: April 2017

Grupo de Física de Nuevos Materiales, Departamento de Física, Universidad Nacional de Colombia, Bogotá D.C., AA 5997, Colombia.

DOI: 10.22068/ijmse.14.2.1

Abstract: *In this work the procedure to the synthesis of Ba_2GdSbO_6 complex perovskite by the solid-state reaction method is reported. Theoretically a study of the crystalline and electronic structure was performed into the framework of the Density Functional Theory (DFT). The most stable structure is obtained to be a rhombohedral perovskite with a lattice constant a=6,0840 Å. Due the occurrence of a mean energy gap of 2,84 eV close to the Fermi level for both up and down spin polarizations this material is classifies as insulator. The effective magnetic moment of material obtained from the calculations was 7,0 μ_B. The crystalline structure was analyzed through the X-ray diffraction technique and Rietveld refinement of the experimental data. Results are strongly in agreement with those theoretically predicted. Magnetic response was studied from measurements of magnetic susceptibility as a function of temperature. Results reveal the paramagnetic feature of this material in the temperature regime from 50 K up to 300 K. From the fitting with the Curie law the effective magnetic moment was obtained to be 8,1 μ_B, which is slightly higher that the theoretical value for the Gd^{3+} isolated cation predicted by the theory of paramagnetism. The energy gap obtained from experiments of diffuse reflectance is relatively in agreement with the theoretical predictions. The dielectric constant as a function of applied frequencies at room temperature was measured. Results reveal a decreasing behavior with a high value of dielectric constant at low applied frequencies.*

Keywords: *Perovskite Material, Structure, Magnetic Feature, Electronic Properties*

1. INTRODUCTION

Recently, there has been a great interest in the electronic oxide ceramics oxides with ABO_3 perovskite structure due to the chemical versatility to evaluate different combinations of transition metal cation in the B site and obtain a variety of magnetic and electric properties [1, 2]. Ideally, a simple ABO_3 perovskite possesses a 3-dimensional cubic network of BO_6 octahedra with the cation A into the void formed by eight octahedral with AO_{12} coordination [3]. If the A and B sites contain a mixture of cations, distorted complex perovskites structures with lower symmetries are obtained. Distortions are mainly related with octahedral tilting due to a small cation driving a rotating of octahedral respect the crystallographic axes. Other kind of distortion is the cation displacement caused through first and second-order Jahn-Teller effects. Specially, the 1:1 B-site based class with chemical formula $A_2BB'O_6$ (or double perovskites) is the most frequently complex perovskite encountered [4]. From the distortions and composition of the double perovskites, new properties and applications are found in ferroelectric devices with large dielectric constants and frequency dispersion [5], magnetoresistance [6], solar energy conversion [7], catalysis [8], solid-oxide fuel cells [9] and microwave resonator [10]. In this paper we propose the synthesis and characterization of Ba_2GdSbO_6 ceramic material. We describe the crystalline structure of this double perovskite and perform morphological and compositional analyses. Furthermore, we present results of measurements of the magnetic response as a function of temperature. Moreover, considering that in recent years the density functional theory (DFT) has constituted in a strong tool to study electronic properties in

[DOI: 10.22068/ijmse.14.2.41]

perovskite-like material [11], we carried out a study of the electronic properties of these materials, in order to establish the type of hybridization between the orbitals of GdO_6 and SbO_6 octahedra present in the structure.

2. EXPERIMENTAL

Samples were synthesized through the standard solid-state reaction recipe. Precursor powders of Gd_2O_3, Sb_2O_5 and Ba_2CO_3 (Aldrich 99.9%) were stoichiometrically mixed according to the chemical formula Ba_2GdSbO_6. Mixture was ground to form a pellet and annealed at 1000 ºC for 30 h. The samples were then regrinded, repelletized and sintered at 1100 ºC for 40 h and 1200 ºC for 40 h. X-ray diffraction (XRD) experiments were performed by means of a PW1710 diffractometer with λ_{CuK}=1,54064 Å. Rietveld refinement of the diffraction patterns was carried out by the GSAS program [12]. Morphological studies were performed by means scanning electron microscopy (SEM) experiments through the utilization of VEGA 3 equipment, and chemical composition of samples was analyzed by energy dispersive X-ray (EDX) technique. Field cooling measurements of the magnetic susceptibility as a function of temperature were carried out by using an MPMS Quantum Design SQUID. Diffuse reflectance experiments were performed by using a VARIAN Cary 5000 UV-Vis-NIR spectrophotometer, which has an integration sphere with a PMT/Pbs detector. The relative dielectric constant was measured by using an Agilent HP4194A-350 frequency analyzer.

3. CALCULATION METHOD

In order to determine the electronic and band structures we applied the Full-Potential Linear Augmented Plane Wave method (FP-LAPW) within the framework of the Kohn-Sham Density Functional Theory (DFT) [13], and adopted the Generalized Gradient (GGA) approximation for the exchange-correlation energy due to Perdew, Burke and Ernzerhof [14]. The self-consistent process is developed by the numeric package Wien2k [13]. Taking the experimental unit cell data as input, the structure studied in this work were fully relaxed with respect to their lattice parameters and the internal degrees of freedom compatible with the space group symmetry of the crystal structure. The resulting energies versus volume functions have been fitted to the equation of state due to Murnaghan [15] in order to obtain de minimum energy value, the bulk modulus, its pressure derivative and the equilibrium lattice parameters and associated volume. The muffin-tin radiuses used for Ba_2GdSbO_6 were 2,20; 2,50; 2,12 and 1,82 Bohr for Ba, Gd, Sb and O respectively, angular momentum up to l = 10 inside the muffin-tin sphere, a maximum vector in the reciprocal space of Gmáx=12,0; $RMT*K_{max}$ = 7,0 and a mesh of 1000 points in the first Brillouin zone (equivalent to a maximum of 250 k points in the irreducible Brillouin zone). Finally, the convergence criterion for the self-consistent calculation was 0,0001 Ry for the total energies, 0,0001 Bohr in the charge and 1,0 mRy/u.a in the internal forces. Spin polarization was included in the calculations.

4. RESULTS AND DISCUSSION

Figure 1 shows the XRD patterns obtained for Ba_2GdSbO_6. In the picture black symbols represent the experimental data and line corresponds to simulated pattern by means of GSAS code. Base line is the difference between theoretical and experimental results. Refinement parameters of figure 1 were x^2=5,236, $R_{(F2)}$=5,84%. From the Rietveld refinement it was established that these materials crystallize in a rhombohedral perovskite structure, space group R-3 (#148). The structural parameter obtained from the refinement was a=5,9882(1) Å. These results are 99,3% in agreement with the theoretical values obtained from the Structure Prediction Diagnostic Software SPuDS [16], which predicts a=6,0293 Å and α=57,8634º. In these ceramic materials the explanation of distortion from the ideal cubic perovskite structure is clear because the double perovskite have the generic formula $A_2BB'O_6$, and for this type of material the tolerance factor τ, is

[DOI: 10.22068/ijmse.14.2.41]

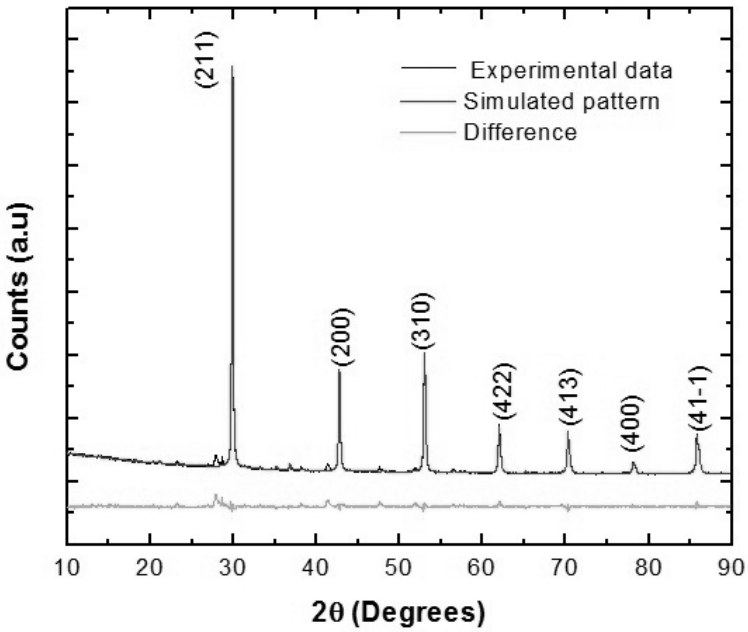

Fig. 1. Characteristic XRD pattern for the Ba2GdSbO6 double perovskite. Black symbols represent experimental diffraction data, continuous lines are the simulated patterns and base line is the difference between experimental and calculated values.

calculated by the ratio $\tau = \frac{r_A + r_o}{\sqrt{2}\left(\frac{r_B + r_{B'}}{2} + r_o\right)}$, where r_A, r_B, $r_{B'}$ and r_o are the ionic radii of the A, B, B', and O ions, respectively.

If τ is equal to unity, there is ideal cubic perovskite structure, and if τ<1 the structures is distorted from the cubic symmetry. The value of tolerance factor obtained for the complex perovskite was 0,9081. The Wyckoff positions obtained from the refinement analysis are presented in table 1.

From the structural analysis above, the expected structure of the Ba_2GdSbO_6 complex perovskite is that presented in figure 2. Clearly, a tolerance factor as far from the ideal value is related to distortions from the cubic cell. As showed in figures 2a and 2b, there is a difference between directions of the GdO_6 and SbO_6 octahedra. The most important has to do with the nature of the rhombohedral structure, since the trigonal angle α=60,0290º is quite far from 90o degrees corresponding to the ideal cubic cell. Furthermore, the tilt of the GdO_6 and SbO_6 octahedra occurs out of phase for an angle β=-16,4650º, corresponding to the Glazer notation a−a−a−, whose symmetry involves reflections, signaling odd-odd-odd reflections, which is characterized by cationic ordering and simple

Table 1. Atomic positions of cations and anions on the unit cell for Ba2GdSbO6.

Atom	Wyckoff Site	*x*	*y*	*z*
Ba	*2c*	0,2500	0,2500	0,2500
Gd	*1a*	0,0000	0,0000	0,0000
Sb	*1a*	0,5000	0,5000	0,5000
O1	*6f*	-0,1771	-0,3613	0,2705

[DOI: 10.22068/ijmse.14.2.41]

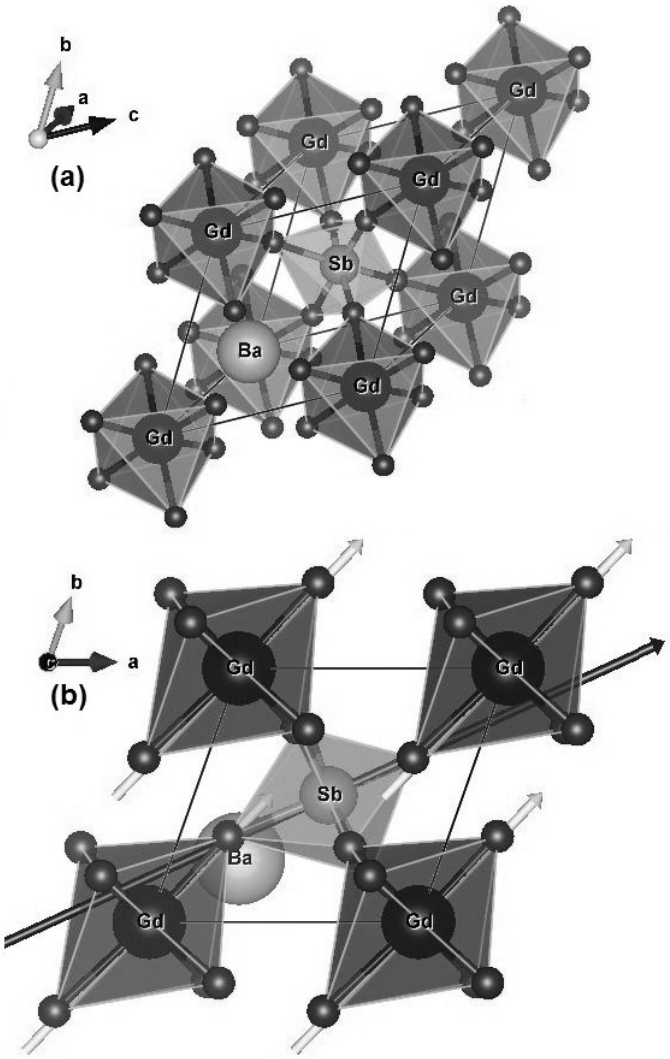

Fig. 2. (a) Characteristic cell and (b) GdO_6 and SbO_6 octahedra in the ab-plane for trigonal structure of the Ba2GdSbO6 double perovskite

octahedral tilting.

SEM images of the material shown in figure 3 reveal a qualitative approximation to the surface microstructure. In picture (a) evidences the formation of clusters of polyhedral grains and interstitial particulate grains. From picture (b) it is clear that the grains could end up having a few tens of nm, forming groups, which have appearance of clusters of several μm sizes.

By applying the EDX microprobe of the VEGA3 TESCAN microscope, the percentages of the constituent elements of the material were obtained, as reported in table 2. These values confirm that the material does not contain other elements than those corresponding to the expected stoichiometry Ba_2GdSbO_6. However, the experimental result reveals an apparent low content of the oxygen anion against an increase in the percentage of Ba, Gd and Sb cations, which may be because the resolution of the device is slightly affected because oxygen is a very light element compared to the other constituents of the compound.

Measurements of magnetic susceptibility as a

[DOI: 10.22068/ijmse.14.2.41]

Table 2. Compositional percentages of elements for Ba2GdSbO6 obtained from EDX.

Element	*Theoretical %*	*Experimental %*
Ba	42,28	43,33
Gd	24,20	24,81
Sb	18,74	19,10
O	14,78	12,76

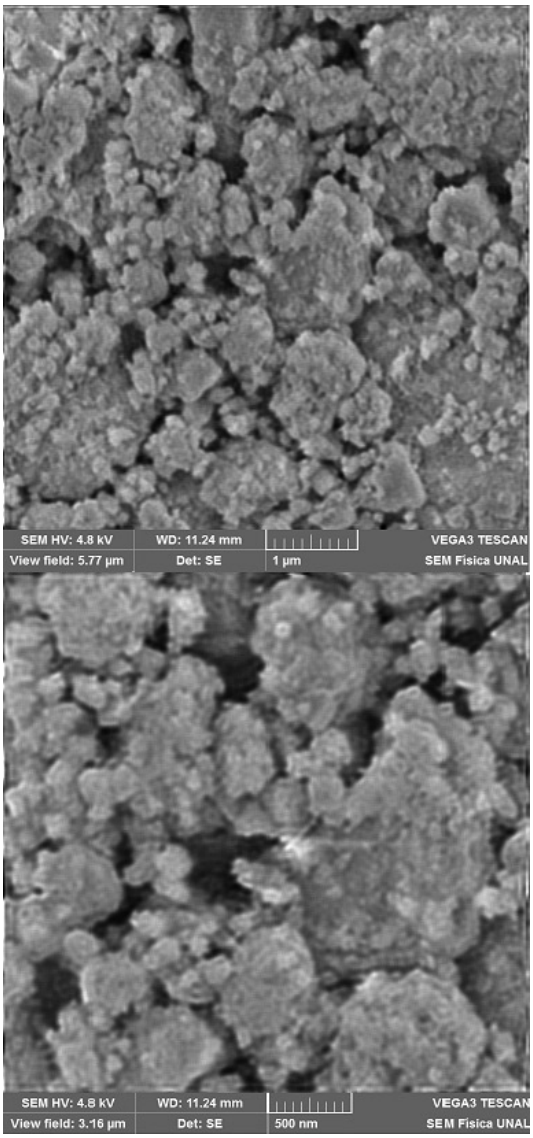

Fig. 3. Granular topology of the surface obtained from SEM images for the Ba_2GdSbO_6 perovskite-like material

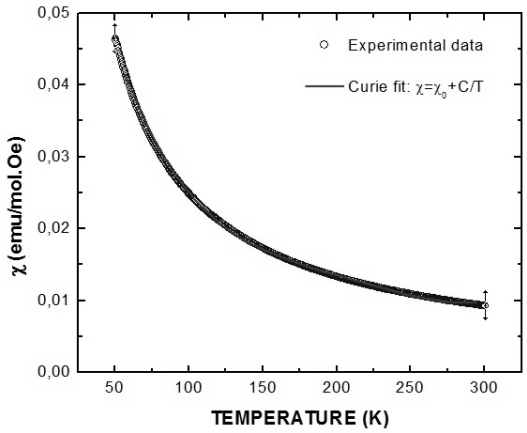

Fig. 4. Magnetic behaviour of Ba_2GdSbO_6 material obtained from measurements of susceptibility as a function of temperature. Red line corresponds to the fit with the Curie law.

function of temperature reveal the paramagnetic character of the Ba_2GdSbO_6 complex perovskite. Figure 4 shows the Curie fitting performed following the equation $X=X_0+(C/T)$. In the Curie equation, $C=N\mu^2_{eff}/3K_B$ is the Curie constant, N is Avogadros's number, μ_{eff} is the effective magnetic moment ($\mu_{eff}=P_{eff}\mu_B$), P_{eff} represent the effective Bohr magneton number, μ_B is the Bohr magneton, K_B is the Boltzmann constant and x_0=0,00139 emu/mol is the temperature independent susceptibility term. From the Curie constant C the effective magnetic moments for Ba_2GdSbO_6 material was calculated to be 8,1 μ_B. This value is 98% in agreement with the theoretical expected moments obtained from the Hund's rules [19]. The difference is attributed to other magnetic effects due to the hybridization of

[DOI: 10.22068/ijmse.14.2.41]

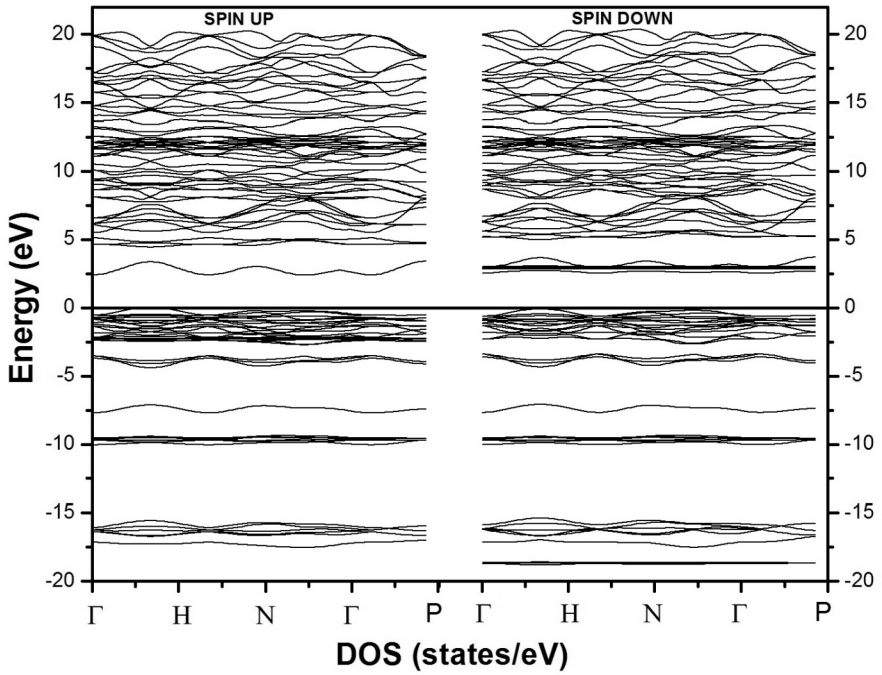

Fig. 5. Spin polarized band structure for the Ba_2GdSbO_6 double perovskite.

the d-Sb and f-Gd orbital and non-preferential spin orientations in the GdO_6 and SbO_6 octahedra due structural distortions.

In order to obtain the most accurate result, the optimal lattice parameter corresponding to the minimal energy value was calculated as the total energy versus volume. The total energy was calculated by fittings with the Murnaghan's state equation [15]. From total energy as a function of volume the ideal lattice parameter was determined to be a=6,0840 Å. Figure 5 shows the band structure for both up and down spin polarizations. In the picture, E=0 eV corresponds to the Fermi level. It is observed that these materials evidence weak semiconductor behavior with gap energy through the Fermi level from -0,05 eV up to 2,81 eV (width 2,86 eV) for the spin up polarization and between -0,05 eV and 2,78 eV (width 2,83 eV) for the spin down orientation.

The Partial Densities of States (DOS) for the Ba_2GdSbO_6 complex perovskite are exemplified in figure 6. As in the figure 5, the energy zero corresponds to the Fermi level reference. It is important to elucidate that close the Fermi level there are contributions due to the O-2p hybridizations but Gd-4f spin up orbitals are responsible for priority contributions. Very incipient contributions of Sb-3d states are observed. This behavior can be clearly seen in Figures 5 and 6 in the energy range between -2,87 and -0,05 eV. Localized states attributed to Sb-3d, Ba-6s and O-2p appear far the Fermi level, below – 3,00 eV. On the other hand, in the conduction band, it is observed in figures 5 and 6 that available states are majority due to the Gd-4f spin down orbitals with very small contributions of the Sb-3d and O-2p spin up and down levels.

The magnetic moment of mixed charge density was calculated to be 7,0 μ_B for Ba_2GdSbO_6. This value is relatively different from the value obtained experimentally. However, an important element to be taken into account has to do with the clutter of Gd and Sb cations in the structure of the double perovskite, which can not only distorted octahedra but also modify the magnetic response of the material.

Results of diffuse reflectance experiments are shown in figure 7. Reflectance values were acquired at 1 nm intervals over the 300–2500 nm,

[DOI: 10.22068/ijmse.14.2.41]

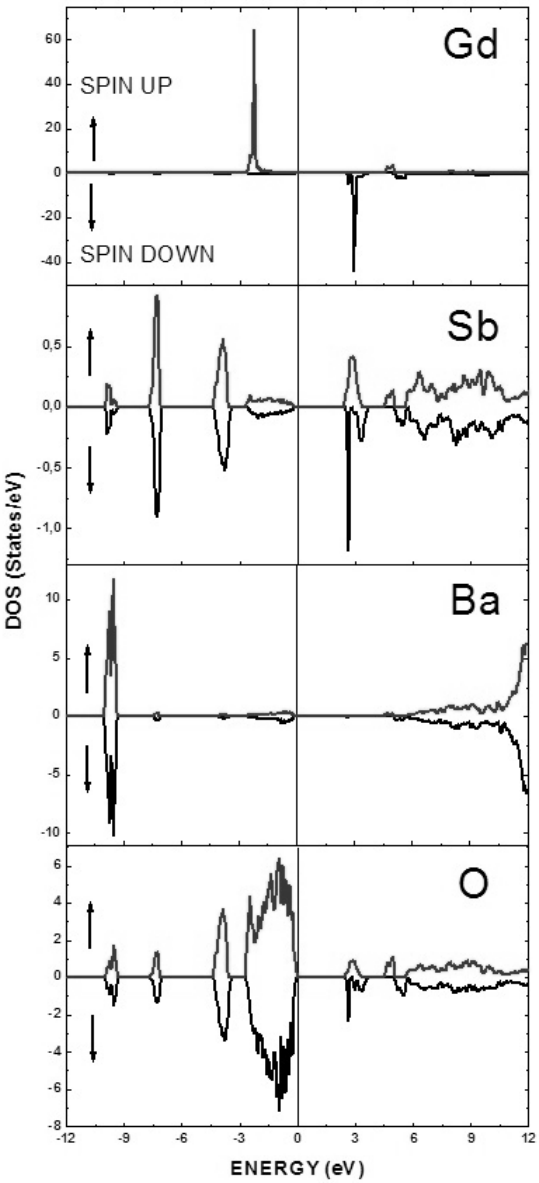

Fig. 6. Partial DOS with spin up and down polarizations for the Ba_2GdSbO_6 double perovskite.

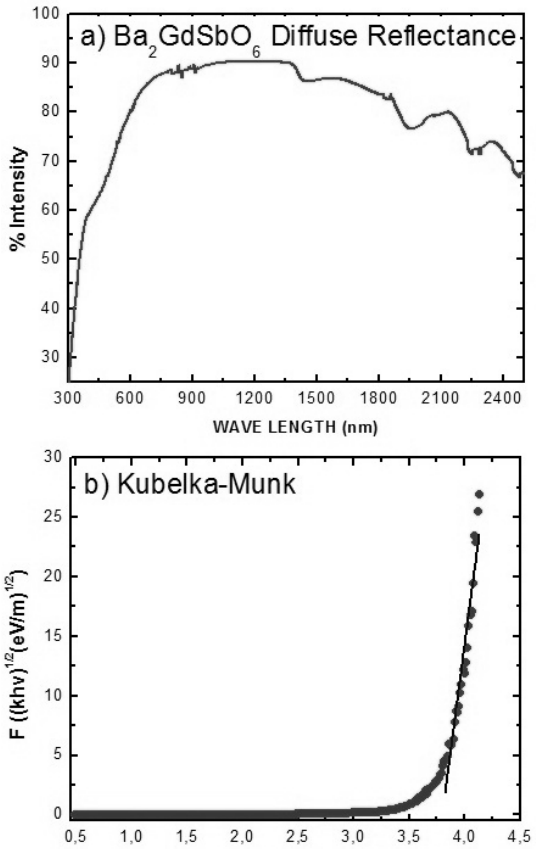

Fig. 7. a) Diffuse reflectance results for the Ba2GdSbO6 material. b) Kubelka–Munk fit.

as shown in figure 7a. The absorption of UV-Vis-NIR radiation reveals that the molecules of the Ba_2GdSbO_6 material cause the excitation of electrons from the ground state to exited state, which produces electronic jumps between quantum levels. The quantum characteristics energy, which depends from the electronic configuration, is calculated from the radiated energy. By applying the Kubelta-Munk model, currently used to the measurement of the band gap in powder samples, the respective band gap for the Ba_2GdSbO_6 perovskite is obtained as showed in figure 7b. Structural defects or vacancies can produce spontaneous absorption that appears for several wavelengths, as observed in figure 7a.

From the adjustment to the Kubelka–Munk equation it was determined that the energy gap of the Ba_2GdSbO_6 is 3,61 eV at room temperature, which is 33% different of the theoretic prediction given by the DOS calculations for T=0 K. This difference occurs because in the DFT calculations, the exchange and correlation potential by Perdew, Burke and Ernzerhof [14] gives a very good approximation for the valence and conduction density of states, but is not very accurate for determining the energy gap in

[DOI: 10.22068/ijmse.14.2.41]

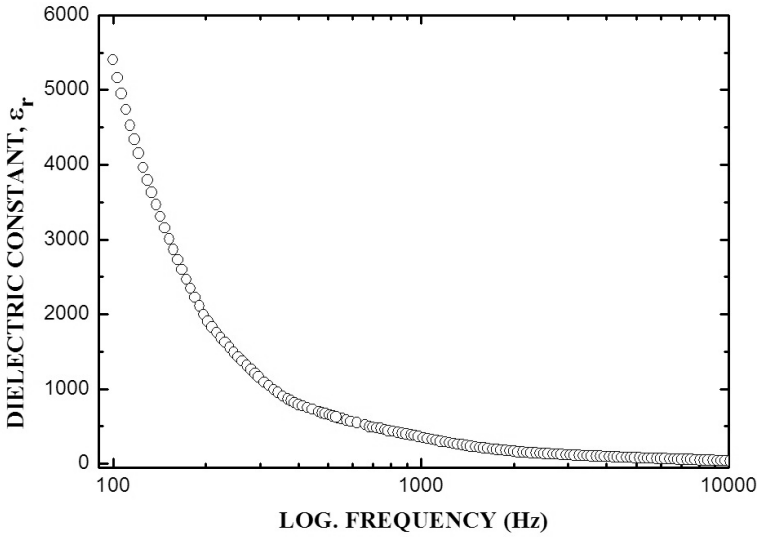

Fig. 8. Dielectric constant as a function frequency measured for the Ba_2GdSbO_6 perovskite.

semiconductors due to self-interaction errors [18-19], for which it would be more interesting to use a potential specifically designed for this purpose, that uses local functional without Hartree-Fock exchange [20-21].

The dielectric characteristics of this compound were obtained from measurements of the dielectric constant as a function of frequency performed. The corresponding results are shown in figure 8. As shown in the picture, at low frequencies (ν=100 Hz) the value of the dielectric constant ε_r=5400, which is a tendency of the giant-dielectric materials [22]. The value of the dielectric constant decreases dramatically with increasing frequency between 100 Hz and 1000 Hz. Above ν=1000 Hz, the dielectric constant decreases smoothly to the value ε_r=40 at ν=10 kHz. There are reports according to which it is expected that most giant dielectric constants are due interconnected effects of polarization [23]. In semiconductors, for example, the formation of Schottky barriers at the contacts could lead to depletion regimes. Another example has to do with the formation of internal barrier layer capacitors through grain boundaries, which produce relaxations Maxwell-Wagner type, resulting in very high dielectric constant [24]. It is not excluded that the behavior of the dielectric constant depending on the frequency has to do with the occurrence of relaxation processes attributed to hopping of oxygen O^{2-} ions and $(O2)^{2-}$ peroxide between multiple off-center sites of the crystal [22].

5. CONCLUSIONS

The Ba_2GdSbO_6 complex has been synthesized by the solid-state reaction procedure. A study of the crystalline and electronic structure was performed through the Linearized Augmented Plane Wave method (FP-LAPW) into the framework of the Density Functional Theory (DFT). The results reveal that a rhombohedral perovskite is the more stable structure with a lattice parameter a=6,0840 Å. Close to the Fermi level a mean energy gap of 2,84 eV was observed for both up and down spin polarizations, which permitted to classify this material as insulator. The largest contribution to the effective magnetic moment, due to the Gd^{3+} cations, evidenced a value of 7,0 μ_B. The crystalline structure was experimentally determined by means measurements in a Panalytical XPert Pro X-ray diffractometer with a Rietveld refinement of the diffraction pattern through de GSAS code. The experimental lattice parameter a=5,9882(1) Å is 98,4% in agreement with those theoretically predicted. Measurements

[DOI: 10.22068/ijmse.14.2.41]

of magnetic susceptibility as a function of temperature reveal the paramagnetic feature of this material. From the fitting with the Curie law the effective magnetic moment was obtained to be 8,1μ_B, which is slightly higher that the theoretical value for the Gd^{3+} isolated cation predicted by $\mu_{eff}=g[J(J+1)^{½}$, where g represents the Landé's factor and J is the quantic number related to the 4f electronic orbital. Experiments of diffuse reflectance and fittings with the Kubelka–Munk equation permitted to obtain an energy gap of 3,61 eV, which differs 33% when compared with the theoretical value predicted by DFT. This difference is attributed to the temperature effect.

ACKNOWLEDGEMENTS

This work was partially supported by DIB, Universidad Nacional de Colombia.

REFERENCES

1. Corredor, L. T., Roa-Rojas, J., Landínez Téllez, D. A., Beltrán, R., Pureur, P., Mesquita, F., Albino Aguiar, J., "Magnetic and structural properties of the new double perovskite family $Sr_2GdRu1-xRexOy$", J. Appl. Phys. 2013, 113, 17E302-17E305.
2. Llamosa, D. P., Landínez Téllez, D. A., Roa-Rojas, J., "Magnetic and structural behavior of Sr_2ZrMnO_6 double perovskite Physica B", 2009, 404, 2726-2729.
3. Macquart, R. B., Zhou, Q. D., Kennedy, B. J., Structural investigation of Sr_2LiReO_6. Evidence for a continuous tetragonal–cubic phase transition", Journal of Solid State Chem., 2009, 182, 1691-1693.
4. Glazer, A. M., "The classification of tilted octahedra in perovskites", Acta Crystallogr. Sect. B, 1972, 28, 3384-3392.
5. Glazer, A. M., "Simple ways of determining perovskite structures", Acta Crystallogr. Sect. A, 1975, 31, 756-762.
6. Woodward, P. M., "Octahedral Tilting in Perovskites I. Geometrical Considerations", Acta Crystallogr. Sect. B, 1997, 53, 32-43.
7. Howard, C. J., Kennedy, B. J., Woodward, P. M., "Structures of ordered double perovskites: A group theoretical analysis", Acta Crystallogr. B, 2003, 59, 463-471.
8. Wakeshima, M., Harada, D., Hinatsu, Y., Crystal structures and magnetic properties of ordered perovskites $A_2R_3+Ir_5+O_6$ (A=Sr, Ba; R=Sc, Y, La, Lu), J. Alloy and Compd., 1999, 287, 130-136.
9. Wakeshima, M., Harada, D., Hinatsu, Y., Masaki, N., "Magnetic Properties of Ordered Perovskites Ba_2LnIrO_6 (Ln=Sm, Eu, Gd, and Yb)", J. Solid State Chem. 1999, 147, 618-623.
10. Wakeshima, M., Harada, D., Hinatsu, Y., "Crystal structures and magnetic properties of ordered perovskites Ba_2LnIrO_6 (Ln = lanthanide)", J. Mater. Chem. 2000, 10, 419-422.
11. Cardona, R., Landínez Téllez, D. A., Arbey Rodríguez M., J., Fajardo, F., Roa-Rojas, J., "Structural and magnetic properties of double-perovskite Ba_2MnMoO_6 by density functional theory", J. Magn. Magn. Mater. 2008, 320, e85-e87.
12. Larson, A. C., von Dreele, R. B., "General Structure Analysis System (GSAS)", Los Alamos National Laboratory Report LAUR, 2000, pp. 86-748.
13. Blaha, P., Schwarz, K., Madsen, G. K. H., Kvasnicka, D., Luitz, J., "WIEN2k, an Augmented Plane Wave + Local Orbitals Program for Calculating Crystal Properties. Karlheinz Schwarz", Techn. Universität Wien, Vienna, 2001. ISBN 3-9501031-1-2.
14. Perdew, J. P., Burke, S., Ernzerhof, M., "Generalized Gradient Approximation Made Simple", Phys. Rev. Let. 1996, 77, 3865-3868.
15. Murnaghan, F. D., "The Compressibility of Media under Extreme Pressures", Proc. Natl. Acad. Sci., USA., 1944, 30, 244-247.
16. Lufaso, M. W., Woodward, P. M., "Prediction of the crystal structures of perovskites using the software program SPuDS", Structural Science, 2001, 57, 725-738.
17. Cullity, B. D., Graham, C. D., "Introduction to Magnetic Materials", 2nd Ed., IEEE Press, NJ, 2009.
18. Einollahzadeh, H., Dariani, R. S., Fazeli, S. M., "Computing the band structure and energy gap of penta-graphene by using DFT and G0W0 approximations", Solid State Commun. 2016,

[DOI: 10.22068/ijmse.14.2.41]

229, 1-4.

19. Zhao, Y., Truhlar, D. G., "Calculation of semiconductor band gaps with the M06-L density functional", J. of Chem. Phys. 2009, 130, 74103(1-3).
20. T. Higuchi, T. Tsukamoto, N. Sata, M. Ishigame, Y. Tezuka, S. Shin, "Electronic structure of p-type $SrTiO_3$ by photoemission spectroscopy", Phys. Rev. B, 1998, 57, 6978-6983.
21. N. Kulagin, J. Dojcilovic, D. Popovic, "Low-Temperature dielectric properties of doped $SrTiO_3$ single crystals and valency of ions", Cryogenics, 2001, 41, 745-750.
22. Lunkenheimer, P., Götzfried, T., Fichtl, R., Weber, S., Rudolf, T., Loidl, A., Reller, A., Ebbinghaus, S. G., "Apparent giant dielectric constants, dielectric relaxation, and ac-conductivity of hexagonal perovskites $La_{1.2}Sr_{2.7}BO_{7.33}$ (B=Ru, Ir)", J. of Solid State Chem. 2006, 179, 3965-3973.
23. Lunkenheimer, P., Fichtl, R., Ebbinghaus, S. G., Loidl, A., "Nonintrinsic origin of the colossal dielectric constants in $CaCu_3Ti_4O12$", Phys. Rev. B, 2004, 70, 172102.
24. Sinclair, D. C., Adams, T. B., Morrison, F. D., West, A. R., "$CaCu_3Ti_4O_{12}$ One-Step Internal Barrier Layer Capacitor", Appl. Phys. Lett., 2002, 80, 2153-2155.

[DOI: 10.22068/ijmse.14.2.41]

The Effects of Plasma Spray Parameters on the Microstracture and Phase Composition of Thermal Barrier Coatings Made by SPPS Process

Z. Valefi* **and M. Saremi**

* *ziavalefi@ut.ac.ir*

Received: April 2016 **Accepted: April 2017**

[1] Maleke Ashtar University of Technology, Tehran, Iran.

[2] Department of Metallurgy and Materials, Faculty of Engineering, University of Tehran, Tehran, Iran.

DOI: 10.22068/ijmse.14.2.11

Abstract: *In this paper the effect of plasma spray parameters, atomizing gas and substrate preheat temperature on microstructure and phase composition of YSZ coatings produced by SPPS process have been investigated. The experimental results showed that increasing the power of plasma, using hydrogen as the precursor atomizing gas and increasing substrate preheat temperature decrease the amount of non-pyrolyzed precursor in the coatings. At low plasma power most of the deposited precursor is in non-pyrolyzed state, and consequently the applied coatings are defective. The increase in substrate temperature beyond 800 °C either by preheating or heat transfer from plasma torch to the substrate, prevent the coating formation. In SPPS coating formation, up to a special spray distance the optical microscopy image of the coatings showed a snowy like appearance. XRD analysis showed that in this situation the amount of un-pyrolyzed precursor is low. Beyond this spray distance spherical particles are obtained and XRD analysis showed that most of the precursor is in un-pyrolyzed state.*

Keywords: *Thermal Barrier Coatings, Solution Precursor plasma Spray, Precursor Atomizing, Ytrria Stabilized Zirconia*

1. INTRODUCTION

Thermal barrier coatings (TBCs) have been widely used in various gas turbines for aircraft propulsion, power generation, and marine propulsion [1–4]. Current TBCs are made by air plasma spray (APS) or electron beam physical vapor deposition (EB-PVD) processes. More recently, a solution precursor plasma spray (SPPS) process has been developed to deposit various ceramic coatings [5–10]. TBCs made by this process have demonstrated improved durability over a range of TBC thicknesses [11], due to their unique microstructure.

It is widely recognized that deposition of small, melted particles achieves a fine microstructure, which in turn leads to improvements in certain desirable mechanical properties such as strength and hardness of the coatings. Unfortunately, it is generally not possible to feed powders finer than 5-10 μm to plasma torch due to the effects of surface forces on powder flow. Recently, the suspension plasma spray process (SPS) was developed to overcome this limitation [12-14]. In this process, nano-sized particles are suspended in a liquid before injection into the plasma plume, circumventing normal feeding problems.

In SPPS process an atomizer nozzle injects the solution of final material precursor into the plasma flame. The precursor usually used for YSZ TBCs, is an aqueous solution containing zirconium and yttrium salts. As with suspension, the liquid undergoes rapid fragmentation and evaporation once injected in the plasma jet. This is followed by precipitation or gelation, pyrolysis and melting to result droplets with average diameters ranging from 0.1 to a few micrometers [15–17].

Three major zones can be identified within the plasma flow:

- The plasma jet core (T>8000 K) where the liquid can encounter the highest heat and momentum transfers,
- The plasma plume (3000<T<6000 K) where the heat and momentum capabilities from the plasma are drastically reduced

[DOI: 10.22068/ijmse.14.2.41]

compared to the ones in the plasma core,
- The plasma fringe (around the plasma core) where the momentum might be high enough to fragment the liquid

The droplet momentum and injection location determine which area of the plasma plume a droplet will entrain and this in turn determines the thermal, or time-temperature, history of that droplet. Also spray parameters determine heat transfer to the atomized droplet. Substrate temperature affects pyrolyzis reactions on the surface of coatings. Since the chemical and physical processes that a droplet undergoes are dependent on the heating that it experiences, the deposition state of the coating is a direct function of this thermal history. Once entrained, a droplet undergoes some or all of the following processes depending on the amount of heat transferred to it from the plasma: precursor solvent evaporation, droplet breakup, precursor solute precipitation, pyrolysis, sintering, melting, and crystallization [18].

In this paper the effect of plasma spray parameters, atomizing gas and substrate preheat temperature on microstructure and phase composition of TBCs applied by SPPS process have been studied.

2. EXPERIMENTAL PROCEDURE

2. 1. Materials Used

An aqueous saturated solution containing zirconium oxy-nitrate and yttrium nitrate salts was used as precursor. The amounts of these salts in the solution were considered to result 93 wt% ZrO_2 and 7 wt% Y_2O_3 in the coating. To make saturated solution, the calculated amounts of $ZrO(NO_3)_2$ and $Y(NO_3)_3.6H_2O$ were added to 500 cm^3 distilled water at 50 ºC while mixing with a magnet. At first the salts dissolve in water and a colorless solution results. Then the salts start to deposit that show a super saturated solution has been made which was used as solution precursor.

The substrates were stainless steel type AISI 420 disks of 25 mm diameter and 10 mm thickness. The specimens after roughening by grit blasting with alumina grits mesh 36 were coated with MCrAlY alloy (Amdry 962) as bond coat by atmospheric plasma spray method (Sulzer-Metco F4 gun) to reach the thickness of 80-100 µm. Spray parameters are shown in table 1. These specimens then were coated to a thickness of 200 µm by SPPS method.

2. 2. Processing

The coatings were applied using F4 plasma spray torch (Sulzer-Metco). To inject solution precursor into the plasma jet, an atomizer suitable to be mounted on this torch was made. The nozzle diameter of the atomizer was 0.3 mm. Two kinds of atomizing gas were used; O_2 with flow rate of 6 slpm and H_2 with flow rates of 6 and 8 slpm. To reduce the danger of using H_2 as atomizing gas, two flash back arrestors after the regulator and before the atomizer have been used. The pressure of atomizing gas (H_2 or O_2) was 3.5 bar adjusted on the exit of the gas regulator. The flow rate of the atomizing gas was adjusted by a ball flowmeter. Solution precursor flow rate of 30 cm^3/min at spray distances of 4 to 20 cm were used.

Two plasma powers of 18.5 and 34.5 KW and three substrate preheating temperatures of 200, 500 and 800ºC were studied. The spray parameters are summarized in table 2. To study the effect of spray distance on coatings morphology, a specimen holder schematically shown in Fig. 1 was used. Ten specimens with 2 cm distances related to each other can be mounted on this holder. The vertical traverse speed for plasma gun was 5 cm/s and after each

Table1. Spray parameters of depositing bond coat by APS

Ar (slpm)	H_2 (slpm)	Current (A)	Voltage	Injector diameter (mm)	Injector angle (degree)	Injector distance (mm)	Powder gas Ar (slpm)	Powder feed rate (g/min)	Spray distance (mm)
65	14	600	75	1.5	90	6	2.3	40	140

[DOI: 10.22068/ijmse.14.2.41]

Table 2. Spray parameters used in this study

Experiment number	Current (A)	Plasma gas Ar (slpm)	Plasma gas H_2 (slpm)	Power (KW)	Atomizing gas	Atomizing gas flow rate at pressure 3.5 bar (slpm)	Substrate preheat Temp. (°C)
1	300	35	8	18.5	O_2	6	200
2	600	35	12	34.5	O_2	6	200
3	600	35	12	34.5	H_2	6	200
4	600	35	12	34.5	H_2	8	200
5	600	35	12	34.5	O_2	6	500
6	600	35	12	34.5	H_2	6	500
7	600	35	12	34.5	O_2	6	800
8	600	35	12	34.5	H_2	6	800

pass of plasma gun, a horizontal displacement of 5 mm of specimen holder caused all surfaces of the specimens to be coated. The coating process proceeded till the thickness of 250±50 μm was attained. The specimens with lower spray distances because of higher spray efficiency gain the mentioned thickness earlier than specimens with higher spray distance so they discharged from the fixture earlier than the specimens with higher spray distance.

2. 3. Characterization

The surface morphology of deposits were characterized by light and Scanning Electron Microscope (SEM). To determine the phase composition of coatings XRD test (Cu K-radiation; D5005, Bruker AXS, Karlsruhe, Germany) was used. The temperatures of specimens were measured by an optical pyrometer.

To study the thermal shock resistance of coatings, the coated specimens were held in a box furnace at 900 °C for 10 min and then quenched to room temperature water. After 500 thermal cycles the surface of coatings were studied by optical microscope.

3. RESULTS

3. 1. Characterization of Solution Precursor

To determine the phases resulted from pyrolysis reactions by XRD analysis, some of the solution precursor was heated at 550 °C for 5 hours and the resulted material was grinded to result a powder in the range of 20-45 μm. Fig. 2

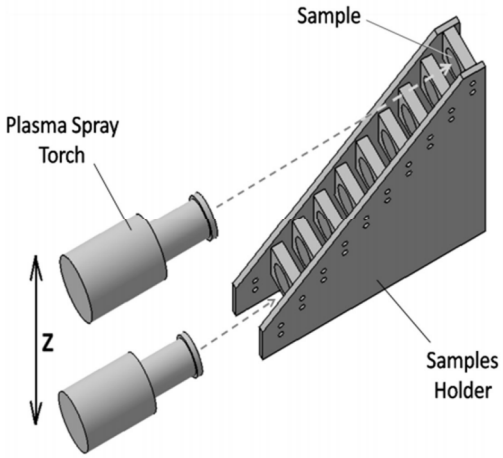

Fig. 1. Specimens mounted on fixture at distances of 2 cm related to each other.

[DOI: 10.22068/ijmse.14.2.41]

shows the result of XRD analysis. According to the work of Chen [19] it can be seen that the powder is mainly composed of stabilized Zirconia. This also can be recognized from the XRD PDF file number 81-1544 [20]. The background of XRD peaks shows that some precursor still is in un-pyrolyzed state. Recognition of Y_2O_3 peaks was not possible because Y_2O_3 is expected to be doped inside ZrO_2 crystal structure.

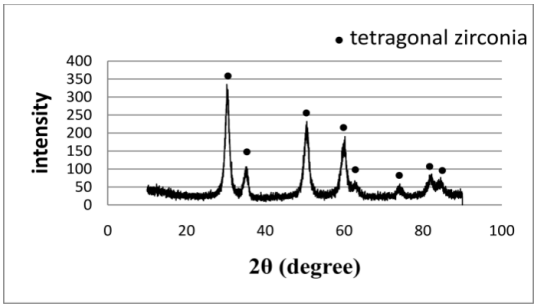

Fig. 2. XRD analysis of solution precursor pyrolyzed at 600 ºC.

3. 2. Optical Microscope Images of the Coatings Surface

Fig. 3 shows the optical microscope images from the surface of coatings deposited by the parameters of test 1 in Table 1 at spray distances 4 to 20 cm. It can be seen that coating deposited at spray distance 4 cm contains cracks and is defective. At spray distance of 6 cm these cracks are not observed and again at spray distances 8 to 18 cm these cracks appear. The amount of cracking is low at spray distances up to 10 cm and is increased at higher spray distances up to 16

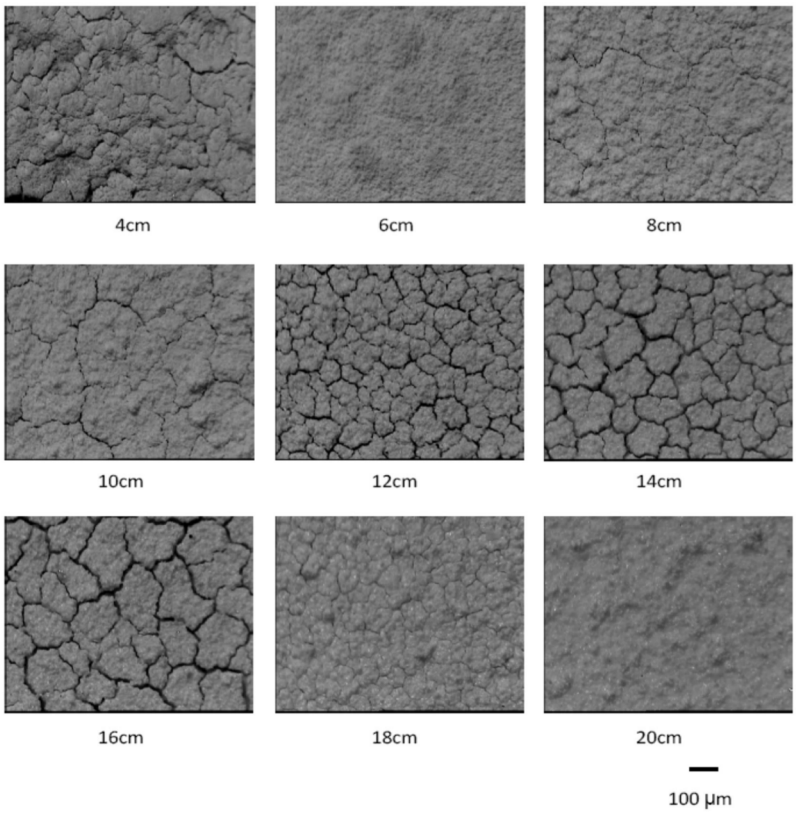

Fig. 3. Optical microscopy images from the surface of coatings produced under condition of test 1 at spray distances of 4 to 20cm (×100).

[DOI: 10.22068/ijmse.14.2.41]

cm while decreased again at spray distance of 18 cm. No crack was observed at spray distances more than 18 cm.

To explain this observation it should be considered that evaporation of solute and pyrolysis of precursor can be done in two steps; the first step occurs when the atomized precursor is injected into the plasma jet. At this step depending on injection and atomizing conditions, some of the solution enters the hot zone of the plasma jet in which it will breakup to fine particles and then the pyrolysis, crystallization and melting can occur [21]. The remaining part enters the lower temperature zone of plasma in which the evaporation of precursor solute or pyrolysis reactions may not be done completely. At the second step depending on preheating temperature of substrate and the heat transferred from plasma torch to substrate solute evaporation or pyrolysis reactions can be occurred on the substrate. Obviously by decreasing the spray distance more heat transfers to the substrate and these reactions will be done severely.

In the condition of test 1, in which the power of plasma is low, complete evaporation and pyrolyzation of the solution precursor would not occur.

It seems that at spray distance of 4 cm there is not enough time for complete evaporation of precursor solute while reaching the surface of substrate. So the mud-flat cracks observed in coatings are due to rapid evaporation of precursor solute by high heat transfer from the plasma to the layers formed on the substrate.

Lack of cracks at spray distance of 6 cm proposes that the cracking seen at more spray distances should have another reason. Xie [22] showed that unpyrolyzed precursor starts to

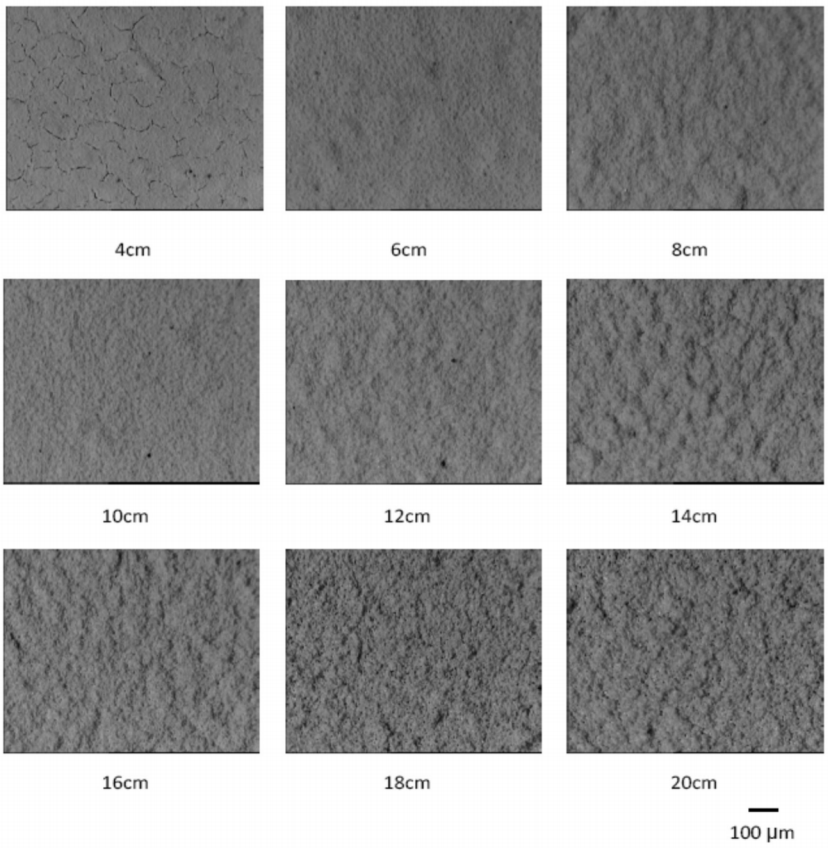

Fig. 4. Optical microscopy images from the surface of coatings produced under condition of test 2 at spray distances of 4 to 20cm (×100).

[DOI: 10.22068/ijmse.14.2.41]

decompose at temperatures above 350ºC. The decomposition of precursor causes contraction and tensile stresses which can cause cracking in the coating structure. Because of low plasma power used in test 1, much of the precursor remains unpyrolyzed and heat transferred from plasma torch to the layers already formed on substrate causes pyrolyzation to occur and the resulted stresses cause cracking. Lack of cracking in coatings produced at spray distances of 20 cm and more shows that at these distances the heat transferred from plasma torch to substrate was not enough to cause pyrolyzation.

As mentioned earlier when the droplets enter the hot zone of the plasma core, they breakup to finer particles. Because of lower volume of these particles, the pyrolysis and crystallization reactions can occur to a large extent. By increasing the spray distance the percent of fine particles which reach the substrate and contribute to the coating structure decreases and the result will be increase in un-pyrolyzed precursor in the deposited coatings. Therefore more volume of the precursor undergoes pyrolyze reaction and the cracking will be more severe. This is the trend observed at spray distances up to 16 cm. At spray distance of 18 cm because heat transfer from plasma to substrate is low the pyrolyzation could not occur to a large extent and cracking is low. At higher spray distances no cracks are seen.

Another result from Fig. 3 is that up to spray distance of 10 cm the coatings have a snowy like structure but at spray distances above 10 cm the coatings are composed of sphere particles.

In Fig. 4 optical microscope images from the surface of coatings formed under the condition of test 2 are shown. In this case also the coating formed at spray distance of 4 cm is defective while at other spray distances no cracks are observed. The reason may be the more heat transferred to both atomized precursor and layers formed on substrate because of higher plasma power used in this test which reduces the amount of un-pyrolized precursor. Consequently the tensile stress resulted from pyrolyzation of precursor will be lower. Another observation from Fig. 4 is that up to spray distances 14 cm the coatings has a snowy like appearance and at higher spray distances coatings are composed of spherical particles.

Fig. 5 shows the optical microscope images from the surface of coatings formed under the

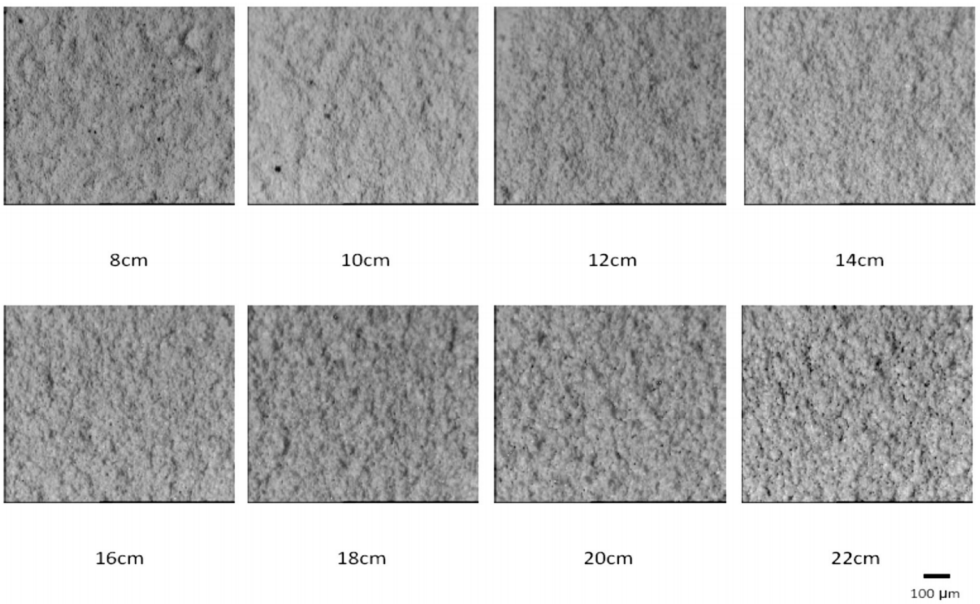

Fig. 5. Optical microscopy images from the surface of coatings produced under condition of test 3 at spray distances of 8 to 22cm (×100).

[DOI: 10.22068/ijmse.14.2.41]

condition of test 3. It can be seen that at all spray distances the coatings are crack free. This demonstrates the presence of low amount of unpyrolyzed precursor in coating structure because of using H_2 as the atomizing gas which increases the enthalpy of plasma and transfers more heat to atomized precursor and layers formed on substrate. Also up to spray distance 16 cm coatings have a snowy like appearance.

The coatings formed under the condition of test 4, similar to coatings of test 3, show no cracking but the snowy like appearance is observed at spray distances lower than 18 cm.

In Fig. 6 the optical microscope images from the surface of coatings formed under the condition of test 5 are shown. By preheating the substrate up to 500 ºC no cracks were observed in the structure at all spray distances. It seems that some of the unpyrolyzed precursors reaching the high temperature substrate surface, pyrolyze immediately and the amount of unpyrolyzed precursor in the coating structure, which during the subsequent passes of plasma torch undergoes pyrolyzation, is not enough to cause cracking in the coatings. Also up to spray distance of 18 cm coatings have a snowy like appearance. At spray distances lower than 12 cm deposit formation was not possible. Measuring the substrate temperature at this condition showed that the substrate temperature have been raised up to 800ºC and it seems that the resulted radiation prevents coating formation. This situation also encountered in conditions of tests 6-8 in which coatings formation were not possible.

3. 3. XRD Results

To determine the crystal structure of the coatings, XRD tests were done on the coatings produced under the conditions of test 2 at spray distances 6 and 16 cm and on coating produced under the condition of test 3 at spray distance of 6 cm. The results are shown in Fig. 7. The coatings are mainly composed of stabilized

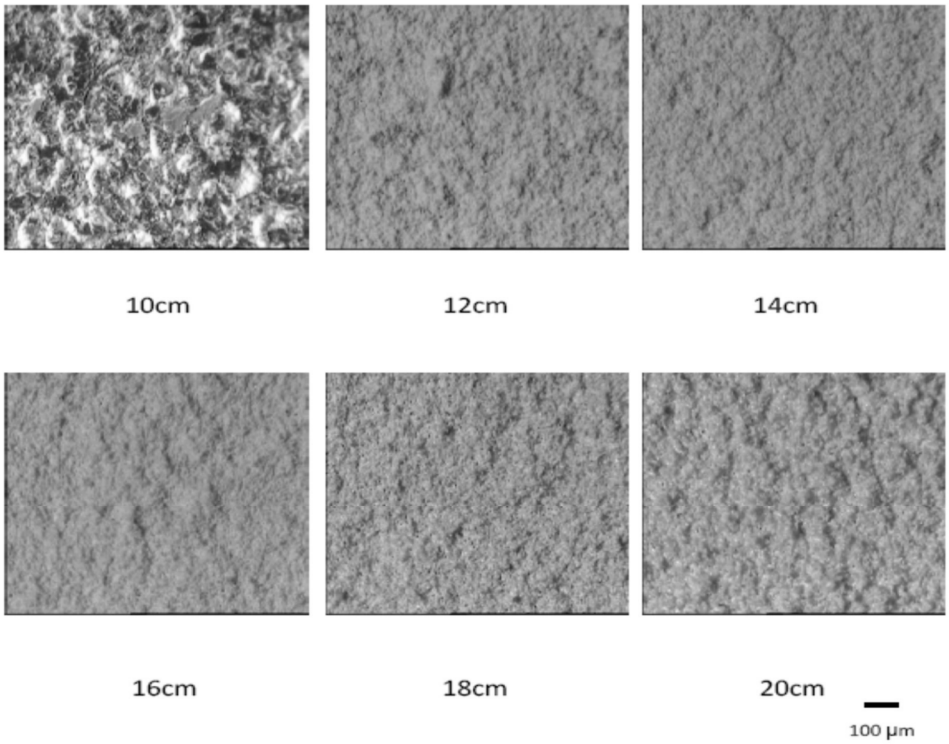

Fig. 6. Optical microscopy images from the surface of coatings produced under condition of test 5 at spray distances of 10 to 20cm (×100).

[DOI: 10.22068/ijmse.14.2.41]

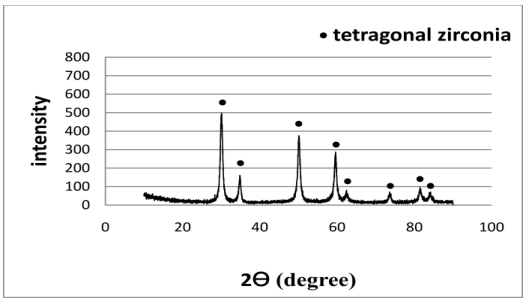

Fig. 7 a

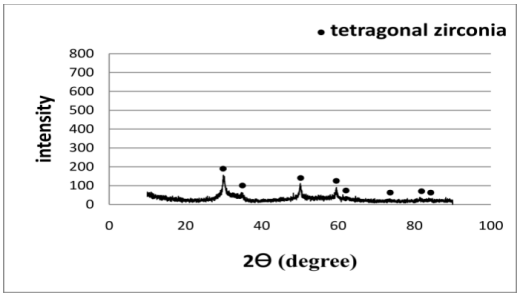

Fig. 7 b

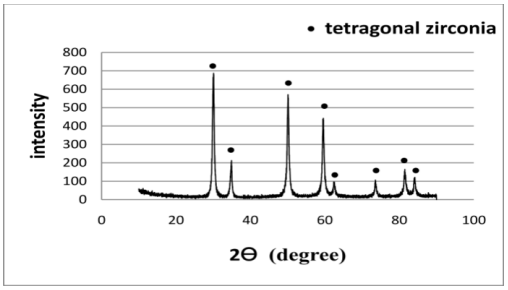

Fig. 7 c

Fig. 7. Results of XRD test for coatings produced under the condition of test 2 at spray distances of 6cm (a) and 16cm (b) and coating produced under the condition of test 3 at spray distance of 6cm (c).

tetragonal Zirconia. Comparing Fig. 7(a) and Fig. 7(b) shows that the amount of tetragonal phase in coatings formed at spray distance of 6 cm is more than spray distance of 16 cm in which the background peak shows the presence of a lot of amorphous phase due to unpyrolyzed precursor. It seems that at spray distance of 6 cm the heat transferred from the plasma to the coatings already formed, is more than spray distance of 16cm and this can increase the pyrolysis reactions and crystallization on the substrate. Also from Fig. 7(c) it can be observed that the amount of crystallization when H_2 is used as the atomizing gas is higher than similar conditions but using O_2 as the atomizing gas. The reason can be higher enthalpy because of using H_2 atomizing gas which increases the pyrolyzation reactions and crystallization both in plasma and on the layers already deposited on substrate. By considering the results of XRD tests and optical microscope images, it can be concluded that the snowy like appearance of the coatings resembles atomized particles that undergo the pyrolysis and crystallization reactions to a large extent and spherical particles resemble atomized particles that do not get enough heat for pyrolyzation and crystallization. When the droplets enter the plasma jet, they undergo post injection breakup. Thus we can expect a combination of particles which reach the substrate surface in different conditions. By considering spherical particles with the size in the range of the atomized particles in the structure of coatings at high spray distances, it can be concluded that the part of the atomized particles that undergo the breakup process, do not reach the substrate at high spray distances.

By comparison of spray distances which form snowy like coatings, it can be concluded that by increasing the enthalpy of plasma, these distances shift to higher amounts. The results are shown in Table 3.

The results of XRD studies show that the final coatings contain large amounts of unpyrolyzed material, although the amount of it is lower for coatings produced by using H_2 atomizing gas. And this shows the merit of using H_2 atomizing gas. The completion of pyrolyzation can be done by a post heat treatment or during service at high temperature.

3. 4. SEM Results

Fig. 8 shows the SEM images from the section

[DOI: 10.22068/ijmse.14.2.41]

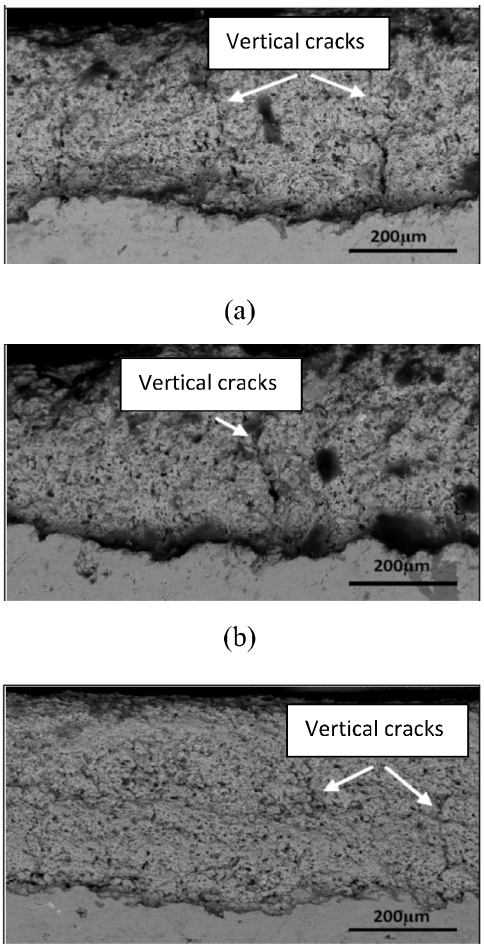

Fig. 8. SEM images from the section of coatings produced under the condition of test 2 at spray distances of 6 cm (a) and 16 cm (b) and test 3 at spray distance of 6 cm.

of coatings produced under the condition of test 2 at spray distances of 6 and 16 cm and test 3 at spray distance of 6 cm. In Fig.8 (a) vertical cracks, which are the characteristic of SPPS coatings, can be observed. Formation of these cracks has been studied by Xie [22]. He showed that the origin of cracks is pyrolyzation of the remained precursor in coatings as the result of heat transferred to the coating during coating build up from the plasma torch or subsequent exposure at high temperature service. These cracks are a positive characteristic of SPPS coatings because improve the thermal shock resistance of them.

In Fig. 8(b) it can be observed that coating formed at spray distance of 16 cm is less compact than spray distance of 6 cm. From table 3 it can be concluded that pyrolyzation hasn't been done to a large extent.

In Fig. 8(c) it can be seen that using H_2 atomizing gas resulted a more compact microstructure. Presence of vertical cracks in this case shows that in spite of higher enthalpy of plasma and heat transferred to the substrate, there is still unpyrolysed precursor in the coating.

Fig. 9 shows the SEM images from the surface of coating produced under the condition of test 2 at spray distance of 6 cm. The structure of coating mainly composes of splats, spherical particles with diameters in the range of less than 50 nm to more than 1000 nm and unpyrolyzed precursor. These particles are fractured atomized droplets

Table 3. Effect of plasma power, Substrate preheating temperature and Atomizing gas kind and flow rate on Spray distance that lower than it coatings have a snowy like appearance

Plasma power (KW)	Atomizing gas	Substrate preheating temperature (°C)	Atomizing gas flow rate at pressure of 3.5 bar (slpm)	Spray distance that lower than it coatings have a snowy like appearance (cm)
18.5	O_2	200	6	10
34.5	O_2	200	6	14
34.5	H_2	200	6	16
34.5	H_2	200	8	18
34.5	O_2	500	6	18

[DOI: 10.22068/ijmse.14.2.41]

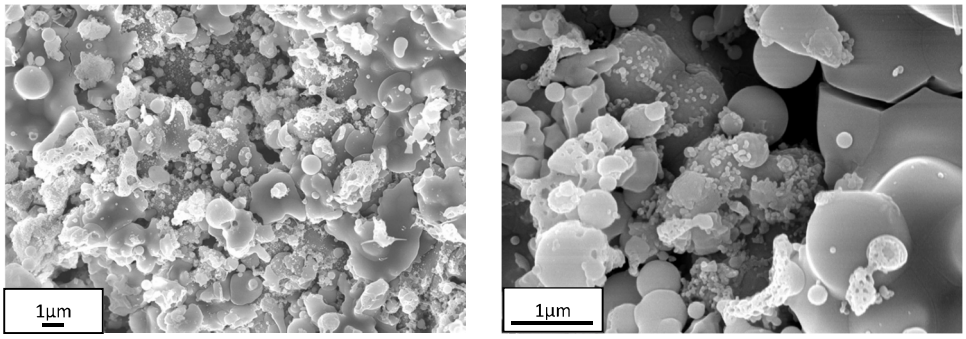

Fig. 9. SEM images of the surface of coating produced under the condition of test 2 at spray distance of 6cm.

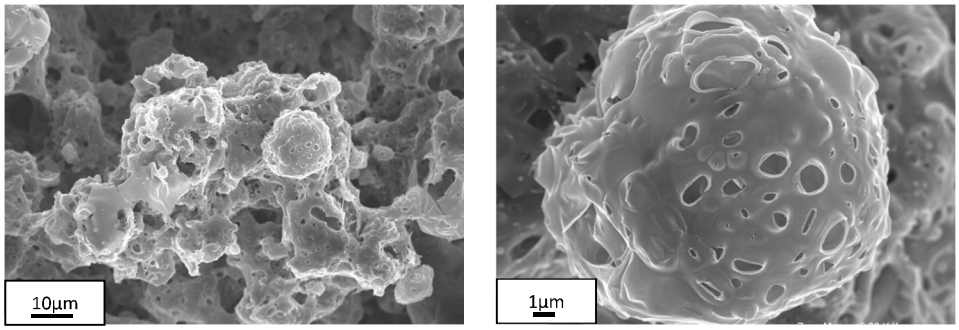

Fig. 10. SEM images of the surface of coating produced under the condition of test 2 at spray distance 16cm.

that solidified and crystallized before impact to the substrate. They adhere to the substrate after being captured by gel or softer deposit phases [21].

Fig.10 shows the surface of coatings produced under the condition of test 2 at spray distance of 16 cm. Spherical particles with diameter of 20 μm are seen in the microstructure which are the size of precursor atomized in the plasma jet. So it can be concluded that these particles did not undergo the breakup process in the plasma jet and entered the colder part of plasma plume. The particles that have entered the hot zone of plasma plume and undergo the breakup process do not reach the substrate surface at higher spray distance. For atomized particles that have entered the cold portion of plasma and have not undergo the breakup process there is not enough heat for pyrolyzation, crystallization and melting processes while such processes just start and occur on the surface of particles. The holes produced on the outer surface of spherical particles show that at first outer shell of the particles has been pyrolyzed and then evaporation of water content of un-pyrolyzed solution create the holes. Similar phenomena have been pointed out in some references [23-26]. These structural features are spherical particles appearance observed before in optical image microscopy and XRD of them seen in Fig. 7(c) showed a lot of unpyrolyzed precursor.

Fig. 11 shows the SEM image from the surface of the coating produced under the condition of test 3 at spray distance of 6 cm. The structure of this coating also composes of splats and particles with the diameter in the range of less than 500 nm to more than 1000 nm and by comparison with Fig. 9, it can be seen that the amount of

[DOI: 10.22068/ijmse.14.2.41]

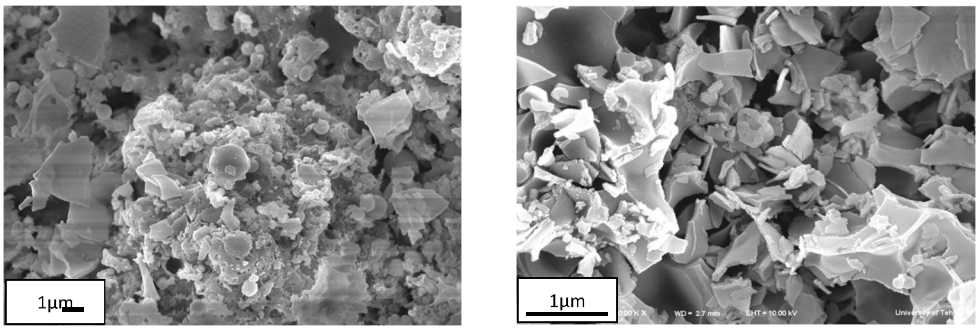

Fig. 11. SEM images of the surface of coating produced under the condition of test 3 at spray distance of 6cm.

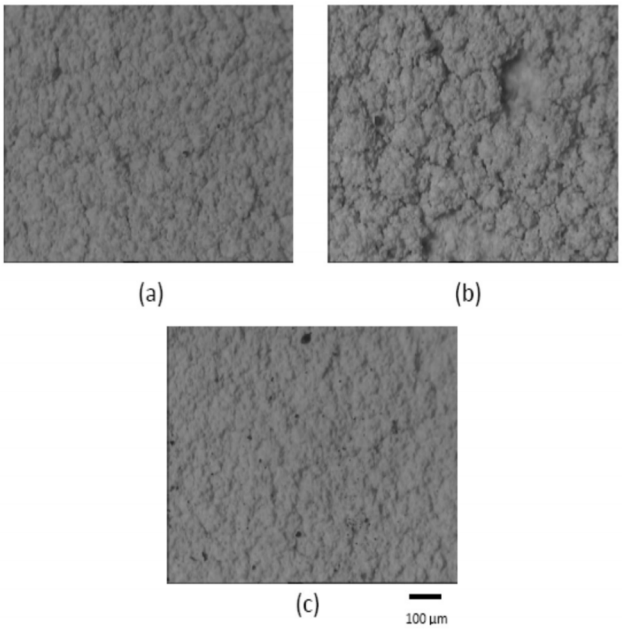

Fig. 12. Optical microscopy images from the surface of coated specimens under the conditions of (a) O2 atomizing at spray distance of 6 cm , (b) O2 atomizing at spray distance of 16 cm and (c) H2 atomizing at spray distance of 6 cm after 500 thermal cycles.

unpyrolyzed precursor and spherical particles are reduced and the amount of splats are increased.

3. 5. The Results of Thermal Cycle Resistance Test

After 500 thermal cycles the surfaces of the coatings produced under the conditions of test 2 at spray distances of 6 and 16 cm and test 3 at spray distance of 16 cm were examined by optical microscope. The results are shown in Fig. 12. In coating produced by O_2 atomizing at spray distance of 6 cm (Fig. 12 (a)), some cracks on the surface can be seen while for the coating produced by O_2 atomizing at spray distance of 16 cm (Fig. 12 (b)), spallation of the coating has been occurred. This result can be explained by too much unpyrolyzed precursor in coating produced at spray distance of 16 cm. Coating produced by H_2 atomizing at spray distance of 6 cm (Fig. 12 (c)) was sound after 500 thermal cycles. This result can be due to higher splat formation and lower unpyrolyzed precursor in this coating.

[DOI: 10.22068/ijmse.14.2.41]

4. CONCLUSION

The morphology of SPPS YSZ coatings depends on spray parameters specially plasma enthalpy. Increasing the power of plasma decreases the un-pyrolyzed precursor in coating structure. Using H_2 as the precursor atomizing gas by increasing the plasma temperature and enthalpy has the same effect. Successive passes of plasma torch transfer heat to coating already formed on the substrate and cause pyrolyzation of un-pyrolyzed precursor in the coating. This effect is severe at lower spray distances. Increasing the preheating temperature of substrate before applying the coating helps pyrolyzation to occur. Existence of too much un-pyrolyzed precursor in the coating can cause cracking due to pyrolyzation. Increasing the temperature of substrate more than about 800 °C prevent coating formation.

Using H_2 as the precursor atomizing gas, showed improvement in thermal shock resistance of coatings due to lower unpyrolyzed precursor and higher splat formation.

REFERENCES

1. Gleeson, B., "Thermal Barrier Coatings for Aeroengine applications", Journal of Propulsion and Power, 2006, Vol 22, 375-383.
2. Meier, S. M., Gupta, D. K. and Sheffler, K. D., "Ceramic Thermal. Barrier Coatings for Commercial Gas Turbine Engines", J. Met., 1991, Vol. 43, 50–53.
3. Jones, R. L., Stern, K. H., "Metallurgical and Ceramic Coatings, Chapman and Hall", London, 1996, 194.
4. Evans, A. G., Mumm, D. R., Hutchinson, J. W., Meier, G. H. and Pettit, F. S., "Mechanisms Controlling the Durability of Thermal Barrier Coatings", Progress in Materials Science, 2001, 46, 505-553.
5. Strutt, P. R., Kear, B. H. and Boland, R. F., "Method of Manufacture of Nanostructured Feeds," U.S. Patent Number 6025034, February 15, 2000.
6. Parukuttyamma, S. D., Margolis, J., Liu, H., Grey, C. P., Sampath, S., Herman, H., and Parise, J. B., "Yttrium Aluminum Garnet (YAG) Films Through a Precursor Plasma Spraying Technique", Journal of American Ceramic Society, 2001, 84/8, 1906-1908.
7. Padture, N. P., Schlichting, K. W., Bhatia, T., Ozturk, A., Cetegen, B., Jordan, E. H., Gell, M., Jiang, S., Xiao, T. D., Strutt, P. R., Garcia, E., Miranzo, P., Osendi, M. I., "Towards Durable Thermal Barrier Coatings with Novel Microstructures Deposited by Solution Precursor Plasma Spray", Acta Materialia, 2001, 49, 2251-2257.
8. Karthikeyan, J., Berndt, C. C., S. Reddy, Wang, J. Y., King, A. H., Herman, H., "Nanomaterial Deposits Formed by DC Plasma Spraying of Liquid Feedstocks", Journal American Ceramic Society, 1998, 81, 121-128.
9. Bhatia, T., Ozturk, A., Xie, L., Jordan, E., Cetegen, B., Gell, M., X. Ma, N. Padture, "Mechanisms of Ceramic Coating Deposition in Solution Precursor Spray", Journal of Material Research, 2001, 17, 2363-2372.
10. Bouyer, E., Schiller, G., Muller, M., Heane, R. H., "Thermal Plasma Chemical Vapor Deposition of Si-Based Ceramic Coatings from Liquid Precursors", Plasma Chemistry and Plasma Processing, 2001, 21/4, 523-546.
11. Jadhav, A., N., Padture, Wu, F., Jordan, E., Gell, M., "Thick Ceramic Thermal Barrier Coatings with High Durability Deposited Using Solution-Precursor Plasma Spray", Materials Science and Engineering A, 2005, 405, 313-320.
12. Bouyer, E., Gitzhofer, F., Boulos, M., "Progress in Plasma Processing of Materials", Ed. P. Fauchais, Begell House, NY, USA, 1997, 735–750.
13. Gitzhofer, F., Bonneau, M. E. and Boulos, M., "Thermal Spray 2001: New Surfaces For A New Millennium", Eds. C.C. Berndt, K.A. Khor, E. Lugscheider, ASM International, Materials Park, OH, USA, 2001, 61-68.
14. Fauchais, P., Rat, V., Delbos, C., Coudert, J. F., Chartier, T. and Bianchi, L., "Understanding of Suspension DC Plasma Spraying of Finely Structured Coatings for SOFC", IEEE. Transactions on Plasma Science, 2005, 33/2, 920-930.
15. Bhatia, T., Ozturk, A., Xie, L., Jordan, E., Cetegen, B., Gell, M., Ma, X. and Padture, N.,

[DOI: 10.22068/ijmse.14.2.41]

"Mechanisms of Ceramic Coating Deposition in Solution Precursor Spray", Journal of Material Research, 2001, 17, 2363-2372.

16. Xie, L., Ma, X., Jordan, E. H., Padture, N. P., Xiao, T. D., Gell, M., "Highly Durable Thermal Barrier Coatings Made by the Solution Precursor Plasma Spray Process", Surface and Coatings Technology, 2004, 177/178, 97-102.
17. Jordan, E. H., Xie, L. Ma, C., Gell, M., Padture, N., Cetegen, B., Roth, J., Xiao, T. D. and Bryant, P. E. C., "Superior Thermal Barrier Coatings Using Solution Precursor Plasma Spray", Journal of thermal spray, 2004, 13, 57-65.
18. Fauchais, P., Rat, V., Coudert, J. F., Etchart-Salas, R. and Montavon, G., "Operating Parameters for Suspension and Solution Plasma-Spray Coatings", Surface & Coatings Technology, 2008, 202, 4309–4317.
19. Chen, D., Gell, M., Jordan, E. H., Cao, E. and Ma, X., "Thermal Stability of Air Plasma Spray and Solution Precursor Plasma Spray Thermal Barrier Coatings", Journal of American Ceramic Society, 2007, 90/10, 3160-3166.
20. Martin, U., Boysen, H., Frey, F., "Acta Crystallogr", Sec. B: Structural Science, 1993, 49, 403.
21. Gell, M., Jordan, E. H., Teicholz, M., Cetegen, B. M., Padture, N. P., Xie, L., Chen, D., Ma, X. and Roth, J., "Thermal Barrier Coatings Made by the Solution Precursor Plasma Spray Process", Journal of Thermal Spray Technology, 2008, 17, 124-135.
22. Xie, L., Chen, D., Jordan, E. H., Ozturk, A., Wu, F., Ma, X., Cetegen, B. M. and Gell, M., "Formation of Vertical Cracks in Solution-Precursor Plasma-Sprayed Thermal Barrier Coatings", Surface and Coatings Technology, 2006, 201, 1058-1064.
23. Xie, L., Ma, X., Ozturk, A., Jordan, E. H., Padture, N. P., Cetegen, B. M., Xiao, D. T. and Gell, M., "The Effects of Processing Parameters on the Spray Patterns Produced in the Solution Precursor Plasma Spray of Thermal Barrier Coatings", Surface and Coatings Technology, 2004, 183, 51-61.
24. Xie, L., Ma, X., Jordan, E. H., Padture, N. P., Xiao, D. T. and Gell, M., "Deposition of Thermal Barrier Coatings Using Solution Precursor Plasma Spray Process", J. Mater. Sci., 2004, 39, 1639-1636.
25. Ozturk, A. and Cetegen, B. M., "Modeling of Axially and Transversely Injected Precursor Droplets into a Plasma Environment", International Journal of Heat and Mass Transfer, International Journal of Heat and Mass Transfer, 2005, 48, 4367–4383.
26. Ozturk, A. and Cetegen, B. M., "Modeling of Axial Injection of Ceramic Precursor Droplets into an Oxy-Acetylene Flame Environment", Mater. Sci. Eng. A, 2006, 422, 163-175.

[DOI: 10.22068/ijmse.14.2.41]

Diffusion Layer Growth Mechanism in ASPN Method Using an Iron Cage for St52 Steel

M. Kiani Salavat, M. Soltanieh* and M. Hasheminiasari

* *Mansour_soltanieh@iust.ac.ir*

Received: April 2016 Accepted: April 2017

Department of Materials and Metallurgical Engineering, Iran University of Science and Technology, Tehran, Iran.

DOI: 10.22068/ijmse.14.2.24

Abstract: *The mechanism of diffusion layer growth in plasma nitrided coatings applied on a St52 steel using an active screen is investigated. The nitriding was performed at 450,500 and 550 ◦C temperature nitriding times of 5, 10 and 15 h, in a gas mixture containing 20 vol. % H2: 80 vol. % N2 and DC-pulsed plasma nitriding unit.*
The surface, cross section and the thickness of diffusion of specimens was studied in terms of optical and scanning electron microscopy. According to the measurements of diffusion layer thickness, values of Q and D0 for nitrogen diffusion in substrate were calculated as 50585 (j/mol) and 4.11× 10-10 (m2/s)respectively. The variations of depth of hardness during nitriding period was determined.

Keywords: *plasma nitriding, AISI St52 tool steel, Diffusion zone, Growth mechanism, microhardness, Active Screen*

1. INTRODUCTION

Plasma nitriding process enhanced by an active screen is commonly used to improve steels, titanium alloys, aluminum alloys, polymers and ceramics corrosion behaviour and wear resistance [1-3]. In this process, problems of conventional plasma nitriding like the edge effect is completely omitted since the plasma is produced on the screen and not directly on the surface of sample[4,5].

During the plasma nitriding process of steels, the nitriding reaction takes place on the surface and in subsurface of substrate[6,7]. As a result, two different structures have been identified, the so-called white or compound layer and the diffusion zone. The outermost layer is compound layer, and consists of one or two kind of iron nitrides (Fe4N–Fe2–3N), depending on the process parameters. Below the white layer nitrogen atoms diffuses toward substrate which produces a diffusion zone [8-10].

In diffusion zone, the diffusion thickness, d, is defined as the depth, can be estimated as [12, 13]:

$$d = (De.t)1/2 \qquad \text{(Eq.1)}$$

Where De is the effective diffusion coefficient which depends on the diffusion and trapping (nitride formation) of N. The constant c in Eq. (1) takes into account the onset time of the nitriding process, and t is the treatment time.

The temperature dependence of the effective diffusion coefficient (Dk) can be approximately expressed in an Arrhenius form [11,14]:

$$Dk = Dk0 \exp(-Qk/RT) \qquad \text{(Eq.2)}$$

where Dk0 is so-called pre-exponential factor, Qk the activation energy for diffusion, R=8.3144 (Jmol-1K-1) the ideal gas constant, and T the absolute temperature. With c coefficient and De in Eq. (1) Dk0 and Qk for the diffusion of nitrogen in diffusion layer could be calculate[15,16].

In this study, the kinetics of diffusion layer produced by active screen plasma nitriding method on A St52 steel was determined. The effect of nitriding time and temperature on composition, structure and thickness of the nitrided layer was investigated by XRD optical (OM) and scanning electron microscope (SEM). The topographical evolution and surface

Table 1. Parameters related to screen and sample location

Screen Material	Screen diameter	Screen height	Screen hole diameter	Distance between screen holes	Distance between screen and sample edge	Distance between screen and sample
St 37	10 cm	10 cm	1 cm	1 cm	3 cm	7 cm

roughness were studied by atomic force microscopy (AFM). It was found that there is a correlation between these properties and nitriding of the samples.

2. EXPERIMENTAL PROCEDURE

A typical St52 boiler steel (chemical composition 0.27% C, 0.6% Mn, 0.18% Si, 0.2% Cr and 0.45% Cu, wt %) were used in this study. Chemical composition of steel was examined by quantometry analysis. Specimens were wire cut from the bars in the form of discs with 25 mm diameter and 10 mm height. All of the specimens were surface ground and polished using 60, 80, 120, 240, 400, 600, 800 and 1000 SiC grit and 0.5 μm alumina powder, respectively.

The polished specimens were placed on an insulated ceramic in an iron screen with 0.8 mm thickness, plasma nitrided in a pulsed DC plasma reactor. The plasma nitriding was performed with a 10 kHz frequency and 60% duty cycle at 450˚C, 500˚C and 550˚C for 5, 10 and 15 h. The process parameters used in the nitriding chamber are shown in Table 1.

X-ray diffraction (XRD) (Philips PW-1730), was used for phase composition analyze. VEGA II TESCAN scanning electron microscopy and optical microscopy (Carl-Zeiss, 4996387) used for cross sectional microstructure of coatings. Cross-sectional microhardness profiles were obtained on polished surfaces, using a Buehler microhardness tester equipped with a Vickers indenter applying 50g of load.

3. RESULTS AND DISCUSSION

The XRD patterns of the plasma nitrided samples treated at 450 ˚C, 500 ˚C and 550 ˚C for 10 h are shown in Fig. 1, which indicate that the compound layer consists of γ′ and ε iron nitrides. In general, increasing the treatment temperature resulted in an increase in the intensity of the γ′ and ε phases. This may be explained by the increase in the compound layer thickness for an increase in the treatment temperature. In fact at higher temperature more FexN particles would deposit from screen on the substrate surface

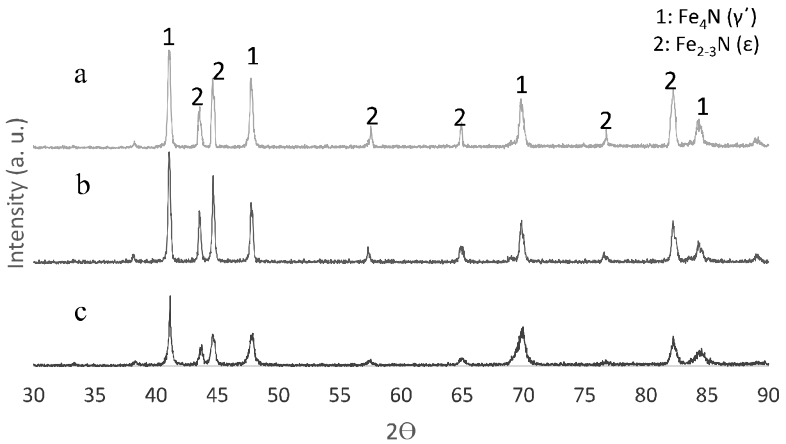

Fig.1. XRD patterns of active screen plasma nitrided samples for 10h and 450˚C (a), 500˚C (b) and 550˚C (c)

[DOI: 10.22068/ijmse.14.2.41]

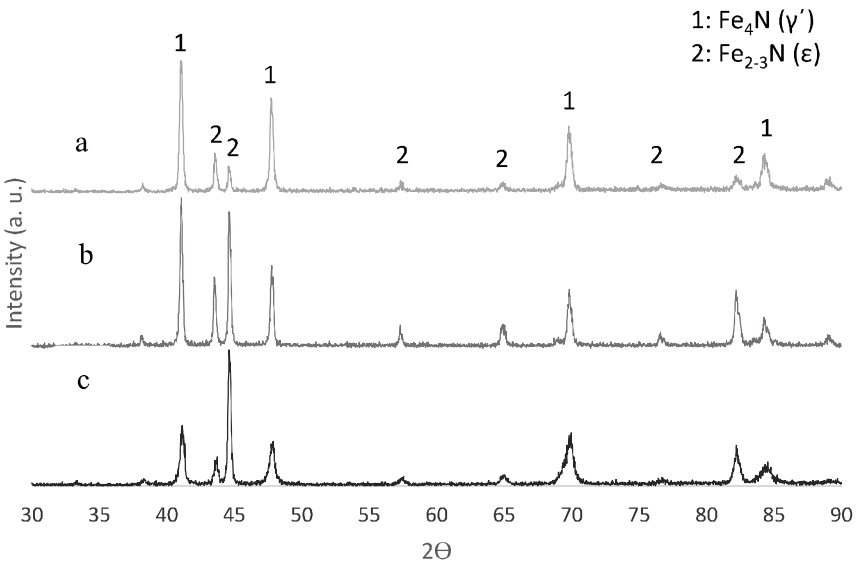

Fig. 2. XRD patterns of active screen plasma nitrided samples at 500˚C for 5h (a), 10h (b) and 15h (c)

which results more diffusion of nitrogen toward substrate. Fig. 2 shows effect of plasma nitriding time on iron nitrides peak intensity. It is clearly seen that intensity of γ′ phase increases due to decomposition of Fe2-3N to Fe4N at longer treatment time.

The sample cross-section after plasma nitriding using an active screen at a gas mixture of 20 % H2: 80 % N2 and a temperature of 500 ˚C for 10 h is presented in Fig. 3. A diffusion zone and compound layer present on the surface can be seen. Fig. 4 shows the results of the compound layer thickness as a function of treatment temperatures. Increasing temperature causes thicker compound layer. Growth of the compound layer is controlled by diffusion of nitrogen through this layer [17]. At low treatment temperature the diffusion coefficient of nitrogen atoms is low, therefore the compound layer and diffusion layer are thin. Increasing treatment temperature results in an increase in the nitrogen diffusivity, leading to the formation of thicker layers.

Thickness of layers assessed using OM and SEM cross sectional images are in Fig. 5. It is seen that by increasing the coating time, the thickness of the layers increases which is due to the growth of the iron nitride particles descending from the top screen. Similar results have been reported by other researchers [18]. One of the important properties of active screen plasma nitriding method is Enhancement of the coating

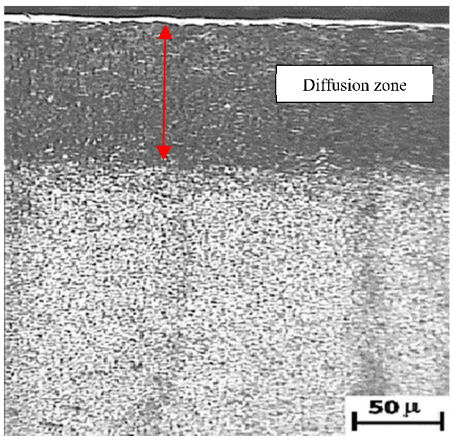

Fig. 3. Optical micrograph of typical specimen plasma nitrided at a gas mixture of 20 % H2: 80 % N2 at 500 ◦C for 10 h.

[DOI: 10.22068/ijmse.14.2.41]

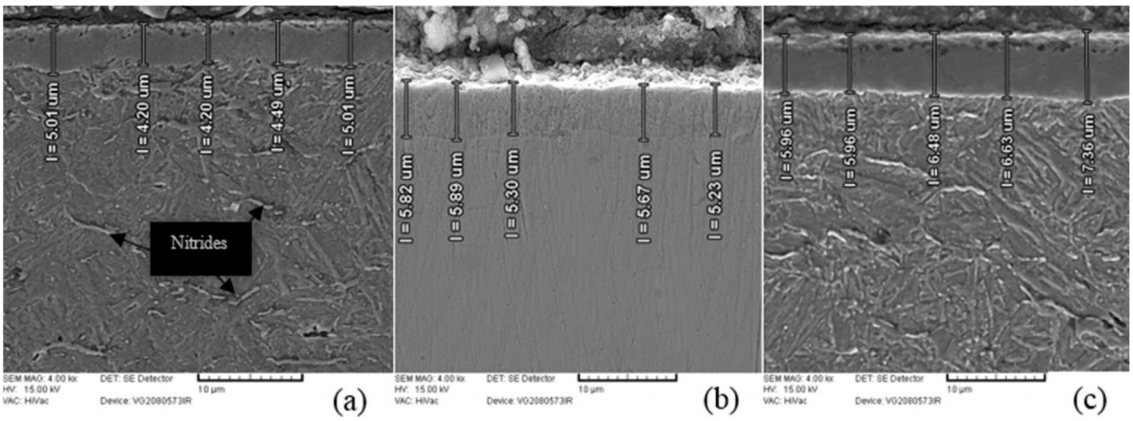

Fig. 4. SEM secondary electrons micrographs of the cross section specimen plasma nitrided at a gas mixture of 20 % H2: 80 % N2 at 450˚C, 500 ˚C and 550 ˚C for 10 h.

thickness with nitriding time [1]. In conventional plasma nitriding, prolongation of time would decrease the thickness of coating due to the direct formation of the plasma on the surface of the specimen and continuous surface sputtering whereas in ASPN process the plasma forms on the screen. Thus, particles deposit continual on the surface leading to increase in coating thickness by treatment time. Moreover, thickness of layers is depended on temperature by Arrhenius equation [19]. In fact, increasing temperature causes increment in diffusion constant which produces thicker diffusion zone.

Cross sectional microhardness depth profile of samples nitrided at different nitriding time in 450˚C, 500 ˚C and 550 ˚C is illustrated in Fig. 6 (a-c). The results clearly show that near surface hardness is higher by 3 times compared to that of un-nitrided substrate material. Surface hardening induced by nitriding, can be attributed to the [20]; Solution of nitrogen atoms in the iron lattice which induces solid solution strengthening,

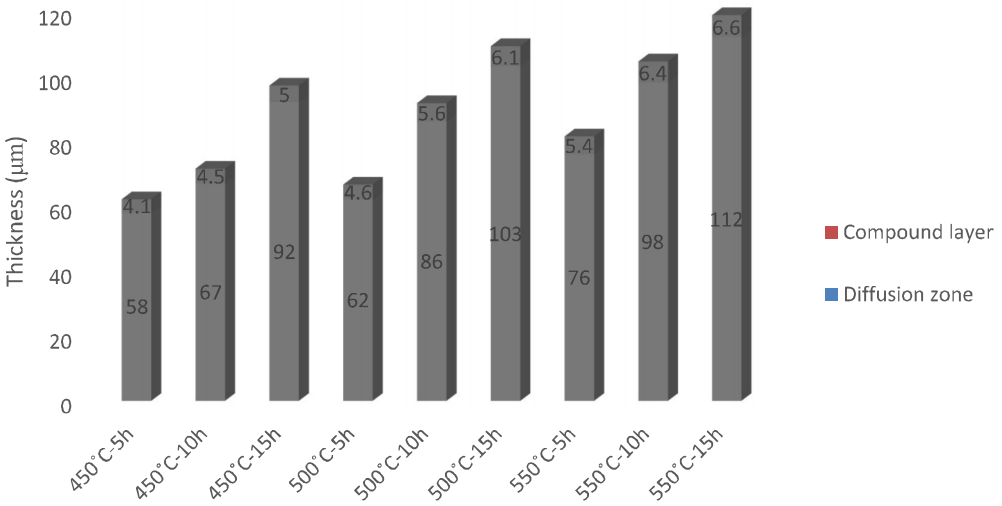

Fig. 5. Thickness of compound layer and diffusion zone for nitrided samples at various plasma nitriding condition

[DOI: 10.22068/ijmse.14.2.41]

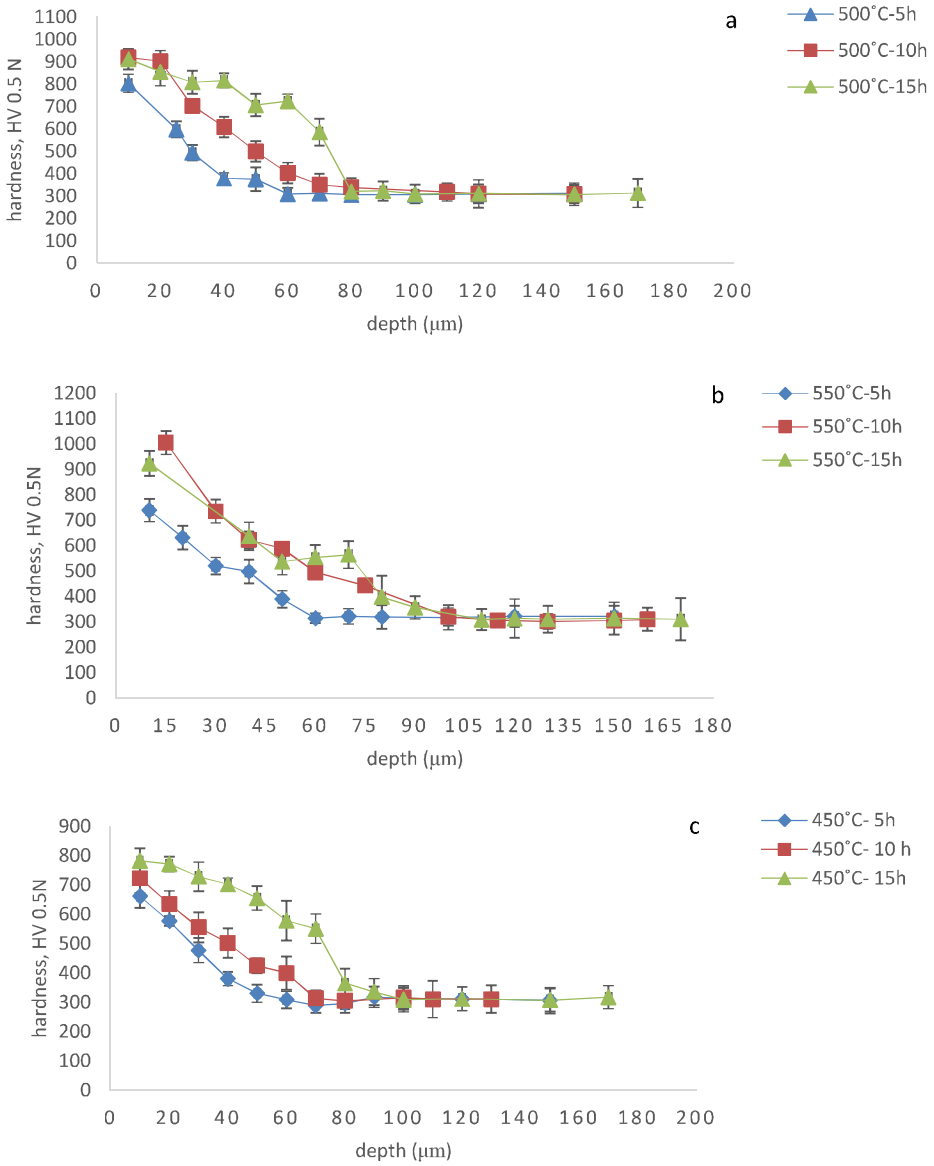

Fig. 6. Cross-sectional hardness-depth profile after plasma nitriding for different time at (a) 450˚C, (b) 500˚C, (c) 550˚C

formation of alloy nitrides and fine precipitates acting as obstacle against dislocations movement and development of compressive residual stress as a result of structural misfit because of formation of interstitial solid solution and alloying element nitrides. Moreover, Fig. 6 shows that at longer times, more atomic nitrogen diffuses from top surface towards substrate and hence expanding diffusion zone. Incremental decline in top surface microhardness could be due to the growth and coarsening of nitride precipitates which leads to lower precipitate density and lower hardness [15, 21]. Diffusion depth and microhardness is enhanced by temperature at different treatment times. Higher temperature could increase the driving force of atomic nitrogen diffusion toward the substrate which may induce nitrided phase in a higher depth.

[DOI: 10.22068/ijmse.14.2.41]

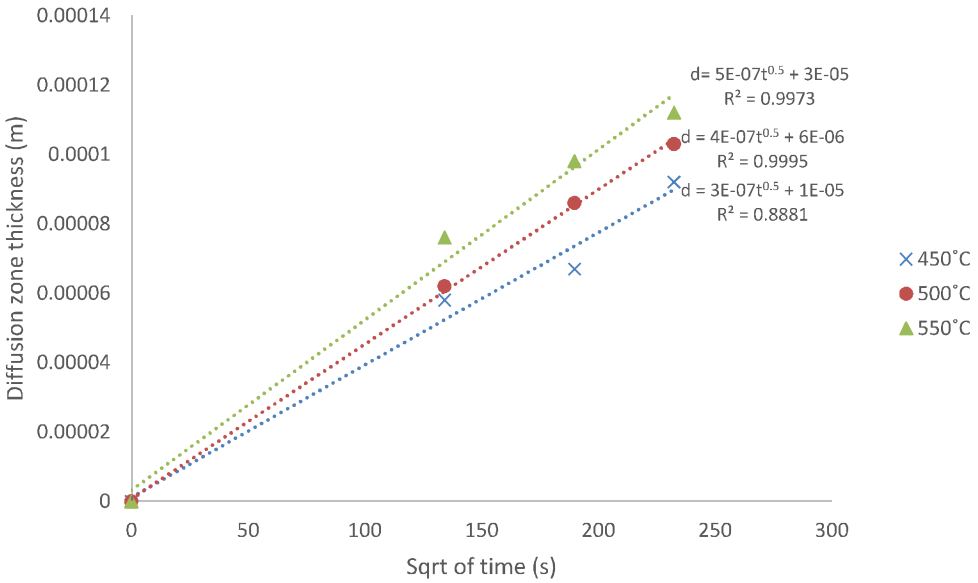

Fig. 7. Diffusion layer thickness as a function of plasma nitriding time

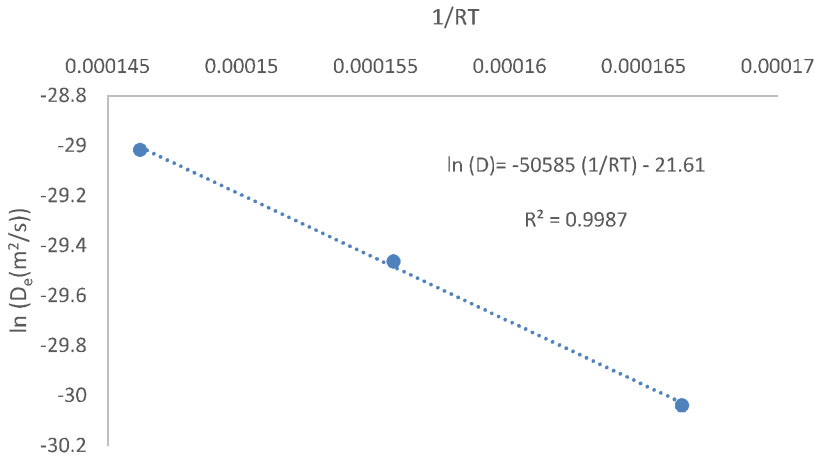

Fig. 8. Calculated values of Q and Dko for nitrogen diffusion in substrate.

In Fig. 7 the variation of diffusion depth estimated by OM, SEM and microhardness depth profile is drawn versus the nitriding time. A linear relationship was found between d and t0.5 as expected for a diffusion controlled process. The symbols represent the obtained results and the curves are obtained from fitting of Eq.1 on obtained results. Regarding the results of diffusion thickness measurements and with the usage of Arrhenius equation Eq. 2, values of Q and Do for nitrogen diffusion in substrate were calculated as 50585(j/mol) and 4.11×10^{-10} (m^2/s), respectively. Diffusion coefficient of nitrogen (Dn) at 450˚C would be calculated 3.7×10^{-13} (m^2/s) by substituting Q and Do values in Eq. 2. 3.7×10^{-13}. Fig. 8 shows values of Q and Dko for

[DOI: 10.22068/ijmse.14.2.41]

nitrogen diffusion in substrate.

4. CONCLUSION

The compositions of the coatings were studied by X-ray diffraction technique. The results showed that the compound layer was consisted mostly of dual phase -Fe4N and -Fe2–3N. Increasing treatment temperature increased both -Fe4N and -Fe2–3N in the compound layer, however increasing the processing time increased only the -Fe4N phase. Increasing treatment time and temperature increased both the compound and diffusion layer thicknesses. A linear relationship was found between the diffusion layer depth and the square root of the nitriding time, as expected for a diffusion controlled process. Values of Q and Do for nitrogen diffusion in substrate for ASPN method were calculated as 50585(j/mol) and 4.11×10^{-10} (m^2/s), respectively.

REFERENCES

1. Yazdani, A., Soltanieh, M., and Aghajani, H., "Active screen plasma nitriding of Al using an iron cage: Characterization and evaluation". Vacuum, 2015, 122, 127-134.
2. Sun, Y. and Bell, T., "Plasma surface engineering of low alloy steel", Materials Science and Engineering: A, 1991, 140, 419-434.
3. Nayebpashaee, N, Soltanieh, M, and Kheirandish, S, A Study on Formation and Growth Mechanism of Nitride Layers during Plasma Nitriding Process of Plastic Injection Mould Steel, Materials and Manufacturing Processes, 2015, 126,245-254.
4. Li, Y. and Bell, T., "Potential of plasma nitriding of polymer for improved hardness and wear resistance", Journal of materials processing technology, 2005, 168, 219-224.
5. Li, C., Dong, H. and Bell, T., "A feasibility study of plasma nitriding of steel with an oxide layer on the surface", Journal of materials science, 2006, 156, 6116-6118.
6. Kauling, A. P., Soares, G. V., Figueroa, C. A., Oliveira, R. V., Baumvol, I. J., Giacomelli, C., "Polypropylene surface modification by active screen plasma nitriding", Materials Science and Engineering: C, 2009, 29, 363-366.
7. Li, C., Bell, T. H. and Dong, H., "A study of active screen plasma nitriding, Surface engineering", 2002, 18, 174-181.
8. Gallo, S. C. and Dong, H., "On the fundamental mechanisms of active screen plasma nitriding", Vacuum, 2009, 84, 321-325.
9. Li, C., Georges, J. and Li, X., "Active screen plasma nitriding of austenitic stainless steel", Surface Engineering, 2002, 18, 453-457.
10. Alves Jr, C., "Plasma nitriding: Foundations and applications", EDFRN, Natal, 2001.
11. Nagatsuka, K., Nishimoto, A. and Akamatsu, K., "Surface hardening of duplex stainless steel by low temperature active screen plasma nitriding", Surface and Coatings Technology, 2010, 205, S295-S299.
12. Clarke, T., da Silva Rocha, T., Reguly, A. and Hirsch, T., "In situ XRD measurements during plasma nitriding of a medium carbon steel", Surface and Coatings Technology, 2005, 194, 283-289.
13. Dimitrov, V., D'Haen, J., Knuyt, G., Quaeyhaegens, C. and Stals, L., "A method for determination of the effective diffusion coefficient and sputtering rate during plasma diffusion treatment", Surface and Coatings Technology, 1998, 99, 234-241.
14. Egert, P., Maliska, A., Silva, H. and Speller, C., "Decarburization during plasma nitriding", Surface and Coatings Technology, 1999, 122, 33-38.
15. Corengia, P., Ybarra, G., Moina, C., Cabo, A. and Broitman, E., "Microstructural and topographical studies of DC-pulsed plasma nitrided AISI 4140 low-alloy steel", Surface and Coatings Technology, 2005, 200, 2391-2397.
16. Pinedo, C. E. and Monteiro, W. A,, "On the kinetics of plasma nitriding a martensitic stainless steel type AISI 420", Surface and Coatings Technology, 2004, 179, 119-123.
17. Roliński, E. and Sharp, G., "The effect of sputtering on kinetics of compound zone formation in the plasma nitriding of 3% Cr-Mo-V steel", Journal of materials engineering and performance, 2001, 10, 444-448.
18. Nishimoto, A., Nii, H., Narita, R. and Akamatsu, K., "Simultaneous duplex process of

[DOI: 10.22068/ijmse.14.2.41]

TiN coating and nitriding by active screen plasma nitriding", Surface and Coatings Technology, 2013, 228, S558-S562.

19. Porter, D. A., Easterling, K. E. and Sherif, M., "Phase Transformations in Metals and Alloys", (Revised Reprint): 2009, CRC press,.
20. Pellizzari, M., Molinari, A. and Straffelini, G., "Thermal fatigue resistance of gas and plasma nitrided 41CrAlMo7 steel", Materials Science and Engineering: A, 2003, 352, 186-194.

[DOI: 10.22068/ijmse.14.2.41]

Microstructure and Mechanical Properties of the Ultrafine-Grained Copper Tube Produced by Severe Plastic Deformation

H. Torabzadeh Kashi[1], M. Bahrami[1], J. Shahbazi Karami[2] and G. Faraji[1*]

* *ghfaraji@ut.ac.ir*

Received: December 2016 Accepted: April 2017

[1] Department of Mechanical Engineering, Faculty of Engineering, University of Tehran, Tehran, Iran.
[2] Faculty of Mechanical Engineering, Shahid Rajaee Teacher Training University, Tehran, Iran.
DOI: 10.22068/ijmse.14.2.32

Abstract: *In this paper, cyclic flaring and sinking (CFS) as a new severe plastic deformation (SPD) method was employed to produce the ultrafine grain (UFG) copper tubes. The extra friction has eliminated in the CFS method that provided the possibility for production of longer UFG tubes compared to the other SPD methods. This process was done periodically to apply more strain and consequently finer grain size and better mechanical properties. The CFS was performed successfully on pure copper tubes up to eleven cycles. Mechanical properties of the initial and processed tubes were extracted from tensile tests in the different cycles. The remarkable increase in strength and decrease in ductility take placed in the CFS-ed tubes. The material flow behavior during CFS processing was analyzed by optical microscopy (OM), and a model was presented for grain refinement mechanism of pure copper based on multiplication and migration of dislocations (MMD). This mechanism caused that the initial grains converts to elongated dislocation cells (subgrains) and then to equiaxed ultrafine grains in the higher cycles. The CFS method refined the microstructure to fine grains with the mean grain size of 1200nm from initial coarse grain size of 40μm.*

Keywords: *Severe plastic deformation, Copper tube, Grain refinement, Mechanical properties*

1. INTRODUCTION

Ultrafine grained (UFG) materials have been introduced as a new generation of metal products with the superior and unique mechanical and physical properties [1, 2]. While strength in the ultrafine-grained metallic material is much higher than the coarse-grained material [3], their ductility is also good [4]. The ultrafine grained materials show excellent ductility properties even at lower temperatures and higher strain rates [5]. Many types of research were done to develop the ultra-fine metal production processes on a laboratory and industry scales. Ultrafine grained metals have a much higher strength-to-weight ratio. In UFG materials, there are other properties such as coaxial and homogeneous microstructure with high angle grain boundaries (HAGB) [6, 7]. The presence of plenty of high angle grain boundaries has a particular importance in achieving the desired properties. In this regard, studies had shown that one of the most effective ways of processing ultrafine grained metallic material is the severe plastic deformation methods (SPD) [8]. In severe plastic deformation methods, high hydrostatic pressure with an intense shear strain cause to refine the microstructure and produce UFG materials [9]. On the other hand, hydrostatic pressure prevents cracks growth, therefore may severe deformations can be applied to the materials with low plasticity [10]. In the last decade, due to growing demand for tubular parts with high strength, some studies have been done to produce UFG tubes. Tooth et al. had Produced ultra-fine tubes using high-pressure tube twisting in 2009 [11]. Mohebi in 2010 had introduced a new method as accumulative spin-bonding (ASB) to produce this kind of tubes [12]. Zangiabadi et al. had masterminded producing high-strength tubes using tube channel pressing (TCP) [13]. Faraji et al. in 2011 had invented tube channel angular pressing (TCAP) process as the optimal way, inexpensively and with the industrial capability [14]. In 2012, parallel tubular channel angular pressing (PTCAP) was presented by Faraji [15].

[DOI: 10.22068/ijmse.14.2.41]

Babaei et al. had taken an innovative step to produce UFG tubes with introducing of two new methods of tube cyclic expansion-extrusion (TCEE) and tube cyclic extrusion-compression (TCEC) [16, 17]. Jafarzadeh et al. had introduced a method under repetitive tube expansion and shrinking (RTES) and have reached success in the production of ultra-fine tubes [18]. More recently, Torabzadeh et al. have presented a method as cyclic flaring and sinking (CFS) by modifying the PTCAP [19]. In this method, with no extra friction, UFG tubes can be achieved with a longer length compared to other methods.

In the present study, The CFS was applied to manufacture the UFG pure copper tubular samples` up to eleven cycles. The CFS processed samples were perused regarding microstructural evolution and mechanical properties. The mechanism of grain refinement of pure copper was introduced during CFS process. Fracture surfaces after tensile tests were investigated by scanning electron microscopy (SEM).

2. PRINCIPLES OF CFS

Fig. 1 depicts schematic illustrations of CFS process. Cyclic flaring and sinking method consists two half-cycles. At first, the tube with the radius of R1 is pressed on the flaring punch, so that shear zones are made with tensile stress and the tube radius increases of up to R2 (Fig 1b). In the next half-cycle, the tube is forced into sinking die, and compressive stress is created at the same shear zones so that the initial radius is obtained (Fig 1c). By considering that the cross-section of the CFS-ed tube remains constant, this process can be repeated cyclic to impose the desired plastic strain on the material.

Fig. 1d depicts geometric parameters of deformation. Because the strain state of the CFS is similar to the PTCAP process [20], the strain calculation could be made similar to PTCAP process. So, the equivalent plastic strain at each half cycle is calculated using equation (1). ($\psi_1=\psi_2= 0°$)

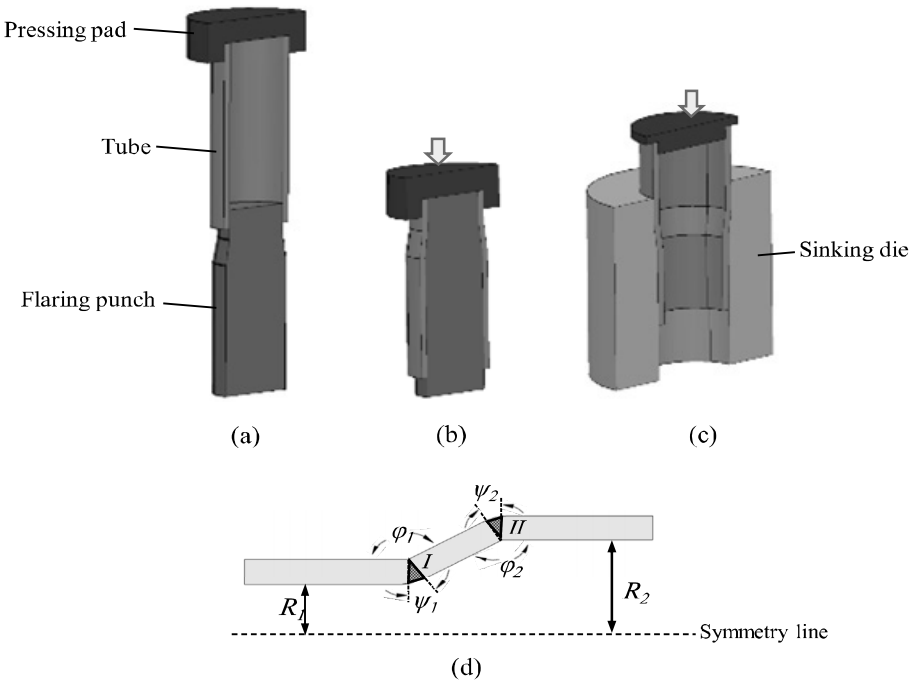

Fig. 1. The schematic illustration of the CFS method (a) initial state, (b) the flaring half-cycle, (c) the sinking half-cycles and (d) the geometric parameters.

[DOI: 10.22068/ijmse.14.2.41]

$$\bar{\varepsilon}_T = \sum_{i=1}^{2}\left[\frac{2\cot(\varphi_i/2)}{\sqrt{3}}\right] + \frac{2}{\sqrt{3}}\ln\frac{R_2}{R_1} \quad (1)$$

Therefore total effective strain achieved after N cycles:

$$\bar{\varepsilon}_T = \sum_{i=1}^{2}\left[\frac{2\cot(\varphi_i/2)}{\sqrt{3}}\right] + \frac{2}{\sqrt{3}}\ln\frac{R_2}{R_1} \quad (2)$$

From Eq. (2), the equivalent plastic strain is about 0.45 after one cycle of CFS process with the parameters used in this work. The total equivalent plastic strain applied to the copper tubes after eleven CFS passes is about 5.

3. EXPERIMENT PROCEDURE

In this study, the CFS method was carried out on pure copper tubular samples. The outer diameter of tubes was chosen 22 mm, the thickness of 1.2 mm and a length of 70 mm. The flaring punch and sinking die were made of VCN 150 steel with a hardness of 25 HRC. Die parameters, and their values were: curvature angles $\psi_1=\psi_2= 0°$, the channel angles $\varphi_1=\varphi_2= 170°$, R_2=11mm and R_1=9.8mm. The deformation ratio ($K= R_2-R_1$) was considered the same as the tube thickness. The deformation ratio (K) is related to the die geometry and it represents the increase or decrease of tube diameter in the flaring or sinking half-cycle. Therefore, the K value remains constant in all of the cycles. The CFS experiments were carried out by thread mechanism press with 150 mm/min speed at room temperature. As shown in Fig. 2, the tensile test sample was cut in the axial direction in order to explore the influences of the CFS process on mechanical properties. True stress- strain curves of tube obtained using a tensile test at room temperature and strain rate of 5^{-10} 1/s .

4. RESULTS AND DISCUSSION

4. 1. Mechanical Properties

Fig. 3 shows the mechanical properties of the unprocessed and CFS processed tubes achieved from the tensile test through axial directions at room temperature. Fig. 3a shows the stress-strain curves of unprocessed and CFS processed tubes in the different cycles. Fig. 3b displays the extracted results from these diagrams for yield strength (YS), ultimate tensile strength (UTS) and the elongation (El). Yield strength (in 0.2% strain) in the initial state is 120 MPa, which increases to 165 MPa, 183 MPa and 185 MPa after three, five and eleven CFS cycles, respectively. Also, the ultimate tensile strength increases from ~180 MPa to ~285 MPa after eleven cycles. The tube strength increases due to reducing grain size and increasing the density of

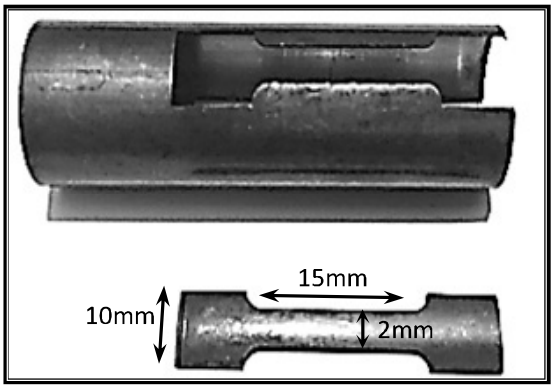

Fig. 2. Axial tensile test sample cut from unprocessed and CFS processed tube specimens.

[DOI: 10.22068/ijmse.14.2.41]

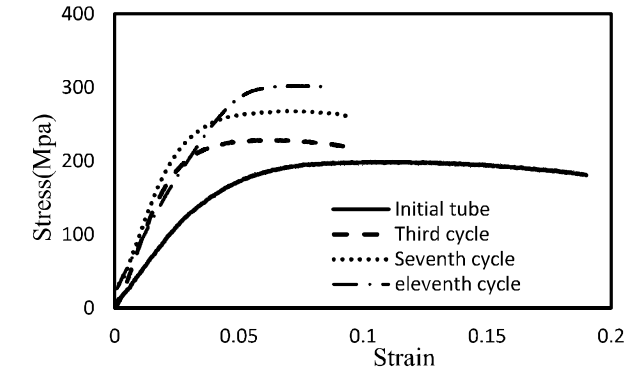

(a)

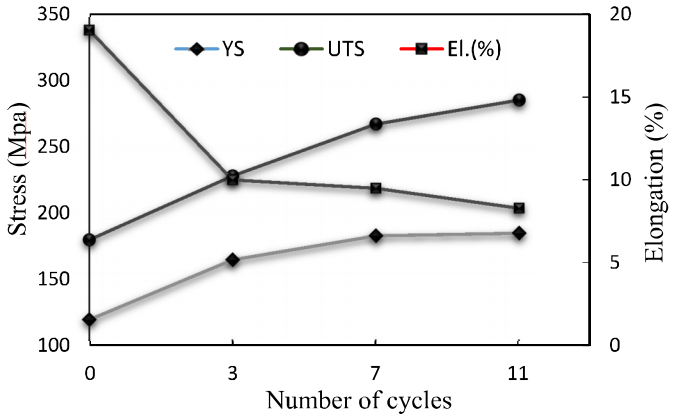

(b)

Fig. 3. (a) Tensile true stress–true strain curves and (b) the variation of mechanical properties in the different cycles.

dislocations [21]. Also, the grain boundaries and twins operate as a barrier to the dislocation movement and increase the resistance to deformation of material which leads to amplification of strength [22]. So, after eleven cycles of CFS process, the yield strength of ~185 MPa and the ultimate tensile strength of ~285 MPa can be reached. In the other word, yield and tensile strengths increase about 230 % and 47 % occurs, respectively. As it is clear, elongations decreases after eleven cycles of CFS processing to 8% from the initial value of 14%. The increase in the strength by grain refinement can lead to a possible decrease in ductility as reported for other SPD methods such as ASB. With the increase in strength, instability or necking occurs earlier, and the ductility of material reduces [12].

4. 2. Grain Refinement

Fig. 4 shows a cut section of the specimen parallel to the longitudinal axis during the process between the third and fourth cycle. As is evident, the tube is in the flaring step, and the material deforms in the shear zones (I) and (II). At first in Fig. 4a, the material microstructure consists of elongated grains in the longitudinal direction. Stretching of the grains has created as a result of applying severe plastic deformation in the previous three cycles [23]. When the material enters the shear zone (I), due to the normal and shear stress, the direction of material flow (MF)

[DOI: 10.22068/ijmse.14.2.41]

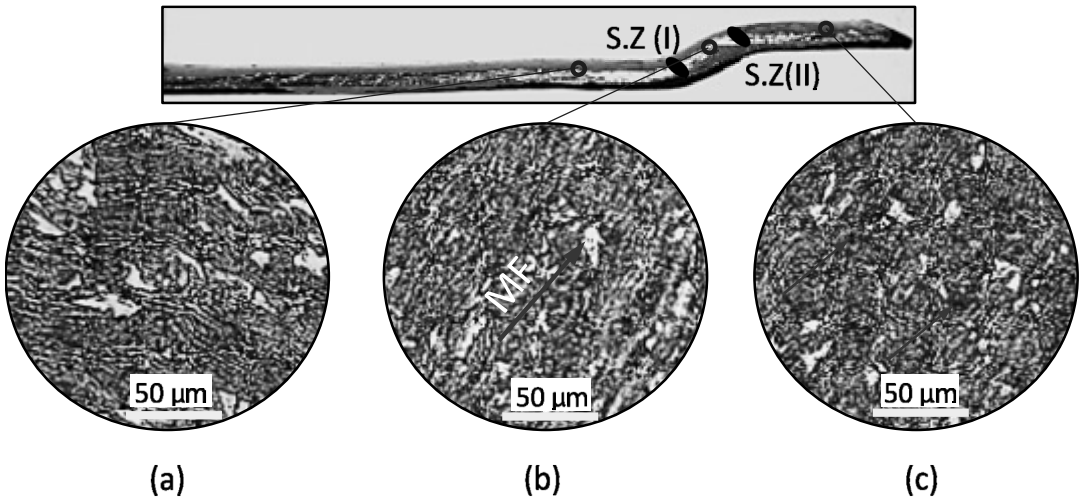

Fig. 4. The process of grain refinement between the third and fourth cycle, (a) before shear zone (I), (b) between shear zone (I) and shear zone (II) and (c) after shear zone (II).

changes. In the Fig. 4b, the orientation of grains has changed to the channel direction. Then the material approaches to the shear zone (II) and shear stress applies to the material once again. In Fig. 4c, the grains of the specimens after the shear zone (II) were significantly refined and, microstructure consists equiaxed grains compared to pre-shear zone (I). After the shear zone (II), the total accumulated equivalent plastic strain increases and the grain refinement occurs in the material [24]. The main factor is the shear strain that in addition to grain refinement, increases dislocations density in the microstructure [25, 26]. As shown by the red arrows in Fig. 4c, accumulation of dislocations was created by shear strains at different points of the material microstructure.

In order to study the microstructural evolutions after CFS processing, the OM images of unprocessed samples, after three and eleven cycles of CFS processed samples are shown in Fig. 5. As illustrated in Fig. 5a, there is the fully recrystallized heterogeneous microstructure of the unprocessed pure copper specimen with a mean grain size about 40 µm. With applying plastic strain until three cycles, the original grains were elongated according to the shear direction, and the energy level of materials decreased. These elongated grains were shown in Fig 5b that their thickness is very smaller than their length, with original grain boundaries still distinguishable. As seen in Fig. 5c, the microstructure of the specimen was significantly altered after eleven CFS cycles and is specifically different from the initial microstructure. After eleven cycles of CFS process, the structure was so much refined that the average grain size is about 1200 nm. Performing eleven cycles of CFS procedure on the material caused the microstructure uniformity increased, and equiaxed grains created in the material that corresponded to the previous studies [27, 28]. Fig. 5d shows the decline of average grain size versus the number of cycles. It is known that the reduction of grain size in the primary cycles was greater than the final cycles and the maximum reduction (30%) occurred after the second cycle. The decreasing in the grain sizes slowed down with increasing cycles, and the grain size stayed in nearly a constant value as a saturated grain size in the higher cycles. The microstructure evolution and grain refinement had occurred more on the primary cycles of SPD process [29].

In general, various mechanisms of refining pure copper in the SPD methods that have already introduced include shear deformation

[DOI: 10.22068/ijmse.14.2.41]

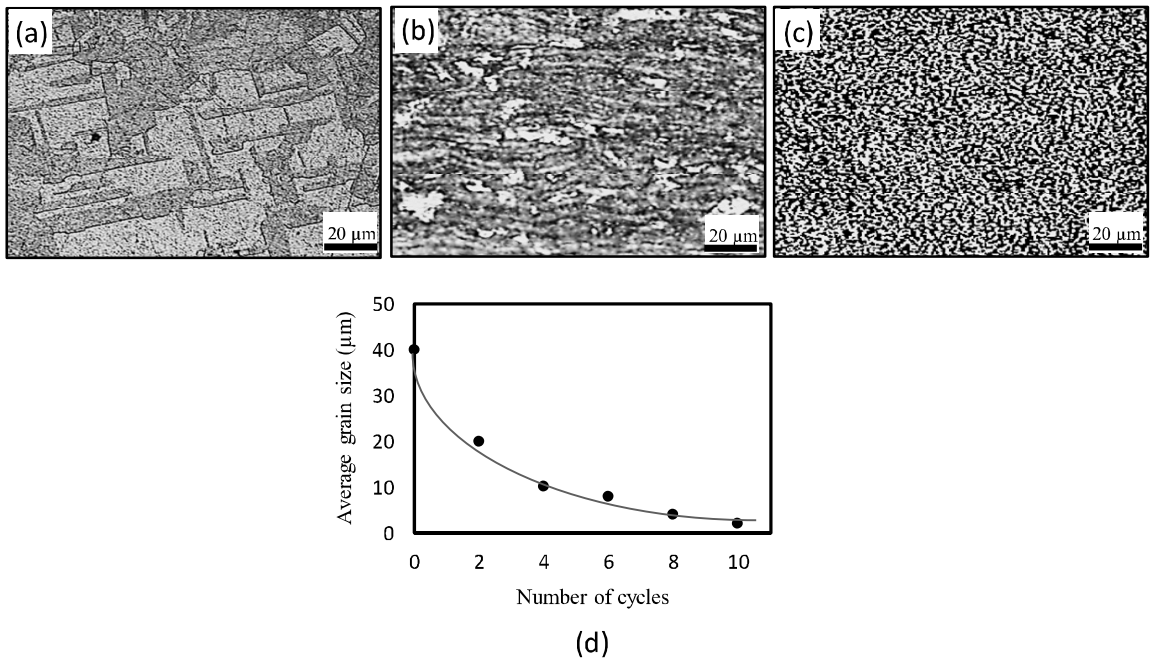

Fig. 5. (a) Microstructures of the unprocessed specimen, (b) after three cycles (c) after eleven cycles and (d) the average grain size in different cycles of CFS process.

[30], dislocation subdivision [31] and twin fragmentation [32]. According to the observed microstructural changes in Fig. 5, a model can be introduced for the dominant grain refinement mechanism in the UFG copper tubes. The model was shown in Fig. 6 which describes the procedure of the fragments original coarse grains and refines the microstructure to ultrafine grained in the severe plastic deformation methods. 1) At first, a random dislocation distribution is observed in Fig. 6a which is not a low-energy configuration. 2) As shown in Fig.6b, Due to applying strain, the dislocations density increases into an intra-granular that results in tangling of the dislocations with the regular arrangement and consequently formation of elongated dislocation cells (D_2>>D_1). 3) As the deformation continues, the dislocations rearrange to form the boundaries of fine grains (Fig. 6c). 4) In higher cycles, accumulation of dislocations increases in the dislocation walls that causes to produce sub-grains with low angle boundaries. With increasing the deformation, the number of sub-grains increments until the material converts to the UFG structure (Fig. 6d). 5) As is clear in the Fig 6e, in the higher cycles, the shear strain causes the sub-grains rotate relative to each other. Accordingly, the inter-granular sub-grains tends to disorient, and the high angle grain boundaries form in the material structure [33].

4. 3. Fracture Surface

SEM was utilized to clarify the rupture mechanisms in the unprocessed, and the CFS processed pure copper samples. Fig. 7 depicts the images of a fractured surface of tensile samples in unprocessed and after seven cycles of CFS. The failure surface of samples consists a large number of dimples or microvoids that indicating ductile fracture mode [18]. The basic steps of ductile rupture are the formation of microvoids, coalescence of microvoids (also known as crack formation), propagation of crack and finally, the failure occurs [34]. As shown in Fig. 7(a), the initial specimen contained long and deep equiaxed dimples in the average size of ~20 µm. In ductile fracture, there is slow crack

[DOI: 10.22068/ijmse.14.2.41]

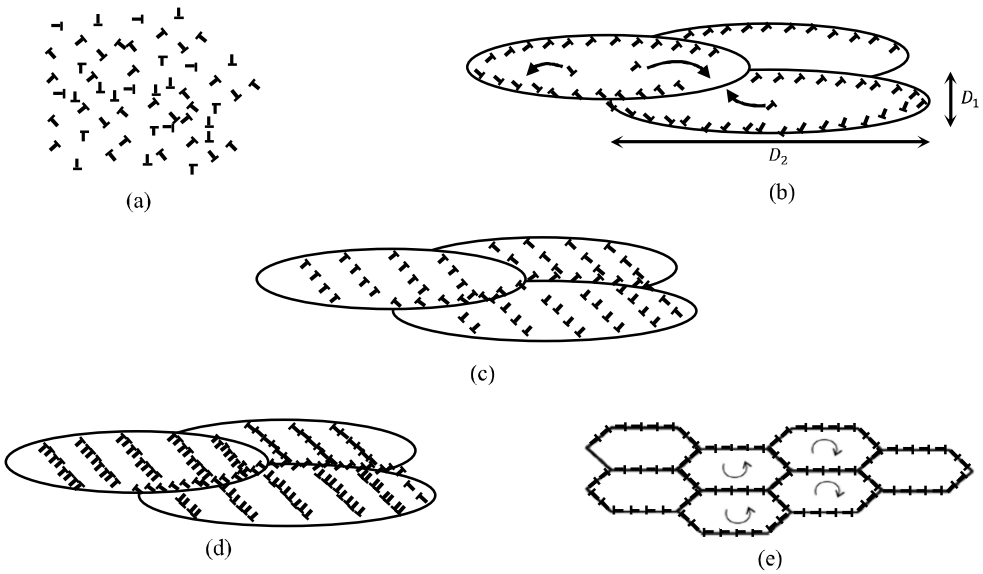

Fig. 6. Schematic of the grain refinement mechanism in the UFG copper tubes. (a) Random dislocation distribution, (b) Elongated grains, (c) the dislocations rearrange to form fine grain boundaries, (d) accumulation of dislocations in the wall and forming the subgrains and (e) Forming the high angle grain boundaries.

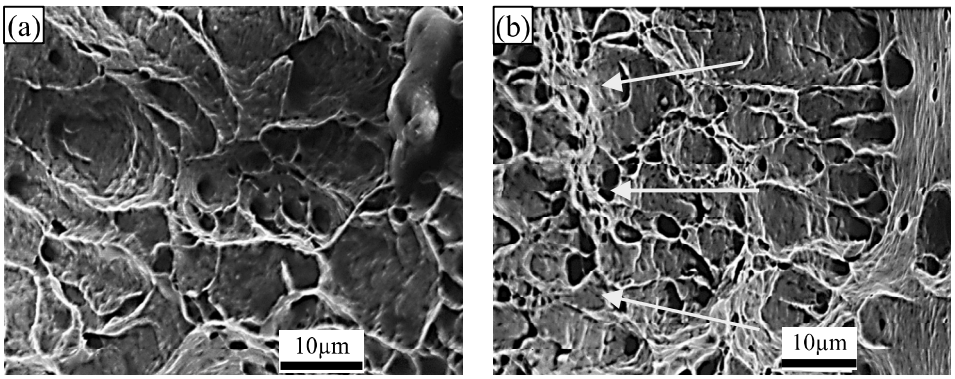

Fig. 7. SEM images of fractured surfaces after the tensile tests of a) unprocessed state, b) after seven cycles of CFS.

propagation and a large absorption of energy before fracture. So that, there is the required time for the formation of large and deep dimples during the tensile test [35]. .Fig. 7(b) shows the samples after seven cycles of CFS process. In the CFS processed samples, the number of dimples has decreased, and the dimples distribution was changed on the fracture surface. In this mode, shallow and tiny dimples were observed that distributed more uniformly on fracture surface with the average size of ~1.5 μm. The decrease of the dimple size is related to the grain refinement in the structure of the CFS processed tubes [36, 37]. With the decrease of ductility in the CFS processed samples, the dimples do not have enough time to grow and assemble with the other neighboring dimples. Therefore shallow dimples were observed in the samples after seven cycles of CFS [18]. Another issue is that the shallow dimples oriented toward the tension zone where the ultimate failure occurs (yellow arrows).

[DOI: 10.22068/ijmse.14.2.41]

5. CONCLUSION

In this paper, a new method of severe plastic deformation as cyclic flaring and sinking (CFS) was used for the production of UFG copper tubes. This method was successfully applied to the pure copper tubes up to eleven cycles. The mechanical properties of the tubes significantly improved as a result of CFS method. The yield and tensile strength of pure copper increased up to 185 and 285 Mpa respectively after eleven cycles of CFS. The SEM images of the fracture surfaces depicted the fracture procedure which justified the decrease of ductility in the tubes after CFS process. The improvement of tube strength enhanced as a result of grain refinement in the processed samples. Optical observations documented remarkable grain refinement after CFS processing as the grain size the mean grain size reduced to 1200nm from the initial of 40μm. The presented grain refinement mechanism based on four stages with continuous applying plastic strain: a) the initial coarse grains converted to elongated grains through migration of dislocations. b) The dislocations rearranged on fine grain boundaries. c) The dislocation density increased on walls, and the subgrains were formed. d) The formed ultrafine grains rotated to one another, and the high grain boundaries (HAGBs) were produced. The presence of ultrafine grains with HAGBs was the main reason for the superior mechanical properties in the CFS-ed tubes.

REFERENCE

1. Valiev, R. Z. and T. G. Langdon, "Principles of equal-channel angular pressing as a processing tool for grain refinement". Progress in Materials Science, 2006, 51, 881-981.
2. Beyerlein, I. J. and L. S. Tóth, "Texture evolution in equal-channel angular extrusion". Progress in Materials Science, 2009, 54, 427-510.
3. Kawasaki, M. and T. Langdon, "Principles of superplasticity in ultrafine-grained materials". Journal of Materials Science, 2007, 42, 1782-1796.
4. Máthis, K., J. Gubicza, and N. H. Nam, "Microstructure and mechanical behavior of AZ91 Mg alloy processed by equal channel angular pressing". Journal of Alloys and Compounds, 2005. 394, 194-199.
5. Matsunoshita, H., "Ultrafine-grained magnesium–lithium alloy processed by high-pressure torsion: Low-temperature superplasticity and potential for hydroforming". Materials Science and Engineering: A, 2015, 640, 443-448.
6. Valiev, R. Z., R. K. Islamgaliev, and I. V. Alexandrov, "Bulk nanostructured materials from severe plastic deformation". Progress in Materials Science, 2000, 45, 103-189.
7. Zhilyaev, A. P. and T. G. Langdon, "Using high-pressure torsion for metal processing: Fundamentals and applications". Progress in Materials Science, 2008, 53, 893-979.
8. Sabirov, I., M. Y. Murashkin, and R. Z. Valiev, "Nanostructured aluminium alloys produced by severe plastic deformation: New horizons in development". Materials Science and Engineering: A, 2013, 560, 1-24.
9. Valiev, R., "Producing bulk ultrafine-grained materials by severe plastic deformation". JOM, 2006, 58, 33-39.
10. Zhilyaev, A. P., "The microstructural characteristics of ultrafine-grained nickel". Materials Science and Engineering: A, 2005, 391, 377-389.
11. Tóth, L. S., "Severe plastic deformation of metals by high-pressure tube twisting". Scripta Materialia, 2009, 60, 175-177.
12. Mohebbi, M. S. and A. Akbarzadeh, Accumulative spin-bonding (ASB) as a novel SPD process for fabrication of nanostructured tubes". Materials Science and Engineering: A, 2010, 528, 180-188.
13. Zangiabadi, A. and M. Kazeminezhad, "Development of a novel severe plastic deformation method for tubular materials," Tube Channel Pressing (TCP). Materials Science and Engineering: A, 2011, 528, 5066-5072.
14. Faraji, G., M. M. Mashhadi, and H. S. Kim, "Tubular channel angular pressing (TCAP) as a novel severe plastic deformation method for cylindrical tubes". Materials Letters, 2011, 65, 3009-3012.
15. Faraji, G., et al., Parallel tubular channel

[DOI: 10.22068/ijmse.14.2.41]

angular pressing (PTCAP) as a new severe plastic deformation method for cylindrical tubes. Materials Letters, 2012. 77, 82-85.
16. Babaei, A., M. M. Mashhadi, and H. Jafarzadeh, "Tube Cyclic Extrusion-Compression (TCEC) as a novel severe plastic deformation method for cylindrical tubes". Materials Science and Engineering: A, 2014, 598, 1-6.
17. Babaei, A., M. M. Mashhadi, and H. Jafarzadeh, "Tube cyclic expansion-extrusion (TCEE) as a novel severe plastic deformation method for cylindrical tubes". Journal of Materials Science, 2014, 49, 3158-3165.
18. Jafarzadeh, H. and K. Abrinia, "Fabrication of ultra-fine grained aluminium tubes by RTES technique". Materials Characterization, 2015. 102, 1-8.
19. Torabzadeh, H., G. Faraji, and E. Zalnezhad, "Cyclic Flaring and Sinking (CFS) as a New Severe Plastic Deformation Method for Thin-walled Cylindrical Tubes". Transactions of the Indian Institute of Metals, 2015, 1-6.
20. Faraji, G., "Parallel tubular channel angular pressing (PTCAP) as a new severe plastic deformation method for cylindrical tubes". Materials Letters, 2012, 77, 82-85.
21. Afrasiab, M., "Excellent energy absorption capacity of nanostructured Cu–Zn thin-walled tube". Materials Science and Engineering: A, 2014, 141-144.
22. Tavakkoli, V., "Severe mechanical anisotropy of high-strength ultrafine grained Cu–Zn tubes processed by parallel tubular channel angular pressing (PTCAP)". Materials Science and Engineering: A, 2015, 625, 50-55.
23. Arzaghi, M., "Microstructure, texture and mechanical properties of aluminum processed by high-pressure tube twisting". Acta Materialia, 2012, 60, 4393-4408.
24. Jamali, S. S., G. Faraji, and K. Abrinia, "Hydrostatic radial forward tube extrusion as a new plastic deformation method for producing seamless tubes". The International Journal of Advanced Manufacturing Technology, 2016, 1-11.
25. Mesbah, M., G. Faraji, and A. R. Bushroa, "Characterization of nanostructured pure aluminum tubes produced by tubular channel angular pressing (TCAP)". Materials Science and Engineering: A, 2014, 590, 289-294.
26. Haghdadi, N., et al., An investigation into the homogeneity of microstructure, strain pattern and hardness of pure aluminum processed by accumulative back extrusion. Materials Science and Engineering: A, 2014, 595, 179-187.
27. Zhu, C. F., "Microstructure and strength of pure Cu with large grains processed by equal channel angular pressing". Materials & Design, 2013, 52, 23-29.
28. Mishra, A., et al., Microstructural evolution in copper processed by severe plastic deformation. Materials Science and Engineering: A, 2005, 410–411, 290-298.
29. Nemati, J., "Improvements in the microstructure and fatigue behavior of pure copper using equal channel angular extrusion". International Journal of Minerals, Metallurgy, and Materials, 2014, 21, 569-576.
30. Segal, V. M., "Severe plastic deformation: simple shear versus pure shear". Materials Science and Engineering: A, 2002, 338, 331-344.
31. Zhang, Z. J., "Microstructure and mechanical properties of Cu and Cu–Zn alloys produced by equal channel angular pressing". Materials Science and Engineering: A, 2011, 528, 4259-4267.
32. Qu, S., "Microstructural evolution and mechanical properties of Cu–Al alloys subjected to equal channel angular pressing". Acta Materialia, 2009, 57, 1586-1601.
33. Wang, K., "Plastic strain-induced grain refinement at the nanometer scale in copper." Acta Materialia, 2006, 54, 5281-5291.
34. Courtney, T. H., "Mechanical Behavior of Materials," Second Edition. 2005: Waveland Press.
35. Davis, J. R., Tensile Testing, 2nd Edition. 2004: A S M International.
36. Pippan, R., "The Limits of Refinement by Severe Plastic Deformation". Advanced Engineering Materials, 2006, 8, 1046-1056.
37. Babaei, A. and M. M. Mashhadi, "Tubular pure copper grain refining by tube cyclic extrusion–compression (TCEC) as a severe plastic deformation technique". Progress in Natural Science: Materials International, 2014, 24, 623-630.

[DOI: 10.22068/ijmse.14.2.41]

Applied of Impressed Current Cathodic Protection Design For Fuel Pipeline Network at Naval Base

A. K. Susilo*, A. Ahmadi, O. S. Suharyo and P. Pratisna

* *ku2h_lagi@yahoo.com*

Received: February 2017 **Accepted: April 2017**

Indonesian Naval Technology College, Bumimoro-Morokrembangan, Surabaya, Indonesia.

DOI: 10.22068/ijmse.14.2.41

Abstract: *Indonesian Navy (TNI AL) is the main component for Maritime Security and Defence. Because of that, TNI AL needs Indonesian Warship (KRI) to covered Maritime area. The main requirement from KRI is fulfilled by demand. To pock of fuel demand from KRI at Naval Base, it needs a new pipeline of fuel distribution network system. The pipeline network system used for maximum lifetime must be protected from corrosion. Basically, there are five methods of corrosion control such as change to a more suitable material, modification to the environment, use of protective coating, design modification to the system or component, and the application of cathodic or anodic protection. Cathodic protection for pipeline available in two kinds, namely Sacrifice Anode and Impressed Current Cathodic Protection (ICCP). This paper makes analysis from design of Impressed Current Cathodic Protection and total current requirement in the method. This paper showed both experimental from speciment test and theoritical calculation. The result showed that design of Impressed Current Cathodic Protection on fuel distribution pipeline network system requires voltage 33,759 V(DC), protection current 6,6035 A(DC) by theoritical calculation and 6,544 A(DC) from pipeline specimen test, with 0,25 mpy for corrosion rate. Transformer Rectifier design needs requirements 45 V with 10 A for current. This research result can be made as literature and standardization for Indonesian Navy in designing the Impressed Current Cathodic Protection for fuel distribution pipeline network system.*

Keywords: *Pipeline Network System, Corrosion, Cathodic Protection, ICCP, Rectifier*

1. INTRODUCTION

Indonesian Navy (TNI AL) is the main component for Maritime Security and Defence. Because of that, TNI AL needs Indonesian Warship (KRI) to covered Maritime area. The main requirement from KRI (Indonesian Warship) in activities of basic training, warfare alert and operation at sea is fulfilled by demand. Fuel is used for main engine and electricity at warship.

With the condition background what are demanded from KRI, it is urgent to make design of fuel pipeline distribution network system from metal materials to pock of fuel demand from KRI at Naval Base for supporting warfare alert, basic training and operation activities at sea, but the pipeline network system has negative effect from corrosion. Corrosion is the destructive attack of a material by reaction with its environment (Roberge, 1999). Because of that, the pipeline network system needs protection from corrosion that can applied underground. The corrosion of underground structure is a very widespread problem (Al-Sultani, et al., 2012). Structure such as natural gas, crude oil pipelines, and water are only some of the many structures reported to have been affected by soil corrosion (Al-Sultani, et al., 2012).

In today's regulated environment, a method to protect corrosion of all new hazardous pipelines (carrying oil, gas, or other potentially dangerous substances) is required by federal regulation to use an effective coating and cathodic protection (Parker, 1999). Cathodic Protection (CP) is a proven method of controlling corrosion in reinforced concrete through the application of a small Direct Current (DC) (Nguyen, et al., 2012). It is commonly used in the protection of the exterior surfaces of pipelines (Kakuba, 2005). There are two types of applying cathodic protection system, namely Sacrificial Anode Cathodic Protection (SACP) and Impressed Current Cathodic Protection (ICCP) (Al-Himdani, et al., 2005).

Impressed Current Cathodic Protection (ICCP) is a method to prevent corrosion by allowing an

[DOI: 10.22068/ijmse.14.2.41]

appropriate DC to flow continuosly through metal bodies in contact with wet soil or a corrosive aqueous solution (Choi, et al., 2016). It employs a direct current generator (rectifier) that has the pipe connected to the negative terminal of the rectifier, whereas the selected anode is connected to its positive terminal, thereby making the current flow from the selected anode to the onshore pipe forcibly and thus preventing corrosion currents in the pipeline. This is also called forced current method (Choi, et al., 2016).

This paper presents design of protection system and total current needed in the ICCP method. It has been an effort to apply design of corrosion prevented ICCP method for fuel pipeline distribution network system at Naval base, and to analyze corrosion rate from pipeline specimen test. Boundary of problem in this paper is ICCP method applied in surfaces of pipeline, soil chemical anaylis such as pH, Sulphate and Cloride content is ignored, coating is in good condition.

The inscriptive benefit from this paper is a literature for Indonesia Navy about the design of fuel distribution pipeline system in Naval base. It can be made as standarization for design of ICCP at fueled pipeline in Naval base.

This paper has many literatures to support the research, such as literature about corrosion control, cathodic protection and impressed current (ICCP). Literature of paper about corrosion control likes Corrosion Protection System in Offshore Structure (Ivanov, 2016). Synergic effect of Thiomalic acid and Zinc ions in Corrosion control of Carbon Steel in Aqueous Solution (Ramesh, et al., 2014). Reduction of Corrosion Process in Steel Bars Using Inhibitor (Zubaidy, et al., 2012). Green Inhibitor for Corrosion Protection of Metals and Alloys : An Overview (Rani, et al., 2011). Corrosion control in Oil and Gas Pipeline (Enani, 2016). Interactions of Corrosion Control and Biofilm on Lead and Copper in Premise Plumbing (Payne, 2013). Corrosion Control by Green Solution – An Overview (Raja, et al., 2014). Solutions to Corrosion Caused by Agricultural Chemicals (Eker, et al., 2005). Corrosion Protection of Steel Pipelines Againts CO2 Corrosion – A Review (El-Lateef, et al., 2012). Corrosion Control Approach Using Data Mining (Dapiap, et al., 2015).

Paper literature about cathodic protection such as Protect of Underground Oil Pipelines by Using (Al-Sn-Zn) as Sacrificial Anode in Al-Qasim Region (Al-Sultani, et al., 2012). Efficiency of Corrosion Inhibitors on Cathodic Protection System (Briggs, et al., 2014). (Mainier, et al., 2014). Modelling Cathodic Protection for Pipeline Network (Riemer, 2000). Cathodic Protection of an underground Pipeline by Photovoltaic Power System using Intelligent Method (Javadi, et al., 2104). The effect of Cathodic Protection System by Means of Zinc Sacrifial Anode on Pier in Korea (Jeong, et al., 2014). Cathodic Protection of Steel in Concrete Using Conductive Polymer Overlays (A.S.S.Sekar, et al., 2007). Interaction Between Cathodic Protection and Microbially Influenced Corrosion (Masli, 2011). Use of Sacrifial Anode for Corrosion Protection of Tradition Well Cover (Olusunle, et al., 2015). Cathodic Protection of Onshore Buried Pipelines Considering Economic Feasibility and Maintenance (Choi, et al., 2016).

Paper literature explains about ICCP is Shipboard Impressed Current Cathodic Protection System (ICCP) Analysis (Hogan, et al., 2005). Effectiveness of Impressed Current Cathodic Protection System in Concrete Following Current Interruption (Bhuiyan, 2015). Modeling and Control of Impressed Current Cathodic Protection (ICCP) System (Hashim, et al., 2014). Assessing the long term benefits of Impressed Current Cathodic Protection (Christodoulou, et al., 2010). ICCP cathodic protection of tanks with photovoltaic power supply (Janowski, et al., 2016). The Impressed Current Cathodic Protection System (Kakuba, 2005). System Identification Modelling and IMC Based PID Control of Impressed Current Cathodic Protection System (Balla, et al., 2013). Identification and Control of Impressed Current Cathodic Protection System (Sada, et al., 2016). The application of impressed current cathodic protection to historic listed reinforced concrete and steel framed structures (Broomfield, 2004).

This paper is organized as follows. Section 2 reviews the basic consepts of corrosion control. Section 3 gives result of research. Section 4 describes the analysis of Impressed Current Cathodic Protection System in fuel distribution pipeline. Finally, in section 5 presents this paper conclusion.

[DOI: 10.22068/ijmse.14.2.41]

2. MATERIAL/METHODOLOGY

2. 1. Corrosion

Corrosion is defined as the destruction or deterioration of material because of reaction with its environment (Fontana, 1987). Some insist that the definition should be restricted to metals, but often the corrosion, engineers must consider both metals and nonmetals for solution of given problem (Fontana, 1987). Corrosion is the damage to metal caused by reaction with environment. (Bradford, 2001). Corrosion is the degradation of material through environmental interaction (Peabody, 2001).

Important types of corrosion are general attack corrosion, metal attack corrosion, galvanic corrosion, environmental cracking, flow assisted corrosion, intragranular, fretting corrosion and high temperature corrosion (Kulkarni, 2015).

The corrosion process involves the removal of electrons (oxidation) of the metal and the consumption of those electrons by some other reduction reaction, such as oxygen or water reduction respectively (Peabody, 2001). Corrosion proccess develop fast after disruption of the protective barrier and are accompanied by a number of reactions that change the composition and properties of both the metal surface and the local environment, for example formation of oxides, diffussion of metal cations into the coating, local pH changes and electrochemical potential (Rani, et al., 2011).

$$Fe \rightarrow Fe^{2+} + 2e^{-} \quad (1)$$

$$O_2 \rightarrow 2H_2O^{+} + 4e^{-} \quad (2)$$

$$2Fe + O_2 + 2H_2O \rightarrow 2Fe_2 + 4OH^{-} \quad (3)$$

The oxidation reaction is commonly called the anodic reaction (1) and the reduction reaction (2) is called the cathodic reaction. Both electrochemical reactions are necessary for corrosion to occur. The oxidation reaction (3) causes the actual metal loss but the reduction reaction must be present to consume the electrons liberated by the oxidation reaction, maintaining charge neutrality (Peabody, 2001). Otherwise, a large negative charge would rapidly develop between the metal and the electrolyte and the corrosion process would cease. The oxidation and reduction reactions are sometimes referred to as half-cell reactions and can occur locally (at the same site on the metal) or can be physically separated (Peabody, 2001). When the electrochemical reactions are physically separated, the process is referred to as a differential corrosion cell (Peabody, 2001).

There are four necessary components of a differential corrosion cell (Bradford, 2001).

a. The anode, which is the metal that is corroding.
b. The cathode, which is a metal or other electronic conductor whose surface provides sites for the environment to react.
c. The electrolyte, (the aqueous environment), in contact with both the anode and the cathode to provide a path for ionic conduction.
d. The electrical connection between the anode and the cathode to allow electrons to flow between them.

2. 2. Corrosion Control Method

Corrosion prevention can take a number of forms depending on the circumstances of the metal being corroded. There are basically five methods of corrosion control: change to a more suitable material, modification to the environment, use of protective coating, design modification to the system or component, and the application of cathodic or anodic protection (Roberge, 1999).

The basic principle of cathodic protection (CP) is a simple one. CP is a method to reduce corrosion by minimizing the difference in potential between anode and cathode (Agarwal, et al., 2015). Cathodic protection is often applied to coated structures, with the coating providing the primary form of corrosion protection (Roberge, 1999). The CP current requirements tend to be excessive for uncoated systems. Its installations include buried tanks, marine structures such as offshore platforms, and reinforcing steel in concrete (Roberge, 1999).

[DOI: 10.22068/ijmse.14.2.41]

There are two main types of cathodic protection systems; there are impressed current and sacrificial anode. Both types of cathodic protection have anodes, a continuous electrolyte from the anode to the protected structure, and an external metallic connection (wire) (Agarwal, et al., 2015).

2. 3. Impressed Current Cathodic Protection

Impressed Current Cathodic Protection (ICCP) is applied by means of an external power current source (Roberge, 1999). It uses a power to move the current from a very noble anode material to protect the structures (Orazem, 2014). Its current is impressed on the structure by means of a power supply, referred to as a rectifier, and anode buried in the ground (Peabody, 2001).

The external current supply is usually derived from a Transformer Rectifier (TR), in which the AC power supply is transformed (down) and rectified to give a DC output (Roberge, 1999). Other power sources include fuel or gas driven generators, thermoelectric generators and solar and wind generators (Roberge, 1999). Important application areas of impressed current system includes pipelines and other buried structures, marines structures, and reinforcing steel embbeded in concrete (Roberge, 1999).

Some advantages of ICCP are as follows (Roberge, 1999) :

a. High current and power output range.
b. Ability to adjust the protection levels.
c. Large areas of protection.
d. Low number of anodes, even in high-resistivity environment.
e. Even protecting poorly coated structures.

These limitations that have been identified for ICCP system (Roberge, 1999) :

a. Relatively high risk of causing interference effects.
b. Lower reliability and higher maintenance requirements.
c. External power has to be supplied.
d. Running cost of external power consumption.

2. 4. Corrosion Rate

Corrosion rate is the amount of corrosion occurring per time unit (for example, mass change per area unit per time unit, penetration per time unit). The humidity, temperature fluctuations, wide variations in rainfall, wind, and pollutants prevent classification scheme to indication of corrosion rates (Roberge, 1999). One of them can use electrical method. It calculates with equation (NACE, 2002).

$$Corrosion\ rate = K\frac{Icorr\ x\ E}{D} \tag{4}$$

2. 5. Method of Research

This paper shows both experimental from speciment test and studied in detail theoritical calculation design of ICCP. The theoritical result

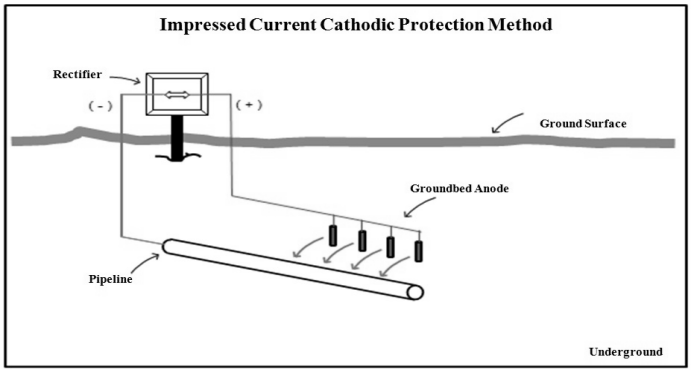

Fig. 1. ICCP Method

[DOI: 10.22068/ijmse.14.2.41]

Table 1. Value of Corrosion Rate(Fontana, 1987)

Relative Corrosin Resistance	Approximate Metric Equivalent				
	mpy	mm/yr	µm/yr	nm/yr	pm/s
Outstanding	<1	< 0,02	< 25	< 2	< 1
Excellent	1 - 5	0,02 - 0,1	25 - 100	2 - 10	1 - 5
Good	5 -20	0,1 - 0,5	100 - 500	10 - 50	5 - 20
Fair	20 - 50	0,5 - 1	500 - 1000	50 - 150	20 - 50
Poor	50 - 200	1 - 5	1000 - 5000	150 - 500	50 - 200

is compared with experimental results showing criteria for design of ICCP in fuel pipeline distribution system. The first phase is identification of the problem, library studies, and the planning of cathodic protection system.

2. 5. 1. Flowchart Diagram

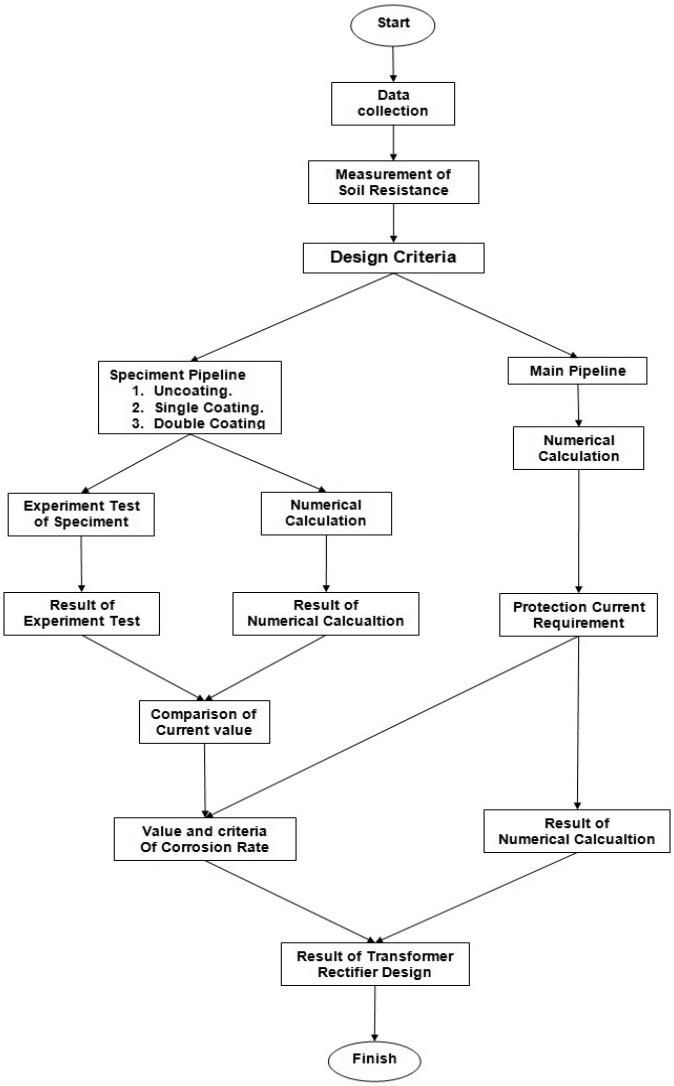

[DOI: 10.22068/ijmse.14.2.41]

2. 5. 2. Data Collection

a. Main pipeline network data.

1) Pipeline.

Carbon steel with classification from spiral pipe seamless ASTM A106 Grade B. Long pipeline 1163.99 m ; outside diameter 0,219 m; thickness 0.00818 m; resistance $3.48*10^{-4}$ Ω-m.

2) Anode.

Carbon graphite; turbular ; long=1m; Diameter 0.06 m; current density 2.5-10 A/ m^2; consumption rate 0.1-1 kg/(A.year).

3) Coating data.

Coaltar epoxy cure polyamide with specification Hot Applied mill coated pipe; 25 °C for temperature; stage destruction 5-65 % per year.

b. Speciment data.

1) Pipeline.

Carbon steel with classification from spiral pipe seamless ASTM A106 Grade B. Long pipeline 0.5 m ; outside diameter 0,048 m; thickness 0.0037 m; resistance $3.48*10^{-4}$ Ω-m.

2) Anode.

Carbon graphite; turbular ; long = 0,01 m; Diameter 0.036 m; current density 2.5-10 A/m^2; consumption rate 0.1-1 kg/(A.year).

3) Coating data.

Coaltar epoxy cure polyamide with specification Hot Applied mill coated pipe; 25 °C for temperature; stage destruction 5-65 % per year.

2. 5. 3. Theoritical Calculation Design

Theoritical calculation design is conducted prior to detailed design of ICCP to achieve value of the system requirements. Its reports describe the investigations made and measurements taken, and make recommendations the result of building design. It has many steps to design(NACE, 2002):

a. Soil resistivity.

b. Surfaces range of pipeline system has protected.

c. Protecting current requirement.

d. Pipeline resistance.

e. Coating conductance.

f. Attenuation constant

g. Pipeline characteristic resistance.

h. Potential shifts.

i. Current of anode.

j. Requirement of total anode.

k. Radius and distance of anode.

l. Resistance of single anode.

m. Interference factor of anode.

n. Groundbed resistance

o. Wire resistance.

p. Voltage losses of wire

q. Requirement voltage of rectifier.

r. Rectifier design.

2.5.4 Experimental of Speciment Test

a. Tools

The Tools are used for research such as transformer rectifier, multimeter, soil resistivity meter, accumulator, Cu/CuSO4 for referensial anode.

b. Planning phase.

1) Survey of soil resistance with Wenner Method.

2) Cable laying.

3) Pipe painting.

c. Test phase.

1) Early experiment test.

2) Continuing experiment test.

3. RESULT

This section shows the result of theoritical calculation, experimental speciment test and design of fuel pipeline distribution. It includes the design of pipeline, criteria of coating selection, voltage requirement for rectifier design.

3. 1. Soil Condition

Measurement of soil condition is used for the control of corrosion of buried structure. It is used for finding the value of soil resistivity. It is used both for estimation of expected corrosion rates and for the design of cathodic protection systems.

Measurement of soil condition is done on 3

[DOI: 10.22068/ijmse.14.2.41]

Table 2. Result of Soil Resistance

No		a (cm)	V (mV)	I (mA)	R (Ω)	ρ (Ω-m)	Average ρ (Ω-m)	Soil condition
Location	Test							
1	1	50,0000	1,8100	1,0300	1,7573	5,5179	13,7304	gray lawn soil brownwish
	2	100,0000	1,9200	1,0600	1,8113	11,3751		
	3	200,0000	2,0700	1,0700	1,9346	24,2983		
2	1	50,0000	1,9300	1,0200	1,8922	5,9414	13,2972	gray lawn soil yellowish
	2	100,0000	1,8900	1,0400	1,8173	11,4127		
	3	200,0000	1,9200	1,0700	1,7944	22,5376		
3	1	50,0000	1,7800	1,0300	1,7282	5,4264	13,6525	brown gray without lawn soil less rocky
	2	100,0000	1,9400	1,0400	1,8654	11,7146		
	3	200,0000	2,0100	1,0600	1,8962	23,8166		
average of soil resistance value (ρ) =					13,5601 (Ω-m)			

(three) locations. Determination of location is based on soil quality, soil structure and distance from the sea. In every location, measurement has done three times with distance variation among pins 0.5 metre, 1 metre and 1.5 metre, voltage source from accumulator 12 volt 9 ampere DC. The result shows 13.56 **Ω-m** for soil resistance.

3. 2. Theoritic Calculation Design of Main Pipeline Network.

Result of protected current requirement for fuel pipeline distribution system is 6.6035 A with surface range of pipeline will be protecting 800.429 m^2, and 0.825 $\mu A/cm^2$ for current density (I_{corr}).

3. 3. Speciment Value

a. Theoritic calculation speciment.

Base theoritic calculation table upon, available current difference on each pipeline criteria. Pipeline with double coating has smaller about current value, meanwhile pipeline without coating has greater about current value.

Table 3. Main Pipeline Result Data

No	Design Calculation	Result Main Pipeline	Units	No	Design Calculation	Result Main Pipeline	Units
1	Surface range of pipeline	800,4294	m^2	11	distance of anode	8,3482	m
2	Protecting Current Requirement	6,6035	A	12	Resistance of single anode	10,8245	Ω
3	Pipeline resistance	0,0061	$\Omega.m^{-1}$	13	Interference factor of anode	1,0849	
4	Coating conductance	0,0000	$\Omega^{-1}.m^{-1}$	14	groundbed resistance	3,3724	Ω
5	Attenuation constant	0,0001		15	DC resistance of wire (Anoda-PJB)	0,1023	Ω
6	Pipeline characteristic resistance	59,6328	Ω		DC resistance of wire (PJB-TR)	0,1173	Ω
7	Potential shift	0,8561	V (DC)	16	Voltage losses of wire	9,4900	V (DC)
8	Current of anode	0,9420	A	17	requirement voltage of rectifier	33,7595	V (DC)
9	Requirement of total anode	9,1132	piece	18	Rectifier design		
10	Radius of anode	11,9640	m		a. Voltage	42,1994	V (DC)
					b. Current	8,2544	A

[DOI: 10.22068/ijmse.14.2.41]

Table 4. Result of Theoritic Calculation Specimen

No	Design Calculation	Result			Units
		Speciment 1	Speciment 2	Speciment 3	
1	Soil resistivity data	13,5601	13,5601	13,5601	Ω-m
2	Surface range of pipeline	0,0758	0,0758	0,0758	m^2
3	Protecting Current Requirement	0,0019	0,0012	0,0006	A
4	Pipeline resistance	0,6750	0,6750	0,6750	$\Omega.m^{-1}$
5	Coating conductance	0,1517	0,0000	0,0000	$\Omega^{-1}.m^{-1}$
6	Attenuation constant	0,3199	0,0005	0,0005	
7	Pipeline characteristic resistance	2,1096	1334,2208	1334,2208	Ω
8	Potential shift	-0,8533	-0,8500	-0,8500	V
9	Current of anode	0,0028	0,0028	0,0028	A
10	Requirement of total anode	1,0063	0,6239	0,3321	piece
11	Radius of anode	0,1000	0,4448	0,4448	m
12	distance of anode	0,6279	0,9312	0,9312	m
13	Resistance of single anode	22,7498	22,7498	22,7498	Ω
14	Interference factor of anode	0,8725	1,1380	1,1380	
15	groundbed resistance	19,8502	8,6298	8,6298	Ω
16	Requirement voltage of rectifier	4,8612	4,8337	4,8290	V
17	Rectifier design				
	a. Voltage	6,0765	6,0422	6,0362	V
	b. Current	0,0024	0,0015	0,0008	A

b. Experimental Specimen Test.

For experiment speciment test, previously was taken sample outgrows current point that issued on each speciment pipeline until 17 days. The result is gotten from electricity source the through anode (graphite) and input goes to cathode (pipeline). The result current views table 5.

Table 5. Result of Specimen Test

Day	Current (mA)		
	Speciment 1	Speciment 2	speciment 3
1	1,52	0,96	0,37
2	1,53	1,05	0,54
3	1,71	1,09	0,56
4	1,76	1,11	0,59
6	1,91	1,12	0,62
8	1,91	1,13	0,62
10	1,91	1,14	0,62
12	1,91	1,14	0,62
14	1,91	1,14	0,62
17	1,91	1,14	0,62

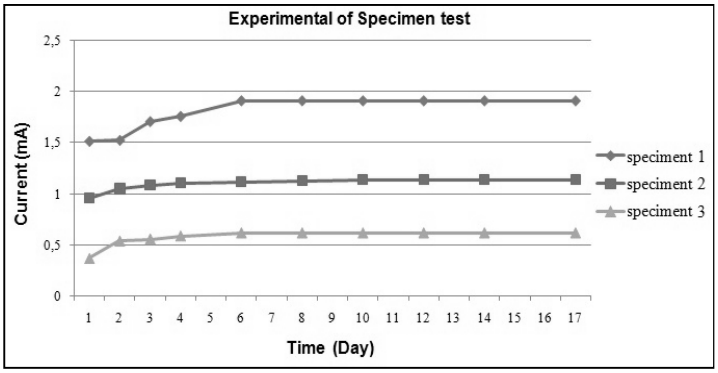

Fig. 2. Result of Specimen Current

[DOI: 10.22068/ijmse.14.2.41]

c. Value of Corrosion Rate

The value of corrosion rate can nake basis to know estimate of design ICCP will be used.

The result showed that design of Impressed Current Cathodic Protection on fuel distribution pipeline network system requires voltage 33,759 V(DC), protection current 6,6035 A(DC) by theoritical calculation and 6,544 A(DC) from pipeline specimen test, with 0,25 mpy for corrosion rate. Transformer Rectifier design needs requirements 45 V with 10 A for current.

Table 5. Result of Specimen Test

Day	Current (mA)		
	Speciment 1	Speciment 2	speciment 3
1	1,52	0,96	0,37
2	1,53	1,05	0,54
3	1,71	1,09	0,56
4	1,76	1,11	0,59
6	1,91	1,12	0,62
8	1,91	1,13	0,62
10	1,91	1,14	0,62
12	1,91	1,14	0,62
14	1,91	1,14	0,62
17	1,91	1,14	0,62

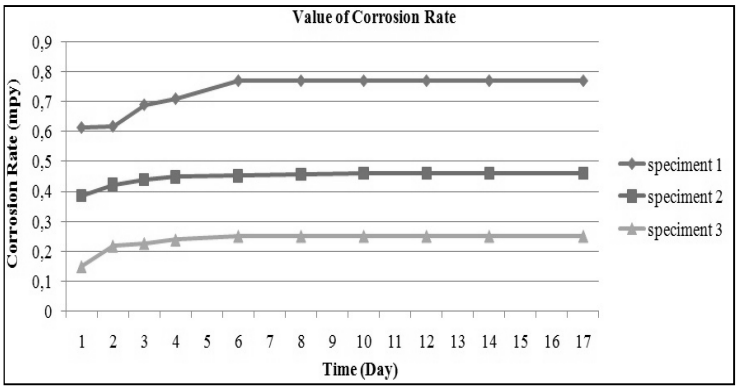

Fig. 3. Corrosion Rate Speciments.

4. DISCUSSION

4. 1. Comparison of Current Value between Theoritical and Experimental Test

Base of data table and figure upon, value of theoritical current to experiment current on speciment 1 that has increase of 1,896 mA becomes 1,91 mA. Whereas on speciment 2 and 3, value of current point has litte decrease. On speciment 2 decreases of 1,175 mA becomes 1,14 mA. On speciment 3 decreases of 0,626 mA becomes 0,62 mA.

Table 7. Value of Theoritical and Experimental Current

No	Name	Speciment 1 (Uncoating)	Speciment 2 (single coating)	speciment 3 (double Coating)	Units
1	Theoritical Current	1,8958	1,1754	0,6256	mA
2	Experimental Current	1,91	1,14	0,62	mA

[DOI: 10.22068/ijmse.14.2.41]

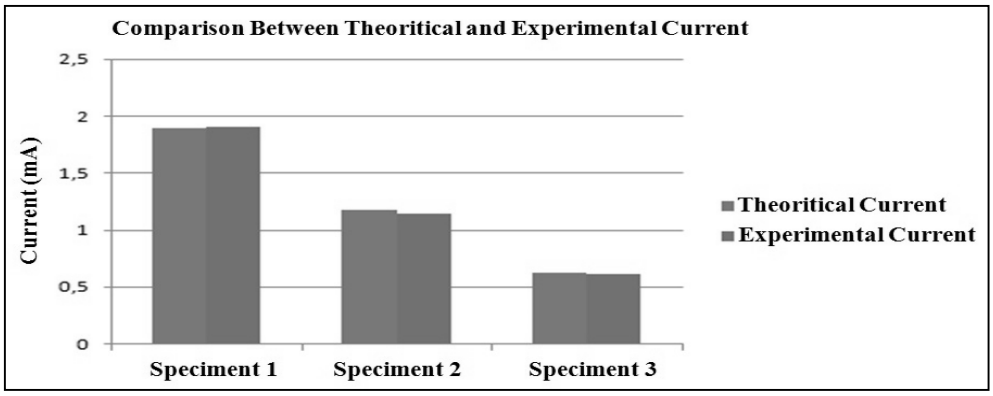

Fig. 4. Comparison of Theoritical and Experiment Current

4. 2. Comparison of Current Density and Corrosion Rate between Speciment Pipeline and Main Pipeline.

Result of current value of main pipeline comes from calculation current density from speciment pipeline and surface range at main pipeline data.

Result of corrosion rate is regarded by pipeline surface range that will be protected and lifetime of pipeline. At the main pipeline 800.429 m^2 for surface range, it has corrosion rate value 0,253 mpy and from experimental pipeline 0,2501 mpy, with clasification of both is outstanding.

Table 8. Value of Current Density

Speciment	Coating Condition	Current		Current Density ($\mu A/cm^2$)
		(mA)	(μA)	
1	Uncoating	1,91	1910	2,5187
2	Single coating	1,14	1140	1,5033
3	double coating	0,62	620	0,8176

Table 9. Current Value of Main Pipeline from Speciment Test

Speciment	Coating Condition	Current Density ($\mu A/cm^2$)	Current value of main pipeline	
			(μA)	(A)
1	uncoating	2,5180	20,161 x 10^6	20,1609
2	single coating	1,5033	12,033 x10^6	12,0332
3	double coating	0,8176	6,544 x 10^6	6,5444

Table 10. Value of Corrosion Rate and Criteria

Name	Current value of main pipeline		Current density ($\mu A/cm^2$)	Corrosion rate (mpy)	Criteria
	(A)	(μA)			
Theoritical Current	6,6035	6,6035 x 106	0,8250	0,2524	Outstanding
Experimental Current	6,5444	6,544 x 106	0,8176	0,2501	Outstanding

[DOI: 10.22068/ijmse.14.2.41]

5. CONCLUSION

The pipeline design has 800.429 m^2 for surface ranging value. This experiment has 3 specimen materials tests with different various coating. So, the experiment result shows the value of current from theoritical calculation and experiment by specimens test. The result of specimen applied from theoritical calculation presents specimen 1 with value $1.89*10^{-3}$ A(DC), specimen 2 presents $1.175*10^{-3}$ A(DC) and specimen 3 shows $6.256*10^{-4}$ A(DC). The result from value of experiment by specimens test shows specimen 1 with value $1.91*10^{-3}$ A(DC), specimen 2 shows $1.14*10^{-3}$ A(DC) and specimen 3 presents $6.2*10^{-4}$ A(DC). So, the best current value that approach from theoritical calculation is specimen material 3 with twice coating variant. It has current value $6.2*10^{-4}$ A and 0,25 mpy for corrosion rate. The result shows that design of impressed current cathodic protection on fuel distribution pipeline system required voltage 33.759 V(DC), protection current 6.6035 A(DC) by theoritical calculation and 6.544 A(DC) from experiment of specimen test. The corrosion rate was observed with 0,25 mpy. The design of Transformer Rectifier needs 45 Volt (DC), current 10 A(DC) with loaded work 70%.

6. ACKNOWLEDEMENT

This research has been supported by Indonesia Naval Technology College (Sekolah Tinggi Teknologi Angkatan Laut/STTAL).

REFERENCES

1. Roberge, P. R., "Handbook of Corrosion Engineering". Mc Graw Hill Company, USA, 1999.
2. Al-Sultani, Khadim F. and Nabat, J. N., "Protect of Underground Oil Pipelines by Using (Al-Sn-Zn) as Sacrificial Anode in Al-Qasim Region". Journal of American Science, 2012, 158-165.
3. Parker, M. E., "Pipeline Corrosion and Cathodic Protection". Gulf Professional , Houston, 1999.
4. Nguyen, C. V., "The Performance of Carbon Fibre Composites as ICCP Anodes for AI". ISRN Corrosion, 2012, 9.
5. Kakuba, G., "The Impressed Current Cathodic Protection System". Technishce Universiteit Eindhoven, Eindhoven, 2005.
6. Al-Himdani, F. F. Mahdi, W. I. and Khuder, A. W. H. "Corrosion Protection of Coated Steel Pipeline Structures using CP Technique". Journal of Engineering and Development, 2005.
7. Choi, B. Y., Kim, J. K. and Oh, J. S., "Cathodic Protection of Onshore Buried Pipelines Considering Economic Feasibility and Maintenance". Journal of Advanced Research in Ocean Engineering, 2016.
8. Ivanov, H., "Corrosion Protection System in Offshore Structure. University of Akron". Ohio, 2016.
9. Ramesh, S. P. M. and Periasamy, V., "Synergic effect of Thiomalic acid and Zinc ions in Corrosion control of Carbon Steel in Aqueous Solution". 2014, Research Journal of Chemical Sciences, 2014, 41-49.
10. Zubaidy, E. A. H. and Tamimi, A. A., "Reduction of Corrosion Process in Steel Bars Using Inhibitor". International Journal of Electrochemical Science , 2012, 6472-6488.
11. Rani, B. E. A. and Basu, B. B. J., "Green Inhibitor for Corrosion Protection of Metals and Alloys: An Overview". International Journal of Corrosion, 2011.
12. Enani, J., "Corrosion Control in Oil and Gas Pipeline". International Journal of Scientific & Engineering Research, 2016, 1161-1164.
13. Payne, S. J. O., "Interactions of Corrosion Control and Biofilm on Lead and Copper in Premise Plumbing". Dalhousie University, Halifax, 2013.
14. A. S. Raja et al., Corrosion Control by Green Solution – An Overview. International Journal of Advanced Research in Chemical Science, 2014, 10-21.
15. Eker, B. and Yuksel, E., "Solutions to Corrosion Caused by Agricultural Chemicals". Trakia Journal of Sciences, 2005, 1-6.
16. El-Lateef, Hany M. A., "Corrosion Protection of Steel Pipelines Againts CO_2 Corrosion – A Review". Chemistry Journal, 2012, 52-63.
17. S. Dapiap, G. Wajiga, M Egwurube, M. Kadzai, and Nathaniel., "Corrosion Control Approach Using Data Mining". International Journal of Computer Science & Information Technology,

[DOI: 10.22068/ijmse.14.2.41]

2015, 53-71.
18. Briggs, T. and Eseonu, Y. M.., "Efficiency of Corrosion Inhibitors on Cathodic Protection System". International Journal of Engineering Trends and Technology (IJETT), 2014.
19. Mainier, F. B., Leta, F. R. and Feliciano, F. F., "Application of Anticorrosive Techniques Compatible with the Environment to Engineering Education". American Journal of Environmental Engineering, 2014, 176-181.
20. Riemer, D. P., "Modelling Cathodic Protection for Pipeline Network". University of Florida, Florida, USA, 2000.
21. Javadi, M., Javidan, J. and Salimi, M., "Cathodic Protection of an underground Pipeline by Photovoltaic Power System using Intelligent Method". International Journal of Renewable Energy Research, 2014, 267-274.
22. Jeong, J. A. and Jin, C. K., "The effect of Cathodic Protection System by Means of Zinc Sacrifial Anode on Pier in Korea". Journal of the Korean Society of Marine Engineering, 2014, 1206-1211.
23. Sekar, A. S. S., Saraswathy, V. and Parthiban, G. T., "Cathodic Protection of Steel in Concrete Using Conductive Polymer Overlays". International Journal of Electrochemical Science, 2007, 872-882.
24. Masli, A. B., "Interaction Between Cathodic Protection and Microbially Influenced Corrosion". University of Manchester, Manchester, 2011.
25. Olusunle, Ogundare, Akinribide, and Adebo., "Use of Sacrifial Anode for Corrosion Protection of Tradition Well Cover". International Journal of Engineering and Technology, 2015, 269-274.
26. Hogan, V. G. E., Lucas, K. E. and Wimmer, S. A., "Shipboard impressed current cathodic protection system (ICCP) analysis". WIT Transactions on State of the Art in Science and Engineering, 2005.
27. Bhuiyan, S., "Effectiveness of Impressed Current Cathodic Protection System in Concrete Following Current Interruption". RMIT University, Singapore, 2015.
28. Hashim, M. S, Mohammed, K. A. and Hamadi, N. J., "Modeling and Control of Impressed Current Cathodic Protection (ICCP) System". J. Electrical and Electronic Engineering, Basra, Iraq, 2014.
29. Christodoulou, C., Glass, G., Webb, J., Austin, S. and Goodier, C., "Assessing the long term benefits of Impressed Current Cathodic Protection". Elvesier, 2010.
30. Janowski, M. and Wantuch, A., "ICCP cathodic protection of tanks with photovoltaic supply". SEED, 2016, 10.
31. Balla, E. E. and Rahmat, M. F., "System Identification Modelling and IMC Basic Control of Impressed Current Cathodic Protection Systems". International Journal on Smart Sensing and Intelligent System, 2013.
32. Sada, B. N. A., Sada, Ali, R. S. and Ali, K. A. M., "Identification and Control of Impressed Current Cathodic Protection System", J. Electrical and Electronic Engineering. Iraq, 2016.
33. Broomfield, J. P., "The application of impressed current cathodic". JCSE, 2004.
34. Fontana, M. G., "Corrosion Engineering". McGraw Hill,Inc, Singapore, 1987.
35. Badford, S. A., "Corrosion Control". CASTI, Canada, 2001
36. Peabody, A. W., "Control of Pipeline Corrosion". NACE International, Houston, 2001.
37. Agarwal, S., "Corrosion: A General Review". International Conference of Advance Research and Innovation, 2015, 181-183.
38. Orazem, M. E., "Underline pipeline corrosion". Woodhead Publising, Cambridge, 2014.
39. NACE, "International. NACE Corrosion Engineer's Reference Book". NACE International The Corrosion Society, Houston, 2002.

[DOI: 10.22068/ijmse.14.2.41]

Predicting the Stiffness of Biaxial Braided Fiber Composites by Incorporation of Carbon Nano Fiber

R. Parimala* and D. B. Jabaraj

* *pdkk4@yahoo.co.in*

Received: April 2016 Accepted: April 2017

Mechanical Department, Dr. M. G. R. Educational and Research Institute University, Maduravoyal, Chennai-95, Tamilnadu, India.

DOI: 10.22068/ijmse.14.2.53

Abstract: *In this study, carbon nano fibers (CNFs) were mixed into epoxy resin through a magnetic stirrer and again mixed using ultra sonicator. Using hand layup technique, biaxial braided fiber composites were prepared with unfilled, 0.2, 0.5 and 1 wt% CNF. Tensile test and shear test were performed to identify the tensile strength and shear strength of the composites. Fractured surface of the tensile specimens were examined by scanning electron microscopy to identify morphologies of nanoparticles. A discrete three layer model was developed for prediction of the tensile modulus and shear modulus of biaxial braided fiber composites. Theoretical and experimental values were compared. The experimental and theoretical results show that the addition of CNF in the epoxy matrix had significant influences on the mechanical properties of biaxial carbon braided fiber composites. CNF inclusion with braided composite promoted the tensile modulus, tensile strength, shear modulus and shear strength up to 0.5wt% of the biaxial carbon braided fiber composites.*

Keywords: *Biaxial braid, CNF, Mechanical properties, stiffness.*

1. INTRODUCTION

Fiber reinforced plastic composites with braid performs posses light weight, improved delamination resistance, strength, stiffness and mechanical properties, compared to conventional type composites. They have played numerous roles in aerospace, marine, sports, biomedical engineering etc. The mechanical properties of braided composites became important to design and fabrication for such applications. Numerical analyses that can accurately model the braided composites are needed for better designing of structural composites. Keeping this in mind, many researchers have studied and tried to predict the stiffness properties of braided composites. Tao Zeng et al [1] were calculated the Young's modulus and Poisson's ratio of 3D braided composites using homogenization theorem. Shunjun et al [2] were carried out micromechanics based study on a series of single and multiple representative unit cell 3-D FE models and predict the compressive strength of 2D triaxial braided carbon fiber polymer matrix composites. Shawn et al [3] were described a model for predicting the energy absorption characteristics of triaxially braided composites tubes. Cui and Yu [4] were presented two-scale method for identifying the mechanics parameters such as stiffness and strength of composite materials. Xiang and Zhi [5] were suggested a micromacromechanical model of unit cells to analyze the dynamic response of 3D-Braided rectangular plates. Anthony et al [6] were presented a macro-cell analytical model to study the piecewise stiffness distribution and then transformed to give global stiffness properties. With the help of the above approaches, a new model has been developed to predict the stiffness and strength of biaxial braided fiber composites by incorporation of carbon nano fiber (CNF).

Polymer matrix composites with CNF reinforcement have become very admired in structural applications because of its excellent mechanical properties. The benefits of CNF reinforcement in polymer matrix composites are apparent in the form of increased stiffness, strength and so on. CNF has attracted much research interests and are widely used for dispersion in epoxy resin due to the high strength and the larger interface of the polymer- CNF interactions. Momchil et al [7] were showed that

[DOI: 10.22068/ijmse.14.2.41]

addition of 0.25wt% carbon nano fibers results in improvement in tensile modulus and strength compared to syntactic foam compositions that did not contain CNF. Yuanxin et al [8] were infused CNF into diglycidylether of bisphenol A and observed that 22.3% improvement in flexural strength of nano composite. Lan et al [9] were provided an in depth study of mechanical behaviors of CNF/epoxy nanocomposites with various contents of CNFs. Mechanical properties of biaxial braided carbon fiber composite with TiO_2 could be effectively adjusted by adding nanoparticle in different percentage [10]. The current improvements in the fabrication techniques ans sympathetic of their mechanical behaviors contribute to the increasing popularity of braided materials [11]. A mechanical property such as impact strength, hardness and double shear of biaxial braided carbon composite with TiO_2 was improved [12].

However, there are few literatures on the mechanical properties of braided fiber/ epoxy laminates. The purpose of the present work is to develop a numerical model for analyzing the stiffness and strength of braided carbon fiber composites with an amount of unfilled, 0.2wt%, 0.5wt% and 1wt% CNFs. The Tensile strength of braided carbon fiber composites with an amount of unfilled, 0.2wt%, 0.5wt% and 1wt% CNFs were investigated. SEM image was examined for the tensile specimen to identify the morphologies of nanoparticles. Then the experimental results are compared with the predicted stiffness behavior.

2. ANALYTICAL MODEL

In this paper, a new model has been introduced for calculation of the stiffness and strength of braided carbon fiber composites with an amount of unfilled, 0.2wt%, 0.5wt% and 1wt% of CNF. The composite properties of a unit cell have been studied. The unit cell consists of two layers for the bias yarns which are aligned in ±45o and a matrix with different percentage of CNF.

The mechanical properties of each layer were calculated by rule of mixture.

$$V_f+V_e+V_h+V_n=1 \quad (1)$$

$$E_{11}=E_{11f}V_f+E_eV_e+E_hV_h+E_nV_n \quad (2)$$

$$E_{22}=1/((V_f/E_{22f})+(V_e/E_e)+(V_h/E_h)+(V_n/E_n)) \quad (3)$$

$$\upsilon_{12}=\upsilon_{12f}xV_f+\upsilon_exV_e+\upsilon_hxV_h+\upsilon_nxV_n \quad (4)$$

$$G_{12}=G_{12f}xG_e+ G_{12f}xG_h + G_{12f}xG_n / (G_{12f}xV_e+ G_{12f}xV_h+G_{12f}xV_n+G_exV_f+G_hxV_f+G_nxV_f) \quad (5)$$

$$\upsilon_{23}=\upsilon_{12}=\upsilon_{13} \quad (6)$$

$$G_{23}=E_{22}/2x(1+\upsilon_{23}) \quad (7)$$

In above formulae, Indices f, e, h and n represent fibre, epoxy, hardener and nanoclay respectively, E_{11} - longitudinal modulus, E_{22} - transverse modulus, υ_{12} - longitudinal poisson's ratio, υ_{23} - transverse poisson's ratio, G_{12} - axial shear modulus and G_{23} - transverse shear modulus.

The stiffness matrix (C_{ij}) can be calculated by considering each composite layer made of transversely isotropic material [13].

$$Cij=\begin{bmatrix} C_{11} & C_{12} & C_{13} & 0 & 0 & 0 \\ C_{12} & C_{22} & C_{23} & 0 & 0 & 0 \\ C_{13} & C_{23} & C_{33} & 0 & 0 & 0 \\ 0 & 0 & 0 & C_{44} & 0 & 0 \\ 0 & 0 & 0 & 0 & C_{55} & 0 \\ 0 & 0 & 0 & 0 & 0 & C_{66} \end{bmatrix} \quad (8)$$

where,

$$C_{11}=(1-(\upsilon_{23})^2)E_{11}/V \quad (9)$$

$$C_{12}=C_{13}=\upsilon_{12}(1+\upsilon_{23})E_{22}/V \quad (10)$$

[DOI: 10.22068/ijmse.14.2.41]

$$C_{23} = (\upsilon_{23}+((\upsilon_{12})^2 x E_{22}/E_{11}))E_{22}/V \quad (11)$$

$$C_{22} = C_{33} = (1-((\upsilon_{12})^2 x E_{22}/E_{11}))\, E_{22}/V \quad (12)$$

$$C_{44}=G_{23}=E_{22}/(2+2\upsilon_{23}) \quad (13)$$

$$C_{55}=C_{66}=G_{12} \quad (14)$$

where

$$V= [(1+ \upsilon_{23})(1- \upsilon_{23}-2((\upsilon_{12})^2 x E_{22}/E_{11})] \quad (15)$$

The braider angle transformation is given by: [14]

$$T_1=\begin{bmatrix} \cos\theta^2 & \sin\theta^2 & 0 & 0 & 0 & 2\cos\theta\sin\theta \\ \sin\theta^2 & \cos\theta^2 & 0 & 0 & 0 & -2\cos\theta\sin\theta \\ 0 & 0 & 1 & 0 & 0 & 0 \\ 0 & 0 & 0 & \cos\theta & -\sin\theta & 0 \\ 0 & 0 & 0 & \sin\theta & \cos\theta & 0 \\ -\cos\theta\sin\theta & \cos\theta\sin\theta & 0 & 0 & 0 & \cos\theta^2-\sin\theta^2 \end{bmatrix} \quad (16)$$

$$T_2=\begin{bmatrix} \cos\theta^2 & \sin\theta^2 & 0 & 0 & 0 & \cos\theta\sin\theta \\ \sin\theta^2 & \cos\theta^2 & 0 & 0 & 0 & -\cos\theta\sin\theta \\ 0 & 0 & 1 & 0 & 0 & 0 \\ 0 & 0 & 0 & \cos\theta & -\sin\theta & 0 \\ 0 & 0 & 0 & \sin\theta & \cos\theta & 0 \\ -2\cos\theta\sin\theta & 2\cos\theta\sin\theta & 0 & 0 & 0 & \cos\theta^2-\sin\theta^2 \end{bmatrix} \quad (17)$$

The stress-strain relation in the global stiffness axes is given as: [15]

$$\{\sigma\} = [T_1]^{-1}\,[C_{ij}]\,[T_2]\,\{e\} \quad (18)$$

Thus, the stiffness matrix of a unit cell in the global coordinate system can be written as:

$$[C]=t^{+e}\,[C_{global}]^{+e} + t^{-e}\,[C_{global}]^{-e} \quad (19)$$

where t^{+e}, t^{-e} are specified as the thickness of each layer to the thickness of the laminate. The thicknesses are assumed to be identical.

Then, the compliance matrix is calculated by inverting the stiffness matrix of a unit cell in Eq. (19):

$$[S]=[C]^{-1} \quad (20)$$

The engineering constants of braided composites can be written as: [16]

$$E_x = 1/S_{11},\ E_y = 1/S_{22},\ E_z = 1/S_{33}$$

$$G_{xy} = 1/S_{66},\ G_{yz} = 1/S_{44},\ G_{xz} = 1/S_{55}$$

$$\upsilon_{xy} = -S_{12}/S_{11},\ \upsilon_{yz} = -S_{23}/S_{22},\ \upsilon_{zx} = -S_{31}/S_{33}$$

3. EXPERIMENTAL METHODS

3. 1. Materials and Specimen Fabrication

Biaxial braided carbon fiber sleeves with ±45°, 4" dia, 15.1 oz/square yard, 3k fiber tow, from ACP composites were used as reinforcement. Bisphenol-A-Diglycidyl-Ether (DGEBA), known as LY556 were chosen as matrix material. When DGEBA is united with Hardener HY951 and nanoparticles, it gives a solvent free curing system. Carbon nanofibers – pyrolitically stripped platelets (conical). >98% carbon basis, D x L 100nm x 20-200 μm were obtained from Sigma Aldrich. An epoxy resin of LY556 and hardener HY951 are mixed in the weight ratio of 10:1 and used as the matrix material for neat, 0.2wt%, 0.5wt% and 1wt% carbon nanofiber nanoparticles. The epoxy in a glass bowl was heated at 75°C to lower the viscosity and the CNF was added. Mixing was conducted in the magnetic hot plate stirrer for 4h at 75°C. The mixture was subjected to sonication using an ultrasonicator at an ultrahigh frequency for 3h to further disperse the CNF while maintaining the resin temperature at 75°C using a hot water bath. The mixture was followed by addition of HY951 and the mixture was stirred well to avoid the formation of bubbles. Braid composites were fabricated using hand layup technique. It is followed by a press machine for 24 h at room temperature. The composites were put in an oven with a post cure treatment for 1h at 100°C. 8layers of biaxial fiber were used to get 3mm

[DOI: 10.22068/ijmse.14.2.41]

thickness of composite material.

3. 2. Tensile Test

Tensile test was performed to determine the stiffness and tensile strength of braided carbon fiber composites with an amount of unfilled, 0.2wt%, 0.5wt% and 1wt% of CNF. A Universal Testing Machine with a gear ratio speed of 2.5mm/min was used to load the specimen, consistent with ASTM D638. The specimens were cut in the dog bone shape with the dimension of 165 x 12.7 x 3mm and gauge length 57mm with radius of 25mm.

3. 3. Double Shear Tests

The double shear strength and shear modulus of the braided composites were measured using Universal Testing Machine according to the ASTM standard method 5616M. The composite specimens with dimensions of 45 x 10 x 3mm were tested. The shear properties were calculated from the tests result. It is compared with theoretical results.

3. 4. Dispersion of CNFs

The dispersion of CNFs was evaluated using Hitachi s3400 scanning electron microscope. To investigate the dispersion of CNFs and to achieve a deeper understanding of the change in microstructure due to CNFs infusion, broken region of tensile specimen was cut with dimension of 10 x 10 mm. The broken surface was observed with the Hitachi s3400 SEM equipment.

4. RESULTS AND DISCUSSIONS

4. 1. Tensile Properties

The tensile modulus and tensile strength from the experiment are presented in Fig. 1 (a) and (b). The stiffness and the tensile strength of the composites were increased by the addition of CNFs up to 0.5wt%. The reason seems that CNFs have high stiffness, strength and bridging effect. However, the stiffness and the tensile strength of the composites were decreased by the addition of CNFs in 1wt%. The reason seems that 1wt% of CNFs were not mixed enough with epoxy resin and forms agglomeration. This shows that high percentage of CNF loading is difficult in the mixing of resin. Due to the above reason, loads were not successfully transferred to the composite material during loading and each ply was fractured individually. The fracture surface of the tensile test specimens are shown in the fig. 2. Fig. 2a indicates the brittle fracture mechanism of neat epoxy resin with biaxial carbon fiber composite. Breakages of fiber were the important failure mode. At tensile strength of 0.103 GPa of neat specimen, fiber breakage was observed vigorously and delamination was also occured. Fig. 2b and 2c composite specimen except 1wt% (fig. 2d) shows improved tensile properties. At tensile strength of 0.245 GPa and 0.269 GPa of 0.2wt% and 0.5wt% composite, the damage of the composite shows ductile nature of the specimen. The significant reduction of 1wt% composite in both failure strength and modulus is linked with a poor dispersion of the high content

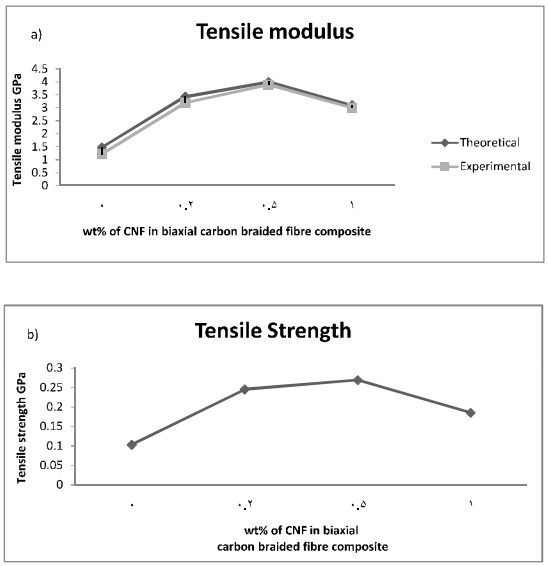

Fig. 1. a) Tensile modulus (stiffness) variation with different wt% of CNF in biaxial carbon fibre composites. b) Tensile strength variation with different wt% of CNF in biaxial carbon fibre composites.

[DOI: 10.22068/ijmse.14.2.41]

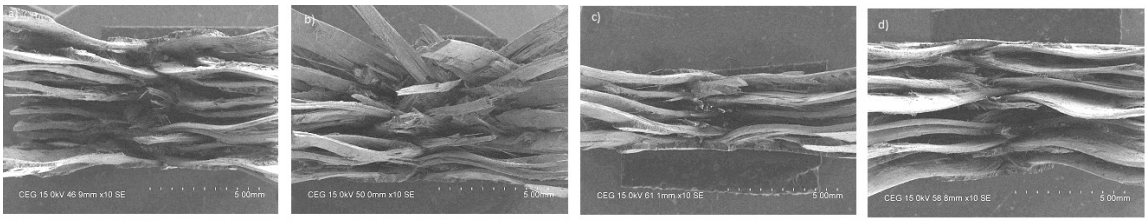

Fig. 2. The fracture surface of the tensile test specimens with a) neat, b) 0.2wt%, c) 0.5wt% and d) 1wt% of CNF in biaxial carbon fibre composites respectively.

level of CNF in the resin shown in Fig. 2d. At tensile strength of 0.185 GPa of 1wt% composite, resin crack and fiber breakage were more. It was observed that an increased viscosity of epoxy due to the addition of high content of CNF made degassing complicate. This allows small void formation and also poor dispersion, agglomeration in the epoxy matrix. Large delamination was observed in the 1wt% of CNFs dispersed composites comparing to the neat, 0.2wt% and 0.5wt%. The reason seems that the CNFs in the composites were aligned in the in-plane direction and it reduced the strength and toughness.

4. 2. Shear Properties

The shear modulus and the shear strength from the experiment are shown in Fig. 3 (a) and (b). The basic parameters affected the shear strength of a quality biaxial carbon braided composite are maximum shear stresses sustainable in the fiber, in the matrix and at the interface. The measured shear modulus and shear strength is agreed well with the predicted. The shear modulus and the shear strength of the composite were increased by the addition of CNFs up to 0.5wt%. The reason seams that proper alignment of biaxial braided fibre and very low void formation during the mixing process. However, the shear modulus and the shear strength of the composites were decreased by the addition of CNFs in 1wt%. The reason seems that 1wt% of CNF were not mixed proper in the epoxy resin and large voids formation by the air trapped adjacent to fibre on the surface of a laminae.

4. 3. Comparison of Tensile Modulus and Shear Modulus with Experimental

The geometrical properties of the biaxial carbon fiber, epoxy resin, hardener and CNF are listed in tables 1 and 2. Table 3 shows the volume fraction of neat, 0.2wt%, 0.5wt% and 1wt% of CNF which is used to predict the tensile modulus and the shear modulus. The geometrical values and volume fractions are applied in the new model to predict the tensile modulus and shear modulus of the composite material. Fig. 1a and 3a are compared the theoretical and experimental

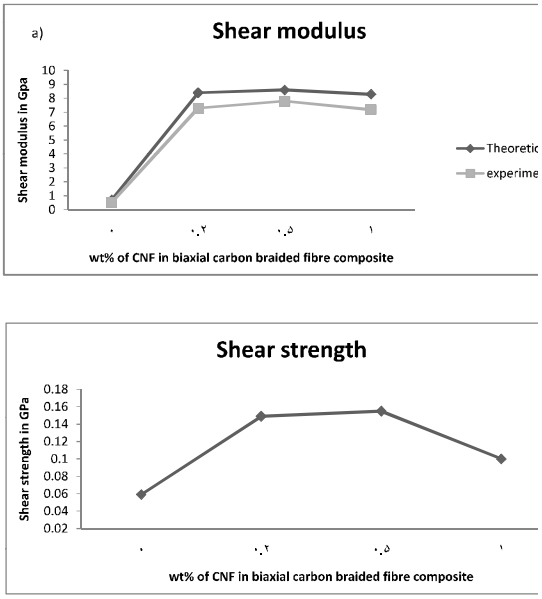

Fig. 3. a) Shear modulus variation with different wt% of CNF in biaxial carbon fibre composites. b) Shear strength variation with different wt% of CNF in biaxial carbon fibre composites.

[DOI: 10.22068/ijmse.14.2.41]

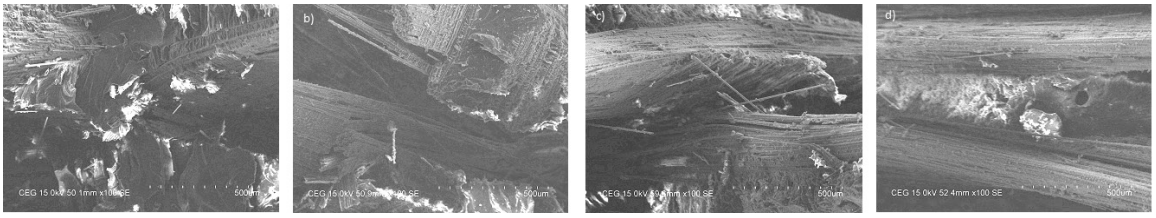

Fig. 4. SEM image a) neat, b) 0.2wt%, c) 0.5wt% and d) 1wt% of CNF in biaxial carbon fibre composites respectively.

results of tensile modulus (stiffness) and shear modulus (stiffness) respectively. The results obtained from the theoretical are nearly in accord with experimental results. The simplicity of this method makes it valid option to predict the stiffness of the composite.

4. 4. SEM Analysis

Scanning electron microscopy image is used to observe neat and dispersion of CNF as shown in Fig. 4. It is quite clear that neat epoxy resin biaxial braided composite shows brittle fracture surface compared to that of the CNF biaxial braided composites. It can be noticed that an ultrasonication at an ultrahigh frequency for 3h led to disperse the CNF uniformly. Only a very few clusters or agglomerations were present in the dispersion of 0.2wt% and 0.5wt% of CNF as shown in fig. 4b and 4c. This shows that the dispersion of the CNF in the epoxy resin is more uniform. But when CNF content is 1wt%, large agglomerations were visible as shown in fig. 4d. The agglomeration can be severe for 1wt% CNF contents due to the reduction of interparticle distances between CNF. As the amount of nanoparticles increases, the inertia of the CNF particles to form agglomeration is also increases. The lack of distribution of CNF is unsettled to that of the epoxy resin and fails to provide proper adhesive force to the fibers. The lower strength could be caused by the formation of CNF agglomeration, poor dispersion and void formation during blending at the high CNF content level. And also, due to lower degree of nanoparticles polymer interaction at higher filler contents. Due to this, interfacial debonding causes during tensile testing and reducing the tensile strength of 1wt% of CNF composite.

5. CONCLUSION

In this paper, the effective tensile modulus (stiffness) and shear modulus are deduced theoretically based on the present model. The effects of CNF loading on the biaxial carbon braided fibre are investigated. The theoretical calculation results are compared to experimental method and excellent results are obtained. The theoretical prediction of the present model shows a good agreement with the experimental data. The different percentage of CNF loading has signicant influences on the stiffness and strength of biaxial carbon braided fibre composites. The stiffness and strength properties in 1wt% were lower than that neat, 0.2wt% and 0.5wt%. This shows that uniform CNF distribution was not easy at high CNF loading. The inclusion of higher CNF (1wt %) content declined the mechanical properties and difficult to disperse, major clustering and entanglement are observed in the SEM images. Moreover, CNF inclusion with braided composite promoted the tensile modulus, tensile strength, shear modulus and shear strength up to 0.5wt% of the biaxial carbon braided fiber composites.

REFERENCES

1. Zeng, T., Wu, L., Guo, L. and Ma, L., "A mechanical model of 3D braided composites with internal transverse crack."" Journal of Composite Materials, 2004, 39, 301-321.
2. Song, Sh., Waas, A. M., Shahwan, Kh. W., Faruque O. and Xiao, X., "Compression response of 2D braided textile composites:

[DOI: 10.22068/ijmse.14.2.41]

Single Cell and multiple cell micromechanics based strength predictions," Journal of Composite Materials, 2008, 42, 2461-2481.

3. Beard, Sha. and Chang, F. K., "Design of Braided Composites for energy absorption", Journal of Thermoplastic Composite Materials, 2002, 15, 3-12.
4. Cui, J. Z. and Yu, X. G., "A two-scale method for identifying mechanical parameters of composite materials with periodic configuration", Acta Mech Sin, 2006, 22, 581-594.
5. Chen, X. D., and Li, Z. M., "Analysis of the dynamic response of 3D-braided rectangular plates on an elastic foundation", Mechanics of Composite Materials, 2008, 44, 607-622.
6. Pickett, A. K., Sirtautas, J. and Erber, A., "Braiding Simulation and Prediction of mechanical Properties", Appl Compos Mater, 2009, 16, 345-364.
7. Dimchev, M., Caeti, R. and Gupta, N., "Effect of carbon nanofibers on tensile and compressive characteristics of hollow particle filled composites", Materials and design, 2010, 31, 1332-1337.
8. Zhou, Y., Pervin, F., Rangari, V. K. and Jeelani, Sh., "Fabrication and evaluation of carbon nano fiber filled carbon/ epoxy composite", Material science and Engineering A, 2006, 426, 221-228.
9. L. H., Sun, Ounales, Z., Gao, X. L., Whalen, C. A. and Yang, Z. G., "Preparation, Characterization and Modeling of carbon Nanofiber/ Epoxy Nanocomposites", Journal of Nanomaterials, 2011, 1-8.
10. Parimala, R. and Jabaraj, D. B., "Carbon braided biaxial fiber with TiO_2 : Mechanical Properties," IEEE 32331, 2014.
11. Parimala, R. and Jabaraj, D. B., "A study on Eglass fiber braided composites", Journal of Harmonized Research in Engineering, 2014, 2, 274- 280.
12. Parimala, R. and Jabaraj, D. B., "Processing and performance of TiO_2 braided biaxial carbon fiber composites", International Journal of Applied Engineering Research, 2015, 10, 212-215.
13. Whitney, J. M., "Structural analysis of laminated anisotropic plates". Technomic 1987.
14. Quek, S. C., Waas, A.M., Shahwan, K. W. and Agaram, V, Analysis of 2-D triaxial flat braided textile composites, Int J Mech Sci, 2003, 45, 1077-96.
15. Shokrieh, M. M. and Mazloom, M. S., "An analytical method for calculating stiffness of two-dimensional tri-axial braided composites", Compos Struct, 2010, 92, 2901- 2905.
16. Jiang, L., Zeng, T., Yan, Sh. and Fang, D., "Theoritical prediction on the mechanical properties of 3D braided composites using a helix geometry model", Compos Struct, 2013, 100, 511-516.

[DOI: 10.22068/ijmse.14.2.41]

Characterization of Co-Fe Magnetic Films Fabricated by Galvano-Static Electrodeposition

Z. Ghaferi[1,2] *, S. Sharafi[1] and M. E. Bahrololoom[3]

* *ghaferi_z@yahoo.com*

Received: December 2016 Accepted: April 2017

[1] Department of Material Science and Engineering, Faculty of Engineering, Shahid Bahonar University of Kerman, Kerman, Iran.

[2] Young Researchers Society, ShahidBahonar University of Kerman, Kerman, Iran.

[3] Department of Material Science and Engineering, Faculty of Engineering, Shiraz University, Shiraz, Iran.

DOI: 10.22068/ijmse.14.2.60

Abstract: *In this research, nanocrystalline Co-Fe coatings were electrodeposited on copper substrate. The influence of current density on different properties of the films at two pH levels was investigated. All the coatings showed nodular structure with rougher morphology at higher current densities. Due to anomalous deposition at higher current density, the amount of iron content increased and reached its maximum value at about 50 wt.% for the coating obtained from pH 5. X-ray diffraction patterns showed hcp structure as the dominant phase. However, by increasing current density at lower pH value, a double phase structure containing fcc+hcp phases was detected. It was observed that current density has a positive effect on grain refinement. However, coarser grains would obtain at lower pH value. Microhardness measurements showed that, there is a direct relationship between grain size and microhardness. Moreover, microstructure in double phase structure films can influence microhardness more dominantly. Vibrating sample magnetometer (VSM) measurements indicated that the saturation magnetic is proportion to deposited iron content and reached its maximum value at about 1512 emu/cm3. It was cleared that grain size, phase structure and chemical composition can affect coercivity of the films effectively.*

Keywords: *Co-Fe, Current density, Microstructure, Microhardness, Magnetic property.*

1. INTRODUCTION

Electrodeposited Co–Fe alloys are important engineering materials used in different industries including communication devices, sensors, actuators, printed circuit boards and magnetic recording heads [1-3]. These materials have high saturation magnetization and Curie temperature, high permeability, low eddy current loss and thermal stability [1, 2].

Many investigations have been carried out for development of these coatings. The influence of homogeneous magnetic fields on internal stress, microstructure, roughness and chemical composition of Co–Fe alloys have been examined by Koza and co-workers [4]. Kim et al. [5] have found that current efficiency obtained from chloride baths is higher than that obtained from sulphate electrolytes and this parameter is decreased by increasing Fe+2 concentration [6].

It has been reported that the presence of internal stress which causes microcracks formation during electrodeposition process affects corrosion resistance, magnetic and mechanical properties of the films [7, 8]. The internal stress is originated from grain size refinement, higher film thickness, increasing iron content and/or fierce hydrogen evolution during electrodeposition process [8-11].

Kockar and co-workers [12] investigated the magnetic properties of Co–Fe alloys as a function of electrolyte pH. Their observations showed that all the films have anisotropic magnetoresistance. However, saturation magnetization of the films reaches its maximum value at about 1597 emu/cm3 at lower pH electrolyte. Lu et al. [13] demonstrated that chemical composition, microstructure and thus magnetic properties of FeCo alloy coatings are influenced by deposition temperature. Their observations showed that Fe content decreased by increasing bath temperature. However, grain size of two phase structure coatings is lower than that obtained from single phase solid solution which is referred

[DOI: 10.22068/ijmse.14.2.41]

to competitive nucleation and growth of the two phases [13]. Mehrizi et al. [3] have also reported the same results. Despite fine magnetic properties, these alloys have high coercivity which causes energy consumption and reduces lifetime of the devices [3, 14-16]. To overcome this problem, reducing the grain size in nanometer scale is recommended [3].

Among different deposition techniques used for fabricating nanostructured materials, electrodeposition can be a good candidate due to its numerous advantages. The most important positive points of this technique are high quality deposition coatings, rapid production at room temperature, low cost and easy control process. In addition, this procedure does not require any vacuum system and secondary processing steps [9, 17, 18].

Although fine magnetic properties and good mechanical features require for fabricating write heads, lower attentions have been devoted for development of these properties as a function of current density [2, 4, 9, 11-13, 15, 19-21]. Thus in the present work, nanocrystalline Co–Fe alloys were fabricated by electrodeposition technique. The influence of current density on chemical composition, microstructure, magnetic property and microhardness of the films at two pH levels was investigated.

2. EXPERIMENTAL DETAILS

2. 1. Materials

Rectangular copper samples with 1 cm^2 surface area were used as cathode. This metal was selected due to easy surface preparation, more accessible, non-magnetic property and high electrical conductivity. Prior to the deposition process, the mechanical polishing of the samples was done up to 3000 grade abrasive paper. Electrodeposition was performed using a digital coulometer (BHP 2056) without agitation and a 430 stainless steel sheet was used as anode surface. The composition of the baths and operating parameters are shown in Table 1. The pH values were adjusted by using dilute H_2SO_4 or NaOH solutions.

2. 2. Methods

The surface morphology and compositional analysis of the coatings were studied by a scanning electron microscope (SEM model WEGA/TESCAN) coupled with an energy dispersive spectrometer (EDS) respectively. To

Table 1. chemical composition of the baths and some deposition conditions for Co-Fe alloys

Bath composition	**Concentration (M)**
$CoSO_4.\ 7H_2O$	0.20
$FeSO_4.\ 7H_2O$	0.20
H_3BO_3	0.40
Na_2SO_4	0.70
L-ascorbic acid	0.05
Electrodeposition parameters	**value**
Current density (mA/cm^2)	10, 20, 35, 50
pH	3, 5
Temperature (°C)	25
Electric charge passed ($colomb/cm^2$)	50

[DOI: 10.22068/ijmse.14.2.41]

evaluate the film thickness, a Motic optical microscope was used. The structural analysis and the grain size measurement were carried out by X-ray diffraction (XRD) technique using Cu Kα radiation (BRUKER/D8 ADVANCED diffractometer, 30 kV-30 mA) and the results were interpreted by X-pert high score software. The grain size was calculated from broadening of the cobalt (101) peak using the Scherrer equation [22]:

$$d=0.9\,\lambda/\,\beta\cos\theta \qquad (1)$$

where λ, β and θ are the wavelength of copper (λ =1.5406 A°), the full width at half-maximum of the peak (FWHM) and the diffraction angle respectively. The scan was done between 40–100 degrees with a step size of about 0.03 degrees. Microhardness of the alloy coatings was determined by using a Koopa MH1 microhardness tester at a constant load of about 15 g for 10 s. The reported values were the average number of five random points on the surface of each coating. The magnetic hysteresis loops were obtained with a vibrating sample magnetometer (Meghnatis Daghigh Kavir Co. Iran). The samples were prepared by using a very thin copper foil with 0.5 cm×0.5 cm dimensions. Magnetic measurements were performed at room temperature and a parallel magnetic field of about ±2000 Oe was applied to the film surface.

3. RESULT AND DISCUSSION

3. 1. Chemical Composition and Surface Morphology

Figs. 1(a–d) and 2(a–d) show SEM images of the coatings obtained from different current densities for both pH values. As seen, a nodular morphology is observed for all current densities. Since the rate of nucleation and growth is proportion to current density [23], the number of nodules increases at higher current density which causes rougher morphology under this condition. Similar results have been also reported

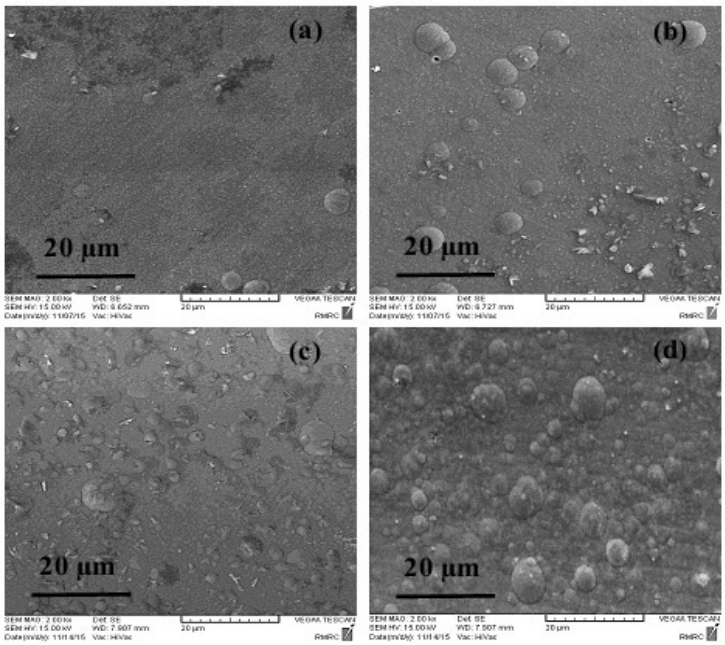

Fig. 1. SEM images of Co-Fe alloy coatings obtained from different current densities and pH=5. The labels (a)-(d) represent current densities i= 10, 20, 35 and 50 mA/cm2, respectively.

[DOI: 10.22068/ijmse.14.2.41]

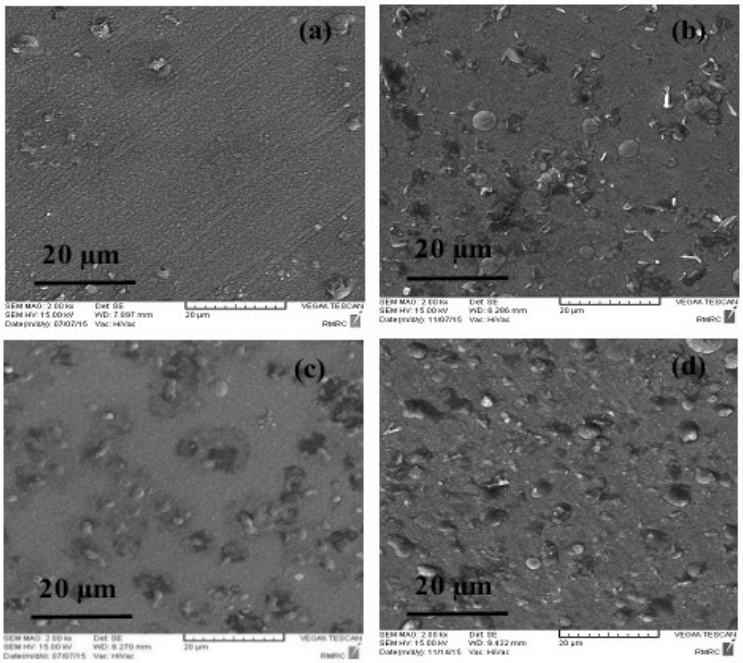

Fig. 2. SEM images of Co-Fe alloy coatings obtained from different current densities and pH=3. The labels (a)-(d) represent current densities i=10, 20, 35 and 50 mA/cm^2, respectively.

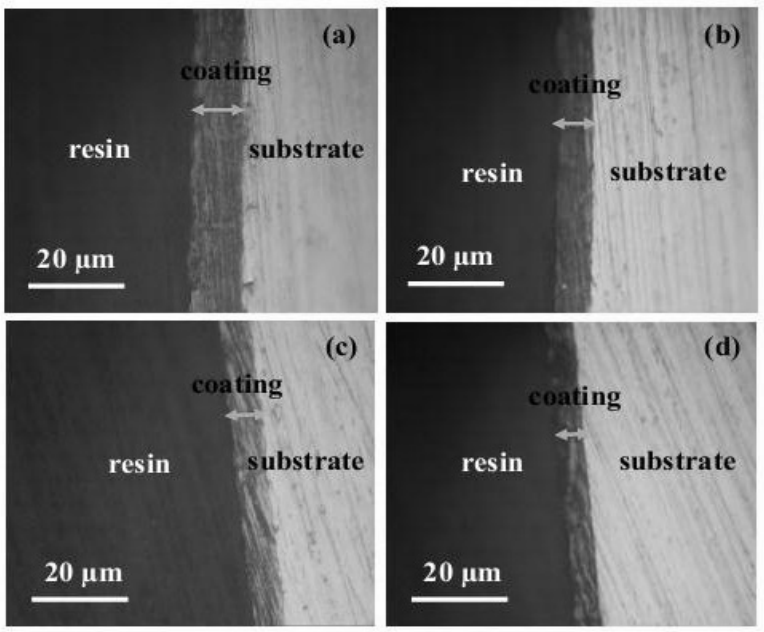

Fig. 3. Optical microscopy images from the cross section of the coatings obtained from different current densities and pH values. The lables (a)-(d) are related to (i=10 mA/cm^2, pH 5), (i=50 mA/cm^2, pH 5), (i=10 mA/cm^2, pH 3), (i=50 mA/cm^2, pH 3) respectively.

[DOI: 10.22068/ijmse.14.2.41]

Table 2. EDS, XRD and VSM data for the coatings obtained from pH=5.

Current density (mA/cm^2)	Fe (wt. %)	Co (wt. %)	Grain size (nm)	Phase structure	M_s (emu/cm^3)	H_c (Oe)
10	35	65	19	hcp	1050	52
20	44	56	15	hcp	1276	41
35	46	54	12	hcp	1348	36
50	50	50	8	hcp	1512	22

Table 3. EDS, XRD and VSM data for the coatings obtained from pH=3.

Current density (mA/cm^2)	Fe (wt. %)	Co (wt. %)	Grain size (nm)	Phase structure	M_s (emu/cm^3)	H_c (Oe)
10	29	71	25	hcp	997	46
20	36	64	19	hcp	1087	31
35	42	58	16	hcp+fcc	1117	24
50	45	55	11	hcp+fcc	1162	16

previously [24]. Optical microscopy images from the cross section of the coatings are shown in Fig. 3 (a-d). It has been reported that, film thickness is theoretically proportion to the electric charge passed during electrodeposition process [3]. Although, the electric charge was kept constant at 50 colomb/cm^2, the real film thickness was not the same. In fact, the film thickness was decreased by increasing current density and this effect became more intense at lower pH value. The difference in film thickness is related to fierce hydrogen evolution and lower current efficiency which occurs at these conditions. These results were also confirmed by other researchers [25-28].

Tables 2 and 3 show chemical composition of the coatings obtained from different current densities for both pH values. The results were reported in weight percentage using EDS analysis. As seen, by increasing current density the amount of iron content was increased which indicates that deposition tends to anomalous fashion under this condition. This expression is used to preferential deposition of the less noble metal compared to the more noble one [10, 18, 27, 29]. To clarify this feature, it must be mentioned that by increasing current density, hydrogen evolution takes place more rapidly at the cathode surface which causes higher pH values near its surface [27]. However, hydroxide ions are dominated species at this condition and the competition adsorption of metal hydroxides causes anomalous deposition [27]. According to Qiang et al. [21] the adsorption tendency of cobalt hydroxide is lower than iron one, which causes higher deposited iron in this condition. This effect became more intense at higher pH electrolytes [25].

[DOI: 10.22068/ijmse.14.2.41]

3. 2. Structural Characterization

XRD patterns of the coatings as a function of current density for two pH levels are shown in Fig. 4. As seen before, EDS analysis confirmed the existence of iron in the coatings but no iron peaks were seen in the XRD spectra. It means that iron was substituted in the cobalt matrix and thus only cobalt structure as the solvent was detected. Similar results have been also reported by other researchers [8, 17, 24, 25, 30, 31].

It has been reported that cobalt has two allotropic structures containing high temperature fcc and low temperature hcp phases. This transition takes place at around 695 K [8]. During electrodeposition, there is not enough time for arrangement of atoms on regular lattice sites. Thus, non-equilibrium phases can be formed during electrodeposition process [13, 24].

As seen in Fig. 4 (a), it is clear that the peaks diffracted from the coatings deposited from different current densities at pH 5 are due to cobalt hcp structure. According to Fig. 4(b), the structure of the coatings obtained from lower current densities was also the same. However, by increasing current density at pH 3, a double phase structure of cobalt containing hcp+fcc phases became evident. Similar results have been also reported by Sakita et al. [10]. According to Nakahara et al. [32], co-deposition of atomic hydrogen with cobalt ions increases the density of faults in hcp structure and thus a metastable fcc phase was detected. It has been reported that lower pH values and/or higher current densities make suitable conditions for deposition of fcc structure [31].

The average grain size of the coatings was calculated by Scherrer equation and the results are summarized in Tables 2 and 3. It has been reported that current density has two contrary effects on the grain size of the coatings. Firstly, by increasing this parameter, surface diffusion of ad-ions to the active growing sites is increased and thus larger grain size would be obtained at this condition. Secondly, by increasing current density, nucleation rate (J) is promoted and thus finer grains would be acquired based on the following equation [23, 26]:

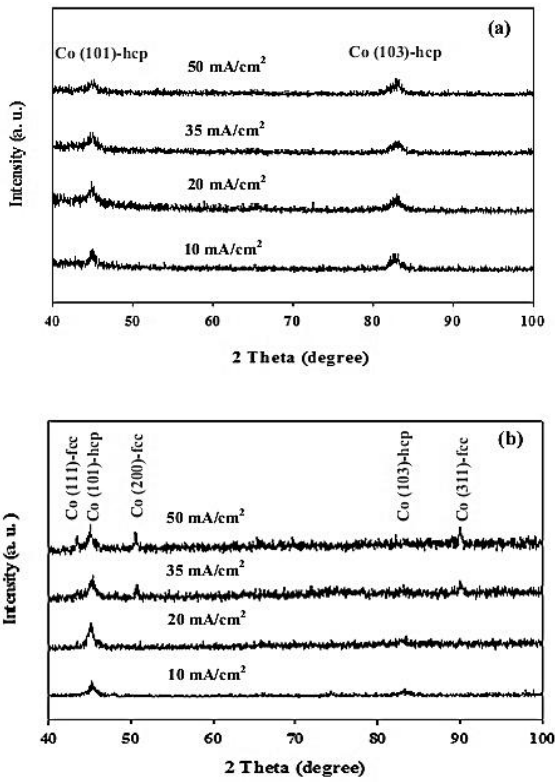

Fig. 4. XRD patterns for Co–Fe alloy coatings obtained from different current densities for (a) pH=5 and (b) pH=3.

$$\lg J = A - \frac{B}{|\Delta\varphi|} \qquad (2)$$

where A and B are constant and $\Delta\varphi$ is the modulus of overpotential. By referring to Tables 2 and 3, it seems that regardless of the electrolyte pH, nucleation rate overcomes the grain growth at higher current densities and thus finer grains would be obtained at this condition. However, the coatings deposited from pH=3 have coarser grains compared to those obtained from the higher pH value. To determine this feature, it can be assumed that hydrogen reduction blocks the nucleation sites more conveniently and this leads to larger grains at lower pH value.

4. MICROHARDNESS OF THE COATINGS

It has been reported that chemical composition, surface defects, crystal orientation,

[DOI: 10.22068/ijmse.14.2.41]

grain size and phase structure can affect microhardness effectively [8, 24, 25, 31, 34-38]. Figure 5 shows microhardness of the coatings as a function of current density for both pH values. As seen, microhardness of the coatings obtained from pH 5 is higher than those obtained from pH 3 initially. This effect may be due to solid solution hardening and higher iron content deposited at pH 5. However, a significant increase in microhardness value for the coatings obtained from pH 3 at higher current densities is related to a double phase structure coatings formed at this condition. Similar results were also reported by other researchers [9, 36].

The strengthening of polycrystalline materials by grain size refinement can be explained by the Hall-Petch equation [38, 39]:

$$H=H_0+kd^{-0.5} \quad (3)$$

where H0 is hardness constant, k is a constant and d is the diameter of grains which is determined by XRD technique. In this model, grain boundaries act as obstacles to dislocations movement [38]. As seen from Fig. 5, microhardness of the coatings obtained from pH 5 has descending trend at higher current densities. It means that the strengthening of material through grain refinement deviates from the normal Hall–Petch equation. This softening effect is related to very small grain size which makes more triple junctions, intercrystalline volume fraction and diffusional creep as reported previously [9, 19, 38]. It has been reported that the deviation from Hall-Petch equation for Co-Fe alloy coatings takes place at around 20 nm grain size [9] which is higher than the reported value in the present investigation.

5. MAGNETIC PROPERTY

Figure 6 illustrates the hysteresis loops of the coatings and the results are summarized in Tables 2 and 3. It has been reported that chemical composition is the main factor responsible for magnetization changes [3, 5, 19]. Since, iron has the highest magnetization compared to other magnetic materials, the variation in this parameter is proportion to deposited iron content [40]. As seen from the mentioned tables, coercivity was decreased at higher current densities. However, the variation in this parameter is related to many factors such as

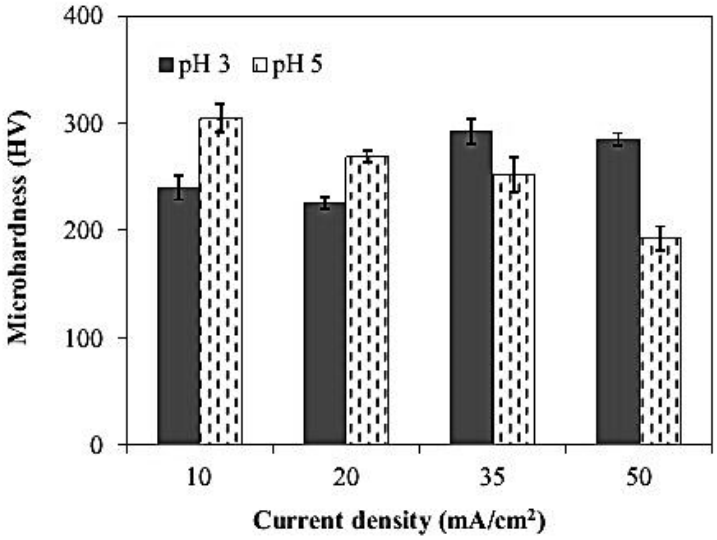

Fig. 5. Microhardness and its error bar for Co–Fe alloy coatings.

[DOI: 10.22068/ijmse.14.2.41]

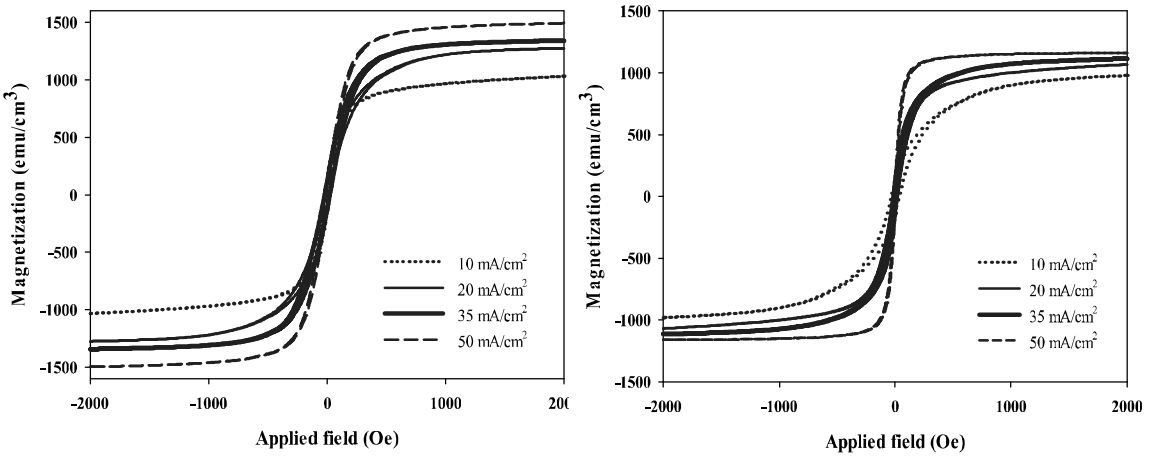

Fig. 6. Hysteresis loops of the coatings obtained from different current densities for (a) pH=5 and (b) pH=3.

chemical composition, surface defects, phase structure, thickness and grain size of the coatings effectively [16, 19, 26].

Based on some documents [41-43], increasing the volume fraction of grain boundaries through grain refinement prevents the domain walls movement and thus higher coercivity would be obtained at this condition. The coercivity is expressed as the following equation [8, 41-43]:

$$H_c \sim 3\sqrt{\frac{kT_cK_1}{aM_s}}\frac{1}{D} \quad (4)$$

where H_c is the coercivity, D the crystallite size, Ms the saturation magnetization, K_1 the manetocrystalline anisotropy, Tc the curie temperature, k the Boltzman constant and a the lattice constant. However, by decreasing the grain size smaller than magnetic exchange length (Lex) which is approximately of the order of tens nanometers, the domain wall effect is eliminated and the exchange interaction of the grains makes the magnetization vectors more parallel to each other [44]. Thus, coercivity can be determined by the following equation [3, 41-43, 45]:

$$H_c \sim \frac{P_cD^6{K_1}^4}{\mu_0 M_s A^3} \quad (5)$$

where P_c is a constant of the order of unity, $\mu 0$ the permeability of free space and A the exchange stiffness constant. The magnetic exchange length is defined as the following equation which is approximately 40 nm for CoFe alloys [3, 41-43, 45]:

$$L_{ex} = \sqrt{\frac{A}{K_1}} \quad (6)$$

As seen previously, grain size of the coatings decreased by increasing current density. Since, the average grain size in this investigation is lower than magnetic exchange length (40 nm), the reduction in this parameter can lead to lower coercivity according to equation 5. It must be mentioned that chemical composition can also affect coercivity of the films effectively. It has been reported that cobalt has higher coercivity compared to other magnetic materials [40]. So the higher cobalt content which was deposited at lower current densities can lead to lower coercivity. Tian et al. [26] have also reported the same results. As seen in previous sections, higher current density and lower pH value provided suitable condition for deposition of fcc phase. It has been reported that fcc phase has lower magnetic anisotropy compared to hcp one which made lower coercivity at this condition [47]. These results are in good agreement with the results obtained here.

[DOI: 10.22068/ijmse.14.2.41]

6. CONCLUSION

In this research, nanocrystalline Co-Fe alloy coatings were prepared by electrodeposition technique. The results showed that by increasing current densities and/or pH value, deposition tends to anomalous fashion and higher iron content would deposit at these conditions. By considering XRD data, it was demonstrated that lower grain size deposits at higher current densities. Furthermore, lower pH values and higher current densities cause suitable situations for deposition of fcc+hcp structure compared to hcp one. Microhardness of the coatings reached its maximum value at about 300 HV. VSM results confirmed that saturation magnetization of the coatings is proportion to deposited iron content and reaches its maximum value at about 1512 emu/cm^3. However, coercivity was changed by chemical composition, microstructure and grain size of the coatings.

REFRENCES

1. Aguirre, M. del C., Farías, E., Abraham, J. and Urreta, S. E., "Co100-xFex magnetic thick films prepared by electrodeposition", J. Alloys Compd. 2015, 627, 393–401.
2. Lu, W., Jia, M., Ling, M., Xu, Y., Shi, J., Fang, X., Song, Y. and Li, X., "Phase evolution and magnetic properties of FeCo films electrodeposited at different temperatures", J. Alloys Compd. 2015, 637, 552–556.
3. Mehrizi, S., Heydarzadeh Sohi, M. and Seyyed Ebrahimi, S. A., "Study of microstructure and magnetic properties of electrodeposited nanocrystalline CoFeNiCu thin films", Surf. Coat. Technol. 2011, 205, 4757–4763.
4. Koza, J. A., Karnbach, F., Uhlemann, M., McCord, J., Mickel, C., Gebert, A., Baunack, S. and Schultz, L., "Electrocrystallisation of CoFe alloys under the influence of external homogeneous magnetic fields—Properties of deposited thin films", Electrochim. Acta 2010, 55, 819–831.
5. Kim, D., Park, D. Y., Yoo, B. Y., Sumodjo, P. T. A. and Myung, N. V., "Magnetic properties of nanocrystalline iron group thin film alloys electrodeposited from sulfate and chloride baths, Electrochim. Acta 2003, 48, 819-830.
6. Tabakovic, I., Riemer, S., Jayaraju, N., Venkatasamy, V., Gong, J., "Relationship of Fe^{2+} concentration in solution and current efficiency in electrodeposition of CoFe films", Electrochim. Acta 2011, 58, 25– 32.
7. Ghaziof, S., Golozar, M. A., Raeissi, K., "Characterization of as-deposited and annealed Cr–C alloy coatings produced from a trivalent chromium bath", J. Alloys Compd. 2010, 496, 164–168.
8. Ghaferi, Z., Sharafi, S., Bahrololoom, M. E., "Effect of current density and bath composition on crystalline structure and magnetic properties of electrodeposited FeCoW alloy", Appl. Surf. Sci. 2015, 355, 766–773.
9. Nik Rozlin, N. M. and Alfantazi, A. M., "Nanocrystalline cobalt–iron alloy: Synthesis and characterization", Mater. Sci. Eng. A 2012, 550, 388–394
10. Sakita, A. M. P., Passamani, E. C., Kumar, H., Cornejo, D. R., Fugivara, C. S., Noce, R. D. and Benedetti, A. V., "Influence of current density on crystalline structure and magnetic properties of electrodeposited Co-rich CoNiW alloys", Mater. Chem. Phys. 2013, 141, 576e581.
11. Shao, I., Romankiw, L.T. and Bonhote, C., "Stress in electrodeposited CoFe alloy films", J. Cryst. Growth 2010, 312, 1262–1266.
12. Kockar, H., Alper, M., Sahin, T. and Karaagac, O., "Role of electrolyte pH on structural and magnetic properties of Co–Fe films", J. Magn. Magn. Mater. 2010, 322, 1095–1097.
13. Lu, W., Huang, P., He, C. and Yan, B., "Compositional and Structural Analysis of FeCo Films electrodeposited at different Temperatures", Int. J. Electrochem. Sci. 2012, 7, 12262 – 12269.
14. Kumari, T. P., Raja, M. M., A. Kumar, S. Srinath, S. V. Kamat, "Effect of thickness on structure, microstructure, residual stress and soft magnetic properties of DC sputtered Fe65Co35 soft magnetic thin films", J. Magn. Magn. Mater. 2014, 365, 93–99.
15. Ricq, L., Lallemand, F., Gigandet, M. P. and Pagetti, J., "Influence of sodium saccharin on the electrodeposition and characterization of CoFe magnetic film", Surf. Coat. Technol. 2001, 138, 278-283.
16. Karpuz, A., Kockar, H., Alper, M., "Effect of film thickness on properties of electrodeposited

[DOI: 10.22068/ijmse.14.2.41]

Ni–Co films", Appl. Surf. Sci. 2012, 258, 5046–5051.
17. Della Noce, R., Benedetti, A. V., Magnani, M., Passamani, E. C., Kumar, H., Cornejo, D. R. and Ospina, C. A., "Structural, morphological and magnetic characterization of electrodeposited Co–Fe–W alloys", J. Alloys Compd. 2014, 611, 243–248.
18. Karpuz, A., Kockar, H., Alper, M., Karaagac, O., Haciismailoglu, M., "Electrodeposited Ni–Co films from electrolytes with different Co contents", Appl. Surf. Sci. 2012, 258, 4005–4010.
19. Tsyntsaru, N., Cesiulis, H., Pellicer, E., Celis, J. P. and Sort, J., "Structural, magnetic, and mechanical properties of electrodeposited cobalt–tungsten alloys: Intrinsic and extrinsic interdependencies", Electrochim. Acta 2013, 104, 94– 103.
20. Lallemand, F., Ricq, L., Deschaseaux, E., De Vettor, L., Bercot, P., "Electrodeposition of cobalt-iron alloys in pulsed current from electrolytes containing organic additives", Surface & Coatings Technology 2005, 197, 10–17
21. Qiang, C., Xu, J., Xiao, S., Jiao, Y., Zhang, Z., Liu, Y., Tian, L. and Zhou, Z., "The influence of pH and bath composition on the properties of Fe–Co alloy film electrodeposition", Appl. Surf. Sci. 2010, 257, 1371–1376.
22. Cullity, B. D., Stock, S. R., Stock, S., "Elements of X-ray Diffraction", Addision-Wesley, London, 2001.
23. Hassani, Sh., Raeissi, K. and Golozar, M. A., "Effects of saccharin on the electrodeposition of Ni–Co nanocrystalline coatings", J. Appl. Electrochem. 2008, 38, 689–694.
24. Ghaferi, Z., Raeissi, K., Golozar, M. A. and Edris, H., "Characterization of nanocrystalline Co–W coatings on Cu substrate, electrodeposited from a citrate-ammonia bath", Surf. Coat. Technol. 2011, 206, 497–505.
25. Ghaferi, Z., Sharafi, S. and Bahrololoom, M. E., "The role of electrolyte pH on phase evolution and magnetic properties of CoFeW codeposited films", Appl. Surf. Sci. 2016, 375, 35–41.
26. Tian, L., Xu, J., Xiao, S., "The influence of pH and bath composition on the properties of Ni-Co coatings synthesized by electrodeposition", Vacuum 2011, 86, 27-33.
27. Oriňáková, R., Oriňák, A., Vering, G., Talian, I., Smith, R. M. and Arlinghaus, H. F., "Influence of pH on the electrolytic deposition of Ni–Co films", Thin Solid Films 2008, 516, 3045–3050.
28. Farzaneh, M. A., Zamanzad-Ghavidel, M. R., Raeissi, K., Golozar, M. A., Saatchi, A., Kabi, S., "Effects of Co and W alloying elements on the electrodeposition aspects and properties of nanocrystalline Ni alloy coatings", Appl. Surf. Sci. 2011, 257, 5919–5926.
29. Pavithra, G. P., Chitharanjan Hegde, A., "Magnetic property and corrosion resistance of electrodeposited nanocrystalline iron–nickel alloys", Appl. Surf. Sci. 2012, 258, 6884–6890.
30. Farzaneh, M. A. Raeissi, K., Golozar, M. A., "Effect of current density on deposition process and properties of nanocrystalline Ni–Co–W alloy coatings", J. Alloys Compd. 2010, 489, 488–492.
31. Fathollahzade, N., Raeissi, K., "Electrochemical evaluation of corrosion and tribocorrosion behavior of amorphous and nanocrystalline cobalt-tungsten electrodeposited coatings", Mater. Chem. Phys. 2014, 148, 67-76.
32. Nakahara, S., Mahajan, S., the influence of solution pH on microstructure of electrodeposited cobalt, J. Electrochem. Soc. 1980, 127, 283-288.
33. Cohen-Hyams, T., Kaplan, W. D., Yahalom, J., "Structure of electrodeposited cobalt", Electrochem. Solid State Lett. 2002, 5(8), C75–C78.
34. He, F., Yang, J., Lei, T. and Gu, C., "Structure and properties of electrodeposited Fe–Ni–W alloys with different levels of tungsten content: A comparative study", Appl. Surf. Sci. 2007, 253, 7591–7598.
35. Nasirpouri, F., Sanaeian, M. R., Samardak, A. S., Sukovatitsina, E. V., Ognev, A. V., Chebotkevich, L. A., Hosseini, M. G., Abdolmaleki, M., "An investigation on the effect of surface morphology and crystalline texture on corrosion behavior, structural and magnetic properties of electrodeposited nanocrystalline nickel films", Appl. Surf. Sci. 2014, 292, 795–805.
36. Sanaty-Zadeh, A., Raeissi, K. and Saidi, A.,

[DOI: 10.22068/ijmse.14.2.41]

"Properties of nanocrystalline iron–nickel alloys fabricated by galvano-static Electrodeposition", J. Alloys Compd. 2009, 485, 402–407.

37. Yun, H. J., Dulal, S. M. S. I., Shin, C. B. and Kim, C. K., "Characterisation of electrodeposited Co–W–P amorphous coatings on carbon steel", Electrochim. Acta 2008, 54, 370–375.
38. Wang, L., Gao, Y., Xu, T. and Xue, Q., "A comparative study on the tribological behavior of nanocrystalline nickel and cobalt coatings correlated with grain size and phase structure", Mater. Chem. Phys. 2006, 99, 96–103.
39. Su, F. h. and Huang, P., "Microstructure and tribological property of nanocrystalline Co–W alloy coating produced by dual-pulse electrodeposition", Mater. Chem. Phys. 2012, 134, 350– 359.
40. Cullity, B. D. and Graham, C. D., "Introduction to magnetic materials", John Wiley & Sons, 2011
41. Bahrami, A. H., Sharafi, S., Ahmadian Baghbaderani, H., "The effect of Si addition on the microstructure and magnetic properties of permalloy prepared by mechanical alloying method", Adv. Powder Technol. 2013, 24, 235-241.
42. Khajepour, M. and Sharafi, S., "Structural and magnetic properties of nanostructured $Fe_{50}(Co_{50})$–6.5 wt% Si powder prepared by high energy ball milling", J. Alloys Compd. 2011, 509, 7729–7737.
43. Sharifati, A. and Sharafi, S., "Structure and magnetic properties of mechanically alloyed $(Fe_{70}Co_{30})_{91}Cu_9$ powder", Mater. Design 2012, 36, 35–40.
44. Zuo, B., Saraswati, N., Sritharan, T. and Hng, H. H., "Production and annealing of nanocrystalline Fe–Si and Fe–Si–Al alloy powders", Mater. Sci. Eng. A 2004, 371, 210–216.
45. Ahmadian Baghbaderani, H., Sharafi, S. and Delshad Chermahini, M., "Investigation of nanostructure formation mechanism and magnetic properties in $Fe_{45}Co_{45}Ni_{10}$ system synthesized by mechanical alloying", Powder Technol. 2012, 230, 241–246.
46. Karpuz, A., Kockar, H. and Alper, M., The effect of different chemical compositions caused by the variation of deposition potential on properties of Ni–Co films, Appl. Surf. Sci. 2011, 257, 3632–3635.
47. Sakita, A. M. P., Passamani, E. C., Kumar, H., Cornejo, D. R., Fugivara, C. S., Noce, R. D. and Benedetti, A. V., "Influence of current density on crystalline structure and magnetic properties of electrodeposited Co-rich CoNiW alloys", Materials Chemistry and Physics 2013, 141, 576-581.

[DOI: 10.22068/ijmse.14.2.41]

The Effect of Various Parameters on Dry Sliding Wear Behavior and Subsurface of Aged Hybrid Metal Matrix Composites Using Taguchi Technique

B. M. Viswanatha[1*], M. Prasanna Kumar[2], S. Basavarajappa[2] and T. S. Kiran[1]

* *vishwanathabm@gmail.com*

Received: April 2016 Accepted: April 2017

[1] Department of Mechanical Engineering, Kalpataru Institute of Technology, Tiptur, India.
[2] Department of studies in Mechanical Engineering, University BDT College of Engineering, Davangere, India.
DOI: 10.22068/ijmse.14.2.71

Abstract: *The effects of applied load, sliding speed and sliding distance on the dry sliding wear behavior of aged Al-SiC_p-Gr composites were investigated. The specimen were fabricated by stir-casting technique. The pin-on-disc wear testing machine was used to investigate the wear rate by design of experiments based on L_{27} using Taguchi technique. Sliding distance was the most important variable that influenced the wear rate followed by sliding speed and applied load. The worn out surfaces were analyzed by SEM and EDS to study the subsurface mechanism of wear. The addition of reinforcements showed improved tribological behavior of the composite than base alloy.*

Keywords: *Composites, Aged, Wear, Subsurface, Taguchi Technique.*

1. INTRODUCTION

Aluminium Metal Matrix Composites (AMMCs) are prominent material to attain high specific strength, high stiffness, low density and good wear resistance compared to the monolithic materials. These are potential replacements for conventional materials in automobile and aerospace applications [1-2]. Several researchers have worked on the improvement of the tribological properties of AMMCs by addition of single ceramic particles viz., SiC_p, Al_2O_3, Gr etc. A few researchers have carried out the research using the combination of the above reinforcements. Increase in the content of SiC_p in aluminium matrix material exhibits good wear resistance. Tjong et al. [3] worked on wear behavior of Al-12% Si alloy reinforced with low volume fraction of SiC_p. The results showed that the addition of low volume fraction of SiC_p is very effective in increasing the wear resistance. Pramila Bai et al. [4] studied the dry sliding wear test of A356 reinforced with 15-25 wt. % of SiC_p. The result revealed that, increase in the content of SiC_p reduced wear.

Ravikiran and Surappa [5] studied the wear behaviour of A356-30 wt. % SiC_p composite as a function of sliding speed. The wear rate of specimen decreases with increasing speed, as the SiC_p is exposed to the specimen surface is increased. Natarajan et al. [6] studied the wear behavior of A356-25SiC_p sliding against automobile friction material. They concluded that the wear rate of MMCs was lower than the cast iron. That makes it a suitable material for brake rotor applications. Wilson and Alpas [7] studied the wear mechanism of A356 alloy and A356-20SiC_p composite. They reported that the addition of SiC_p to A356 aluminium alloy leads to mild wear regime at higher speed and loads, there by inhibiting sever wear. The SiC_p assists the retention of oxide transfer layer on composite sliding surface. It prevents metal to metal contact and keeps wear behavior within the mild wear regime.

The graphite (Gr) used as second reinforcement has to a possible reduction of friction, as solid lubricant imparts good wear resistance to the composites [8]. Akhlaghi and Bidaki [9] studied the effects of addition of lower wt. % (2-5 wt. %) of Gr which exhibited good wear resistance against a higher wt. % (5-20 wt. %) of Gr. Yang et al. [10] studied the tribological properties of A356 alloy with varying Gr of 2, 4, 6 and 8 wt. %. The result showed that 4 and 6 wt. % of Gr particles exhibit

[DOI: 10.22068/ijmse.14.2.41]

lowest wear compared to the 8 wt. %, but sliding speed and normal load had negligible influence on wear rate. Liu et al. [11] studied the wear resistance of Al-Si-Gr composites aged at different temperatures. The wear resistance of aged composites showed better results than as-cast matrix material. Rajaram et al. [12] studied the wear properties of Al-Si alloy reinforced with 3 wt. % of Gr at elevated temperatures. They concluded that, an increase in addition of Gr improved the tribological behaviour when compared with the base alloy.

The addition of SiC_p to Al alloy increases both mechanical and wear resistance but makes machining difficult [13]. The addition of SiC_p along with Gr particles helps to retain the property and reduces the problem of machining. Al matrix reinforced with SiC_p and Gr forms Al-SiC-Gr hybrid composites that improves the tribological characteristics when compared with the base alloy. SiC_p imparts strength and wear resistance, while Gr acts as a solid lubricant [14]. Basavarajappa et al. [15] studied the influence of sliding speed on the extent of subsurface damage on Al-15SiC_p and Al-15SiC_p-3Gr composites. Increasing the sliding speed increases the degree of subsurface deformation.The degree of subsurface deformation and wear rate in Gr composites is less than that of free Gr composites. Suresha and Sridhara [16] reported that the combination of reinforcements of SiC_p and Gr showed better wear behaviour than SiC_p alone. Ames and Alpas [17] studied the wear mechanism of A356 aluminium alloy reinforced with SiC_p and Gr. The wear rate of hybrid composites is significantly lower than the wear rate of base alloy at low and medium loads. Riahi and Alpas [18] observed that the combination of A356-10SiC_p-4Gr revealed good wear resistance than A356-5Al_2O_3-3Gr composites.

Gomez et al. [19] studied the advantage of heat treatment on wear resistance of A6069-SiC_p composite material. It was found that, the heat treated MMCs at T6-7 hrs showed maximum hardness and superior wear résistance. Lin et al. [20] studied the hardness and dry sliding wear of T6 heat treated Al6061-Gr composites and A6069. The tribological characteristic depends on hardness and rate of releasing of Gr particles from the composite specimen. Benal and Shivananad [21] studied the wear characteristics of aged Al6061 hybrid composites. At an aging duration of 5 hrs the composites showed maximum wear resistance. Viswanatha et al. [22] studied the effect of ageing duration on wear behaviour of the aluminium hybrid composites. From the results, A356-9SiC_p-3Gr composites aged at T6-9 hrs showed better mechanical and tribological properties when compared to the base alloy.

Mahdavi and Akhlaghi [23] studied the hardness and tribological behaviour of aged Al6061-SiC_p-Gr composites. The results revealed that hardness of the composites increases with addition of reinforcements. Al-20SiC_p-9Gr gives better tribological property when compared to the other tested specimens. Venkataraman amd Sunderarajan [24] studied the formation of mechanical mixed layer (MML) and its effect of mechanism on wear rate. The MML plays a vital role on the wear behaviour of the composite specimen. The MML protects the surface of specimen from critical sliding conditions. Kiran et al. [25] studied the dry sliding wear behavior of zinc based alloy and composites and the effect of parameters on wear which were investigated using Taguchi technique. Applied load was the most significant parameter to influence the wear volume loss. Dharmalingam et al. [26] investigated the wear parameters by Taguchi method coupled with gray relation analysis to find the performance characteristics. The order of significance on wear rate was wt. % of molybdenum-disulfide followed by sliding velocity and applied load. Sahin [27] optimized the wear behavior of SiC_p reinforced MMCs with two different particles size by Taguchi method. The composite with smaller particle size exhibits severe wear due to easy removal of particles from the matrix. While the larger particles fractured and formed a MML on the surface revealing superior wear resistance. Ravindran et al. [28-30] investigated the effect of applied load, sliding speed and sliding distance on the friction and wear behavior of hybrid composites by Taguchi method. The wear rate increased with an increase in sliding distance and applied load but decreased with increase of Gr content. The most common

[DOI: 10.22068/ijmse.14.2.41]

method of manufacturing process of MMCs are stir cast technique [31-32].

In view of the above literature review, limited works have been carried out to study the effect of ageing on the dry sliding wear behaviour of the composites. The main objective of the investigation was to study the effect of sliding distance, sliding speed and applied load on wear behaviour of base alloy and hybrid composites using Taguchi technique. Taguchi technique is a powerful tool for the design of high quality systems. The Taguchi approach to experimentation provides an orderly way to collect, analyze and interpret data to satisfy the objectives. By using this method, in the Design of Experiments (DOE), one can obtain the maximum amount of information for the amount of experimentation conducted. Taguchi parameter design can optimize the performance characteristics through the setting of design parameters and reduce the sensitivity of the system performance to the source of variation. This is accomplished by the efficient use of experimental runs to the combinations of variables studied. Taguchi technique creates a standard orthogonal array to accommodate the effect of several factors on the target value and defines the plan of experiments. The experimental results are analyzed using analysis of means and variance to study the influence of factors on wear [29]. In addition, the scanning electron microscope (SEM) and electron dispersive spectroscopy (EDS) of worn out surfaces were analysed to know the wear mechanisms.

2. EXPERIMENTAL PROCEDURE

2. 1. Material Fabrication

Fabrication of the base alloy (A356) and composites (A356-9SiC_p-3Gr) was carried out using stir-cast technique. A356 was melted in graphite crucible in an automatic temperature controlled furnace. During the fabrication, 1 wt. % of magnesium (Mg) was added to the liquid metal in order to achieve good bonding between the matrix and reinforcement. The reinforcements were pre-heated to oxidize the surface. The pre-heated reinforcements were added to the stirred liquid metal and the processing temperature was maintained at 750ºC with stirring speed of 500 rpm. The molten metal was poured into the mould box which was pre-heated to avoid the defects like pores and cavities in the specimen. T6–heat treatment was carried-out for the wear specimens at 540ºC for 12 hours and is quenched in 60ºC water. The heat treated

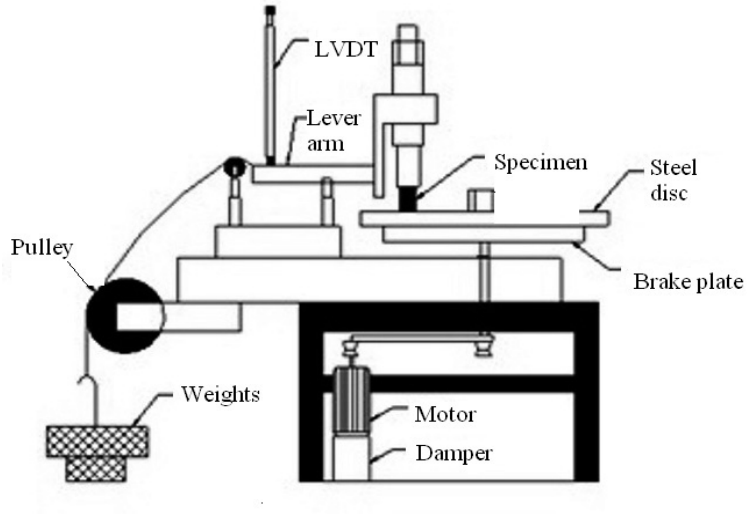

Fig. 1. Pin on disc wear testing machine

[DOI: 10.22068/ijmse.14.2.41]

specimens were aged at 155°C for 9 hours and is quenched in 60°C water.

2. 2. Experimental Procedure

The microstructure and hardness of the specimen was evaluated using Vicker hardness test. The wear testing was carried out on DUCOM pin-on-disc machine to evaluate the dry sliding wear behavior of the composites as shown in Figure 1. The tests were performed as per ASTM G99-95 standard. The cast specimen were turned and polished metallographically for a size of 8 mm diameter and 30 mm height.

The specimen was cleaned with acetone and initial mass was measured using electronic weighing machine with least count of 0.0001g. The specimen was pressed against the rotating EN-32 steel disc with hardness of 65 HRC. The tests were carried out by varying applied load, sliding speed and sliding distance. At the end of each test, the final mass of the specimen was measured. The mass loss was calculated by the difference between the initial and final mass of the specimen. The volume loss was calculated using corresponding density values of the specimen. The wear rate of the specimen was calculated using the ratio of volume loss to corresponding sliding distance. The subsurface of worn out surface was analyzed using SEM. The wear test specimen was cut along its diameter, perpendicular to the specimen surface. The cut surface was polished metallographically to observe the surface behavior (JEOL, JSM-6360).

2. 3. Design of experiment

In the present work, L_{27} orthogonal array (OA) was selected that has 27 rows and 13 columns as shown in Table 1. The experiment consists of 27 tests (each row in the L_{27} OA) and columns are assigned to the parameters. The first column is assigned for applied load (L), second column for sliding speed (S), fifth column for sliding distance (D) and the remaining columns were assigned to the interactions. The experiments were conducted on three parameters at three levels by Taguchi technique. The design parameters with levels are listed in Table 3.7. The desired performance response was calculated by analysis of variance (ANOVA). The main effect plot, interaction plots and regression model were generated. The wear response was conducted with the objective of smaller-the-best.

3. RESULTS

The objective of the present investigation is to evaluate the wear rate of A356 alloy and A356-9SiC_p-3Gr composite by Taguchi method. Both the specimen were heat treated and aged at 9 hours. The parameters applied load, sliding speed, sliding distance and interaction of all variables were studied.

3. 1. Microstructure and Hardness

The particle reinforced composite plays a significant role in the overall strength of the composite. The increase in strength of the matrix invariably enhances the mechanical properties of the composite. Due to this reason the age hardenable base alloy was considered. The heat treatment of base alloy resulted in the removal of dendritic structure and formation of uniform equiaxed grainstructure. The precipitation along the grain boundaries and within the grains are noted to be much finer. However further ageing was carriedout for 9 hrs at 155°C which leads to dissolution of eutectic phase and formation of uniform distribution of fine intermetallic precipitates in the matrix (Fig. 2a). As a result, reinforcements are uniformly distributed within the matrix (Fig. 2b) and produces a maximum hardness (Table 3).

Further increase in the strength of the base alloy by addition of reinfocrements was observed. In composites, reinforcements (SiC_p and Gr) leads to mismatch in thermal stress in the surrounding matrix resulting in increase in dislocation density which increases the precipitation characteristics. The strength was increased due to age hardening in order to develop the acceptable properties. Increase in hardness of the composite was noticable when compared to the base alloy, because of addition of 9 wt. % of SiC_p to the A356-3Gr composites.

The ageing was a phenomenon of precipitation, which is dictated by the combined

[DOI: 10.22068/ijmse.14.2.41]

Table 1. L_{27} Orthogonal array of Taguchi technique

L_{27}, test	1	2	3	4	5	6	7	8	9	10	11	12	13
1	1	1	1	1	1	1	1	1	1	1	1	1	1
2	1	1	1	1	2	2	2	2	2	2	2	2	2
3	1	1	1	1	3	3	3	3	3	3	3	3	3
4	1	2	2	2	1	1	1	2	2	2	3	3	3
5	1	2	2	2	2	2	2	3	3	3	1	1	1
6	1	2	2	2	3	3	3	1	1	1	2	2	2
7	1	3	3	3	1	1	1	3	3	3	2	2	2
8	1	3	3	3	2	2	2	1	1	1	3	3	3
9	1	3	3	3	3	3	3	2	2	2	1	1	1
10	2	1	2	3	1	2	3	1	2	3	1	2	3
11	2	1	2	3	2	3	1	2	3	1	2	3	1
12	2	1	2	3	3	1	2	3	1	2	3	1	2
13	2	2	3	1	1	2	3	2	3	1	3	1	2
14	2	2	3	1	2	3	1	3	1	2	1	2	3
15	2	2	3	1	3	1	2	1	2	3	2	3	1
16	2	3	1	2	1	2	3	3	2	1	2	3	1
17	2	3	1	2	2	3	1	1	2	3	3	1	2
18	2	3	1	2	3	1	2	2	3	1	1	2	3
19	3	1	3	2	1	3	2	1	3	2	1	3	2
20	3	1	3	2	2	1	3	2	1	3	2	1	3
21	3	1	3	2	3	2	1	3	2	1	3	2	1
22	3	2	1	3	1	3	2	2	1	3	3	2	1
23	3	2	1	3	2	1	3	3	2	1	1	3	2
24	3	2	1	3	3	2	1	1	3	2	2	1	3
25	3	3	2	1	1	3	2	3	2	1	2	1	3
26	3	3	2	1	2	1	3	1	3	2	3	2	1
27	3	3	2	1	3	2	1	2	1	3	1	3	2

effect of time and temperature. The precipitation kinetics are strongly influenced by the durations. The similar phenomenon is observed by earlier researcher [37].

3. 2. Statistical Analysis of ANOVA

L27 array was selected and it has 27 rows as shown in Table 4. The wear parameters taken for the experiments are (i) applied load (ii) sliding

[DOI: 10.22068/ijmse.14.2.41]

Table 2. Design parameter with levels

Level	Load L (N)	Sliding velocity S (m/s)	Sliding Distance D (m)
1	10	200	1500
2	30	500	3000
3	50	800	4500

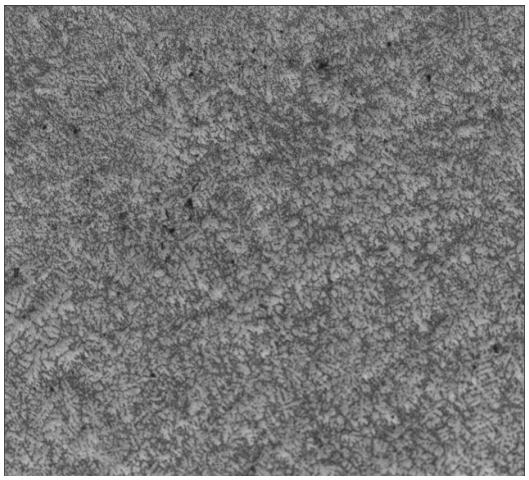

2. (a)

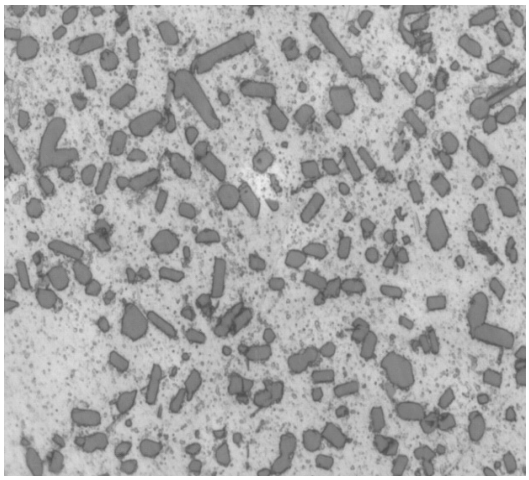

2. (b)

Fig. 2. Microstructure of (a). A356 alloy (b). A356-9SiC$_p$-3Gr

Table 3. Hardness of the specimens

Specimen	Composition	Hardness (VHN)
1	A356	94
2	A356-9SiC$_p$-3Gr	144

speed and (iii) sliding distance. The experiment consists of 27 tests and columns are assigned with the parameters. The first column is for applied load (L), second column is for sliding speed (S), fifth column was assigned to sliding distance (D) and remaining columns were assigned to the interactions. The results of ANOVA for wear rate of base alloy and composites are tabulated in Table 5 and 6 respectively.

F-ratio is calculated by ANOVA, also called as ratio between regression mean square and mean error term. This ratio is important to find the significance of the parameters under the investigation with consideration of all variance and error term at desired significant level. Increased value of F accordingly increases the significance of the parameter shows the contribution of individual parameters such as D, S and L and also interaction of parameters such as S*D, S*L and D*L that influence on wear rate of the materials. From Table 5, sliding distance (P=56.81%) has more contribution to wear rate when compared with the other two parameters sliding speed (P=21.21%), applied load (17.25%) and negligible contribution of interaction D*L (P=1.11%). The effect of interaction is less significant in case of base alloy. Table 6 shows that sliding distance (P= 53.49%) exhibits higher influence on wear rate followed by sliding speed (P=20.21%) and applied load (P=18.32%). Their was no interaction effect on the wear rate of composites. Thus, the distance has predominant effect on wear rate compared to sliding speed and applied load for both base alloy and composite.

[DOI: 10.22068/ijmse.14.2.41]

Table 4. Orthogonal array of Taguchi and experimental results

Expt. No.	Load, L (N)	Sliding speed, S (m/s)	Sliding distance, D (m)	Wear Rate ($mm^3/m*10^{-3}$), A356	Wear Rate ($mm^3/m*10^{-3}$), A356-9SiC$_p$-3Gr
1	10	1.25	1500	11.5	1.8
2	10	1.25	3000	13.4	3.7
3	10	1.25	4500	16.8	5.4
4	30	1.25	1500	12.7	2.1
5	30	1.25	3000	14.4	4.5
6	30	1.25	4500	18.1	6.3
7	50	1.25	1500	13.2	3.6
8	50	1.25	3000	16.8	5.4
9	50	1.25	4500	20.6	7.4
10	10	3.14	1500	13.4	2.3
11	10	3.14	3000	15.8	5.61
12	10	3.14	4500	17.9	7.1
13	30	3.14	1500	13.9	2.8
14	30	3.14	3000	16.9	5.9
15	30	3.14	4500	19.9	7.6
16	50	3.14	1500	14.8	4.7
17	50	3.14	3000	19.9	9.1
18	50	3.14	4500	21.7	10.1
19	10	5.02	1500	14.8	3.8
20	10	5.02	3000	16.2	6.1
21	10	5.02	4500	20.2	8.7
22	30	5.02	1500	15.8	3.9
23	30	5.02	3000	18.5	6.8
24	30	5.02	4500	22.4	9.3
25	50	5.02	1500	17.2	6.1
26	50	5.02	3000	21.5	10.7
27	50	5.02	4500	24.8	11.6

[DOI: 10.22068/ijmse.14.2.41]

Table 5. ANOVA of A356 alloy of wear rate

Factors	SS	DOF	Mean Sq.	T.F.	F	%P
L	52.20	2	26.10	39.60	317.08	17.25
D	168.82	2	84.41	128.09	1025.47	56.81
S	63.85	2	31.92	48.44	387.84	21.21
D*L	5.92	4	1.48	2.24	17.99	1.11
S*L	1.17	4	0.29	0.44	3.55	-
S*D	2.18	4	0.54	0.82	6.63	-
Pooled Error	0.65	8	0.65			3.59
Total	294.808		144.7556			100

S=0.534928, R-Sq=98.1% and R-Sq (adj) =97.5%

Table 6. ANOVA of A356-9SiC_p-3Gr-9hrs of wear rate

Factors	SS	DOF	Mean Sq.	T.F.	F	%P
L	36.57	2	18.28	15.23	121.88	18.32
D	102.12	2	51.06	42.55	340.34	53.49
S	40.09	2	20.04	16.70	133.62	20.21
D*L	1.06	4	0.26	0.22	1.77	-
S*L	2.70	4	0.67	0.56	4.51	-
S*D	2.66	4	0.66	0.55	4.44	-
Pooled Error	1.20	8	1.20			7.95
Total	186.425		91.0036			100

S=0.740448, R-Sq=94.1% and R-Sq adj) =92.4%

[DOI: 10.22068/ijmse.14.2.41]

The measure of degree of fit is based on the coefficient of determination (R2). When R2 approaches to unity, good response model results and it fits the actual data. The value of R-Sq (adj)=97.5% for base alloy and R-Sq (adj)=92.4% for composites are close to unity and hence acceptable.

3. 3. Effects of Variables on the Wear Rate

Fig. 3 (a and b) show the main effects plot for different parameters on wear rate of both base alloy and composite material. As observed from the plot, if the parameter line is nearer to mean line, that parameter tends to have less significant effect on wear rate. The parameter line having steep inclination from the mean line is having the highest significant effect on wear rate. It is observed from Fig. 3 (a and b) that, the parameter line of sliding distance (D) is steeper than other two parameters, namely sliding speed (S) and applied load (L). Hence, the influence of sliding

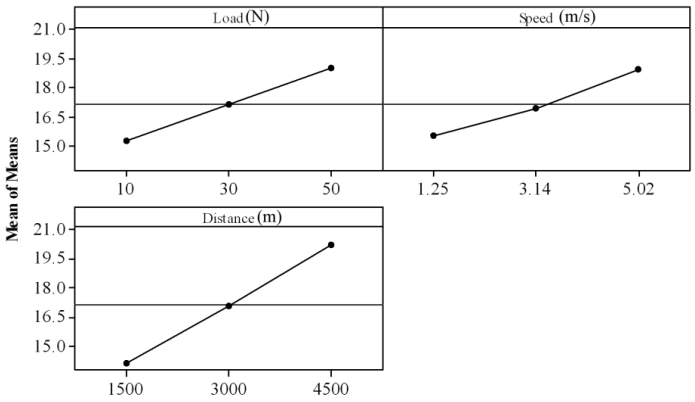

3.(a)

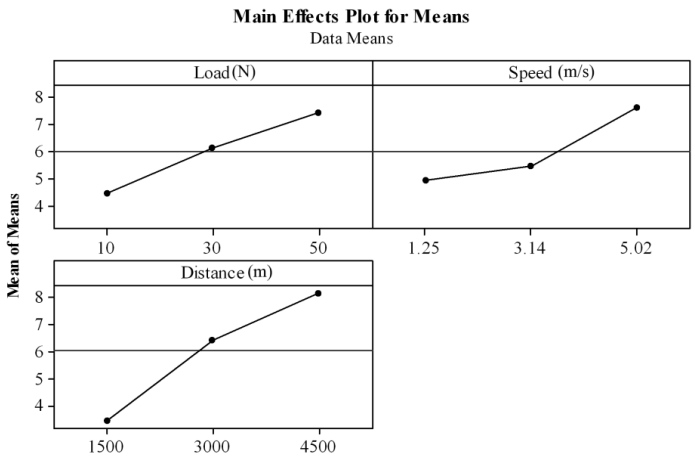

3.(b)

Fig. 3. Main effects plot of different parameters on wear rate of (a) base alloy and (b) composite

[DOI: 10.22068/ijmse.14.2.41]

distance on wear rate is more than the sliding speed and applied load for both the materials. The increase in sliding distance increases the wear rate of the specimen.

The wear rate was more for the base alloy when compared with composite. It indicates that more material was removed from the specimen in the absence of the reinforcement. It is observed from Fig. 3a, that the influence of sliding speed and applied load on wear rate was more in case of base alloy than the composite (Fig. 3b). When sliding speed and applied load were increased in the case of base alloy, it increased the contact surface between the disc and specimen, which in turn increased the friction between them. This resulted in removal of more material from the specimen.

In composite material similar mechanism was observed, but the contact surface between the disc and specimen was reduced as the reinforcements were projected from the specimen surface resulting in less friction. SiC_p acts as a load bearing member which reduces the wear rate of the composite at higher applied load. At higher sliding speed and applied load, graphite acts as a solid lubricant film on tribo-surface which reduces the coefficient of friction between metals. Similar mechanism was observed from earlier researchers [22-25].

3. 4. Interaction Factors on Wear Rate

The interaction plots of variables of the base alloy and composite are shown in Fig 4 (a and b). From Fig. 4a, it is observed that sliding distance has more significant effect on both base alloy and composites followed by sliding speed and applied load.

The sliding distance was the most significant factor influencing the wear rate of the base alloy and composites because, the parameter sliding distance had highest inclination, while the sliding speed and applied load had lowest influence. As observed from Fig. 4b, initially the wear rate decreases and further increasing the applied load and sliding speed which increases the wear rate.

3. 5. Multiple Linear Regression Equation

The multiple linear regression equation was developed using Minitab-16. The linear equations for base alloy and composite material were generated based on individual variable impacts and interaction between the variables. The equations 4.1 and 4.2 represent the regression equations for base alloy and composite material respectively. The positive value of the co-efficient suggests that the dry

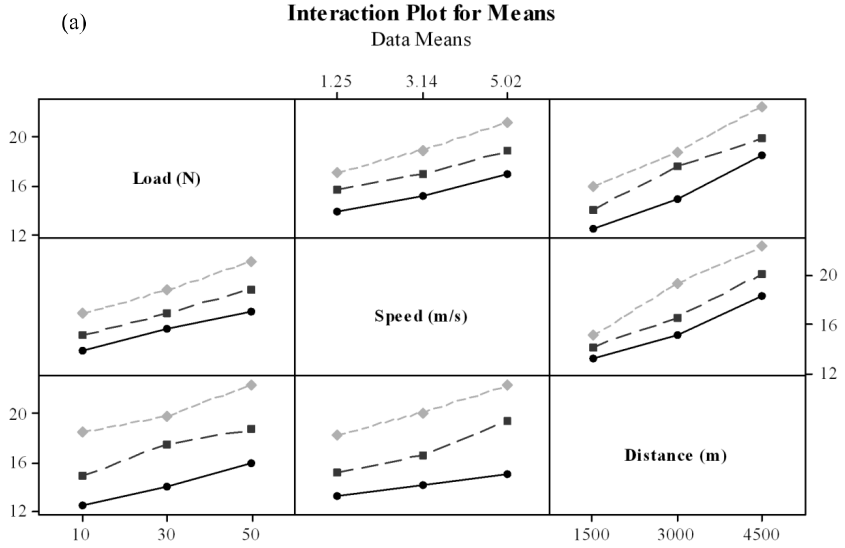

Fig. 4 (a). Interaction factors of wear rate for base alloy

[DOI: 10.22068/ijmse.14.2.41]

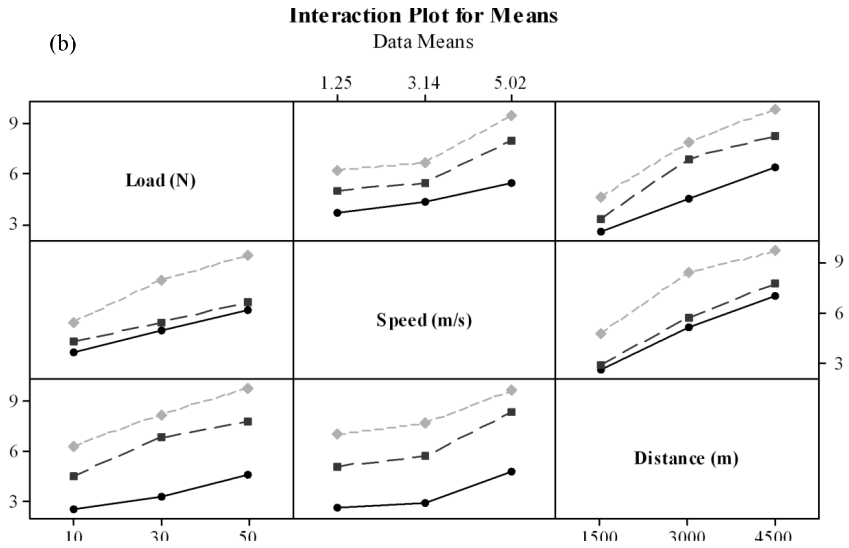

Fig. 4 (b). Interaction factors of wear rate for composite

sliding wear rate increases with increase in their associated variables, where as the negative values of the co-efficient suggest that the wear rate decreases with the increase in associated variables.

Wear (Base Alloy)= 8.15+0.641S+5.3 e^{-3}L+ 1.34e^{-3}D+7.51e^{-3}S*L+4.4e^{-5}S*D+1.9e^{-5}L*D (4.1)

Wear (composite)= -0.78+0.133S+2.57 e^{-2}L+ 1.07e^{-3}D+9.51e^{-3}S*L+1.24 e^{-4}S*D+4e^{-6}L*D (4.2)

All the interactions have positive effect on wear rate. The maximum interaction variable is obtained for applied load. From equations 5.1 and 5.2, the sliding distance impact on base alloy was 0.00134 and for composites it was 0.00107. The magnitude of wear rate of base alloy was more compared to the composite. The parameter associated with sliding speed and applied load and interaction between the parameters is positive. This suggests that, increase in these variables increases the wear rate of the materials for both base alloy and composites.

4. DISCUSSION

4. 1. Wear Mechanism

Fig. 5 shows SEM micrographs of worn out surfaces of base alloy and composite. Fig. 5(a) shows shallow grooves at lower applied load of 10 N and deep grooves (Fig. 5b) were formed as applied load was increased to 50 N, since it causes undergoes plastic deformation leading to severe wear. In base alloy, increasing of sliding speed increases the interfacial temperature between specimen and disc resulting in increase in the oxidation of the base alloy. During sliding, larger shear strain is induced on the surface of the specimen. This shear strain tends to induce the dislocations to glide along slip planes on the surface. This creates a fragmented eutectic phase on the surface and forms hardened surface layer on the specimen. This hardened layer contains a fine mixture of iron and fragmented eutectic phase. The iron particles which originated from the steel disc during wear test (Fig. 5a) were observed. The adhesive nature of wear was observed followed by excessive removal of material from the specimen surface further resulting in delamination (Fig. 5b). The adhesive wear was confirmed by plate like wear debris structure with sharp edges (Fig. 6a).

Fig. 5c shows the surface of composites with

[DOI: 10.22068/ijmse.14.2.41]

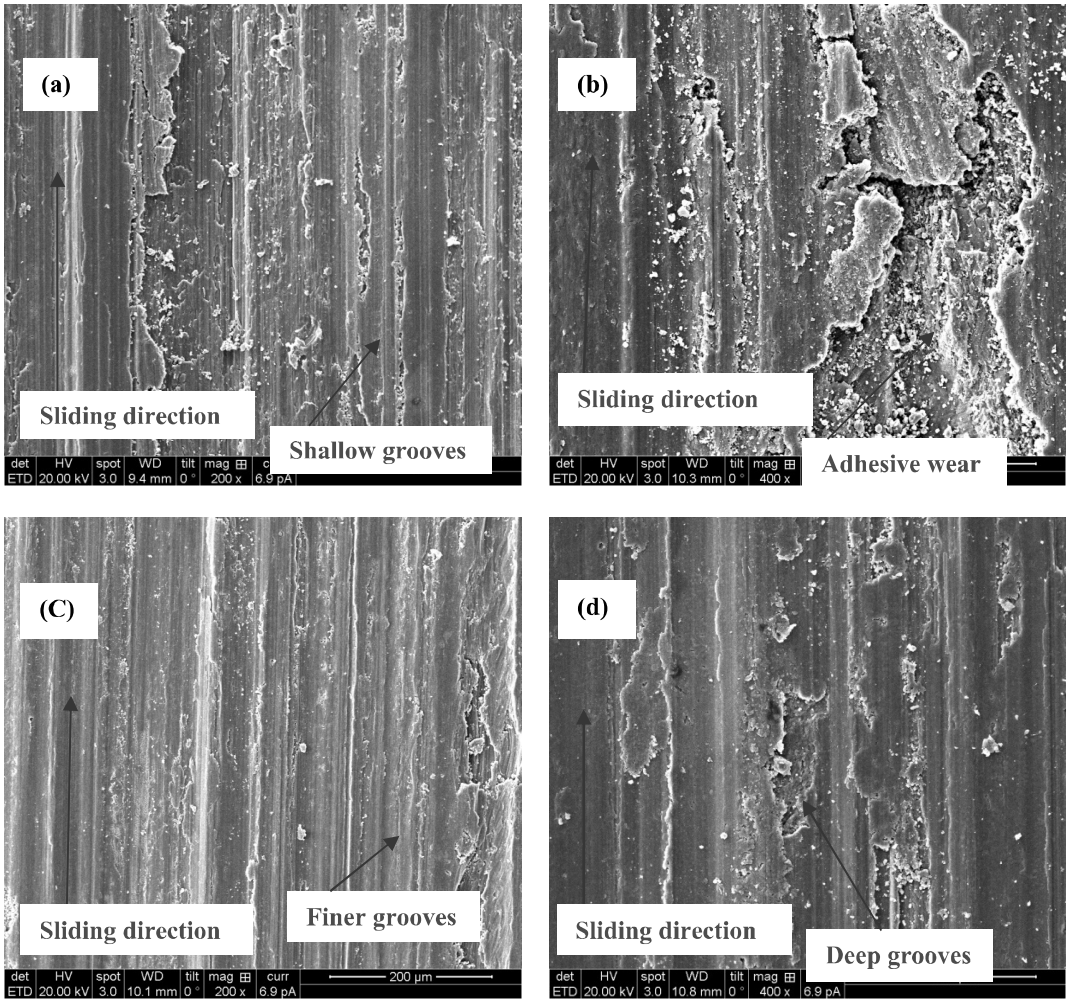

Fig. 5. SEM of worn out surfaces of base alloy (a). 10 N (b). 50 N and composite (c). 10 N (d). 50 N.

finer grooves and appears to be smooth when compared to the base alloy (Fig. 5a) due to the presence of reinforcements. At lower applied load of 10 N, wear rate of composites was lower when compared with the base alloy. As the applied load was increased to 50 N, the wear rate increased and formed deep grooves on the specimen surface of composite specimen (Fig. 5d). As the applied load was increased for base alloy, the layer formed on the contact surface of specimen was removed due to higher pressure resulting in more wear rate.

While in composites, the quantity of wear rate was low as the hardness of the composites was more than base alloy due to the addition of reinforcements that improves the tribological property of the composites (Table 2). In composites, the presence of SiC_p provides abrasion resistance and smearing of graphite on surface of specimen forms a tribolayer due to self lubricating property.

At an applied load of 10 N the asperities that are not able to resist the shear force deform and fill the valley and part of the asperities fracture. In addition, the projected SiC_p along with graphite detaches itself from the surface of the specimen. As the sliding distance increases, the fractured SiC_p lies between the specimen and steel disc that acts as an abrasive medium. They plough the surface of the specimen causing wear by the removal of small fragments of specimen. Hence, wear rate increases linearly during the initial stage of sliding distance. As sliding distance increases further, SiC_p which are rigidly

[DOI: 10.22068/ijmse.14.2.41]

held on to the specimen are subjected to less wear. The ratio of contact area of the base alloy to that of SiC_p with the counter face decreases. Hence, SiC_p takes more load and resists wear for longer time in comparison to the base alloy. At higher sliding distance, wear rate decreases. This result agrees well with the earlier researchers [33-35].

For the composites, at initial sliding speed (1.25 and 3.14 m/s) the wear rate decreases, but at higher sliding speed (5.02 m/s) the wear rate increases. When SiC_p in the composite specimen wear the steel disc, iron particles from the steel disc forms iron oxides (Fe_2O_3). Due the higher hardness of steel disc compared to the base alloy, the powdered and crushed SiC_p penetrates into the matrix of the composite specimen. However, the SiC_p present inside the matrix will resist the penetration of crushed SiC_p into the matrix [13, 18-25]. disc, oxides of aluminium from the specimen and graphite are mixed forming MML [36-37]. SEM (Fig. 6) shows the wear debris of worn out surfaces of the base alloy and composites.

The smeared SiC_p are crushed at the interface and powders of SiC_p are formed. At places where graphite particles are present, the SiC_p penetrates into the matrix easily due to lower hardness that result in squeezing of graphite particles from the matrix. The smeared graphite particles reduce the friction and heat generation. Fig. 5d shows the smearing of graphite at an applied load of 50 N. The powdered SiC_p along with ferrous oxides from the steel.

The wear debris of base alloy (Fig. 6a) are larger and in the form of thin sheets. This indicates that the base alloy has undergone significant plastic deformation. The wear debris in composites (Fig. 6b) is finer than the base alloy (Fig. 6a). The presence of smaller particles indicates that severe wear was not observed exhibiting mild wear in composite specimen. This is due to the presence of reinforcements that scatter in the matrix material minimizing the size of the wear debris. At longer sliding distance, a stable tribolayer on composite reduces the wear rate. The unstable tribolayer results in metal-to-metal contact that leads to increase in the wear rate of composites.

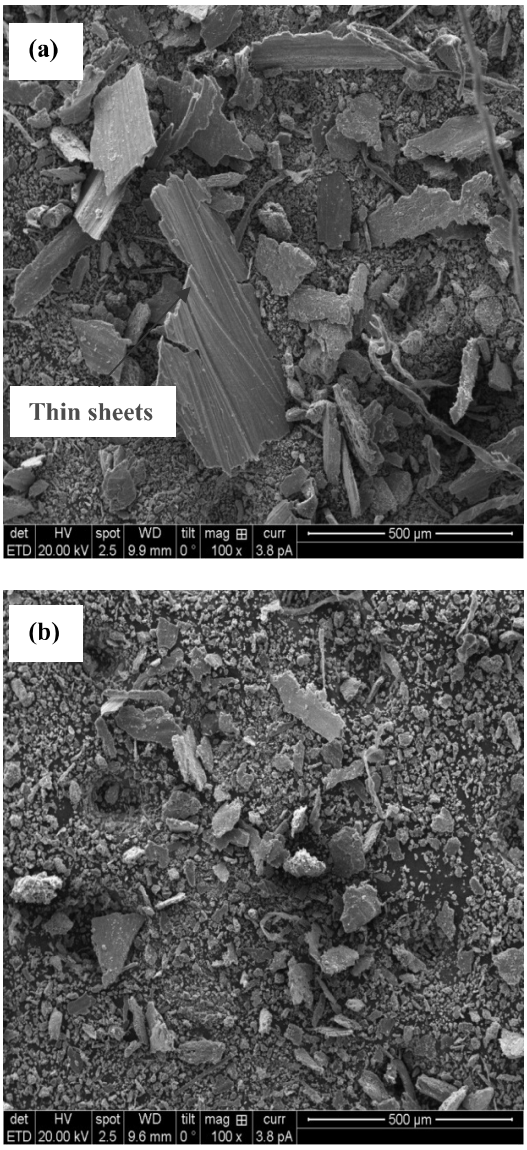

Fig. 6. SEM of wear debris (a). base alloy and (b). composite

EDS analysis of the worn out surface of base alloy and composites is shown in Fig. 7. The EDS analysis of the worn out surfaces of base alloy (Fig. 7a) shows low intensity of Si peak and high intensity of Al peak. The EDS of composites is shown in Fig. 7b. The 'C' peak is observed in Fig. 7b indicating the presence of graphite (solid lubricant). The moderate intensity of the 'Si' peak indicates that fractured SiC_p were noticed on specimen surface. However, a noticeable Fe peak

[DOI: 10.22068/ijmse.14.2.41]

is also observed (Fig. 7b) as the steel counterface material is abraded by the SiC_p. At higher loads, the hard SiC_p fractures and get trapped between steel counter face and the specimen.

The important factor affecting the dry sliding wear is the sliding speed and the associated co-efficient is negative in the regression equation (4.1 and 4.2). This suggests that the dry sliding wear rate decreases with increasing speed within the range of parameters studied. This has been attributed to the formation of MML and thus lowering the wear rate [33-37].

The fractured small particle of SiC_p between the specimen and the rotating disc forms third body abrasion. As the load increases, more SiC_p gets fractured. The brittle fracture of SiC_p in an irregular fashion leads to formation of new edges. The new edged particles will plough the material on the specimen. In case of SiC_p-Gr composite, the smeared graphite between the specimen and the rotating disc along with SiC_p serves to reduce the wear rate.

The iron particles abraded from the disc surface penetrate into the specimen. At higher sliding speed, the fractured particles squeeze out from the surface of composites forming a MML (Fig. 5d). These mechanisms are not present in the base alloy (Fig. 5 a and b). Similar mechanisms were observed by earlier researchers [3, 13, 22, 28 and 33].

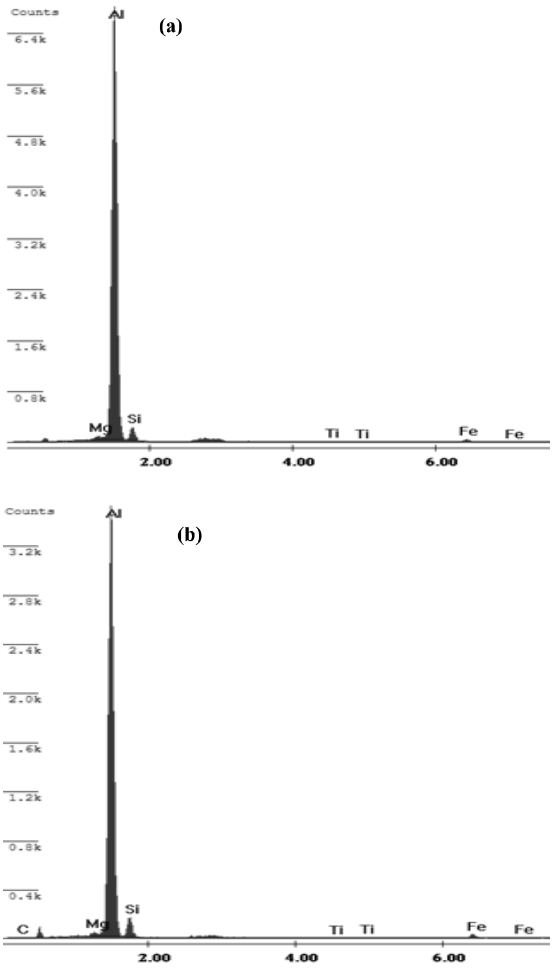

Fig. 7. EDS analysis of worn surfaces (a). base alloy and (b). Composite

4. 2. Sub-Surface Analysis of Worn-Out Surface

A comparison of the sequence of wear mechanism of the base alloy is shown as line diagram in Fig. 8 and SEM of the tested specimen (Fig. 9) is taken as evidence of the process. For the base alloy a large shear strain is induced in the subsurface region during sliding wear process. The magnitude of the surface strain increases with increasing sliding distance, sliding speed and applied load. Increasing of shear strain is closer to the surface; this shear strain induces the dislocation along the slip planes in subsurface region. This region is called as deformation zone as shown in Fig. 8a and it can be observed from the SEM (Fig. 9a). Consequently, eutectic region in the subsurface is fragmented and redistributed near the surface region. The formation of fragmented eutectic phase in the surface region leads to formation of hardened surface layer (Fig. 8b).

The thickness of layer depends on the varying parameters. The hardened layer contains a mixture of iron (Fe) and fragmented eutectic phase. The Fe originating from the steel disc is due to the transfer of metal across the steel disc during dry sliding wear process. That is evident from the SEM subsurface as shown in Fig. 9b. The Fe debris mixes mechanically with Al-Si base alloy during sliding.

Repeated sliding interface between steel disc and specimen results in formation of cracks and leads to delamination from the specimen surface (Fig. 8c) and is evident from the SEM subsurface

[DOI: 10.22068/ijmse.14.2.41]

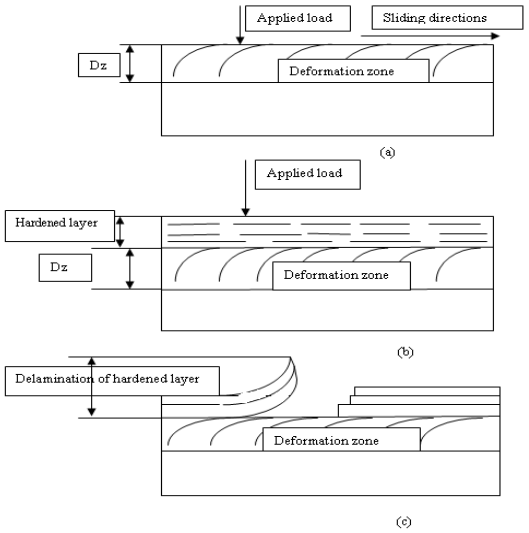

echanism of base alloy (a). formation of deformation zone (b). formati

layer (c). delamination of hardened layer

Fig. 8. Wear mechanism of base alloy (a). formation of deformation zone (b). formation of hardened layer (c). delamination of hardened layer

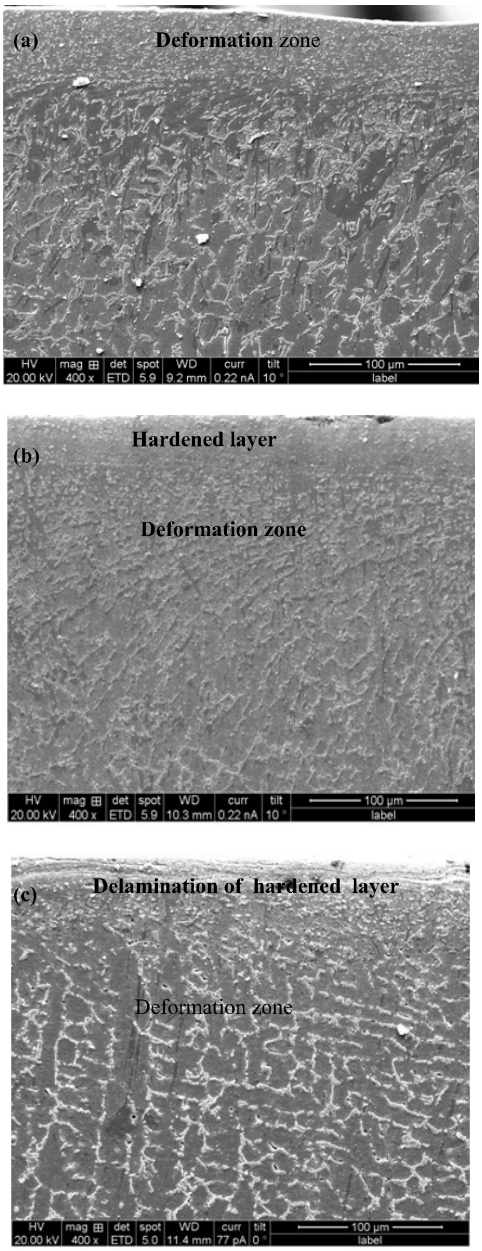

Fig. 9. SEM showing subsurface features in base alloy (a). formation of deformation zone (b). formation of hardened layer (c). delamination of hardened layer

(Fig. 9c). Decreased hardened layer at the top surface forms a delamination hardened layer in the vicinity of the top surface. Apart from this, the cracks are generated and propagate parallel to the surface of the specimen and nucleates at one point which results in removal of material as thin sheet like structure. From the SEM (Fig. 10), the material removed from the specimen adhered at the exit section leading to increase in the wear rate of the base alloy.

The wear mechanism of aged composite is shown in line diagram (Fig. 11) and is evident from the SEM (Fig. 12). In composites, the reinforcement acts as a barrier to the dislocation motion. The dislocation tends to pile up around the reinforcements. The pile-up of dislocations causes the fragmentation of SiC_p owing to the brittle nature of the SiC_P. The fractured SiC_p relives the shear strain in the deformed zone. The smeared Gr on the sub-surface region forms a solid lubricant film thereby resisting plastic deformation in the subsurface region. The fragmented SiC_p and Gr are redistributed in the surface of the hardened layer. This mechanism is shown in Fig. 11. The depth of the hardened layer of the composites is relatively less in comparison with that of the base alloy.

Fig. 11 shows the subsurface of A356-9SiC_p-

[DOI: 10.22068/ijmse.14.2.41]

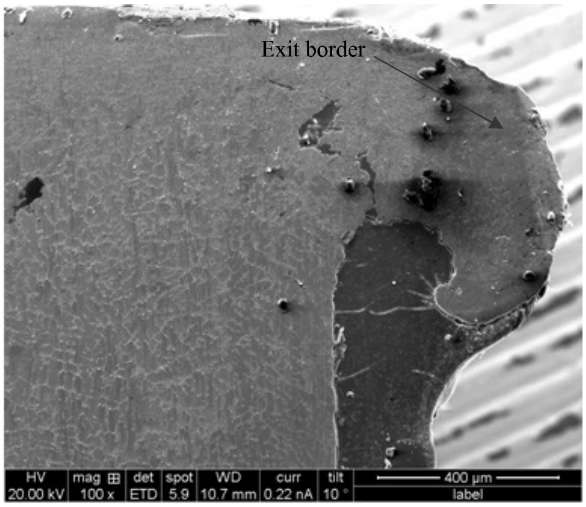

Fig. 10. Worn-out surfaces of base alloy at exit border

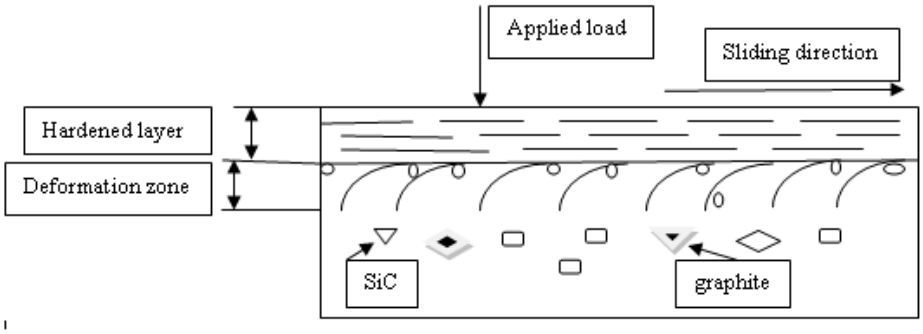

Fig. 11. Wear mechanism of composites

3Gr -9 hrs aged composites at a sliding speed 1.25 m/s where a hardened layer on the surface of the specimen is formed. Further increasing of sliding speed (5.02 m/s) increases the friction between specimen and rotating disc showing low deformation zone beneath the top surface and lower than this surface is the safe zone. The delamination was not observed on the surface of the specimen because of specimen containing reinforcement exhibiting superior hardness. It is evident from the SEM (Fig. 12 and Fig. 13).This results in resistance to flow of material from the specimen which reduces the wear rate of the composites when compared to the base alloy. For the composites, at initial sliding speed 1.25 m/s (Fig. 12) the wear rate decreases, but at higher sliding speed 5.02 m/s (Fig. 13) the wear rate increases.

Fig. 11 shows the smearing of Gr at an applied load of 50 N. The powdered SiC_p along with ferrous oxides from the steel disc, aluminium oxides from the specimen and Gr are mixed, forming MML [13, 33-37]. It is evident from the Fig. 12 and 13. The hardness of the MML is much higher than that of the specimen and the steel disc. This work-hardened layer reduces the wear rate and a stable, thin and hard MML formed on the surface of composite increases the wear resistance of the composite. It is evident from the SEM (Fig. 14) exit section that less flow of material is seen from the specimen surface.

The wear debris of the base alloy and composites is shown in Fig.15. The wear debris as observed from Fig. 15a are larger and is in the

[DOI: 10.22068/ijmse.14.2.41]

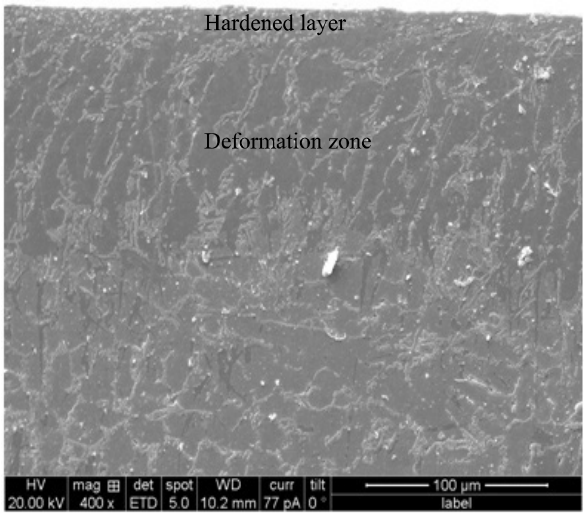

Fig. 12. SEM showing subsurface features in composites at sliding speed of 1.25 m/s

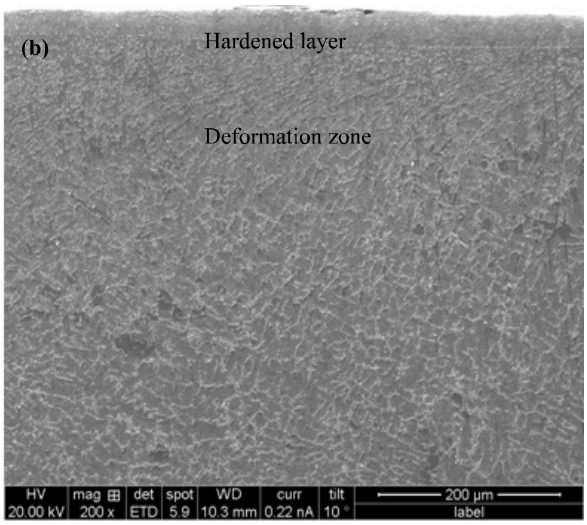

Fig. 13. SEM showing subsurface features in composites at sliding speed of 5.02 m/s

form of thin sheets. This indicates that the base alloy has undergone significant plastic deformation. As the applied load was increased for base alloy, the layer formed on the contact surface of specimen was removed due to higher pressure resulting in more wear rate. While in composites the quantity of wear rate was low. As the hardness of the composites is more than base alloy due to the addition of reinforcements which improves the tribological property of the composites. In composites, the presence of SiC_p provides abrasion resistance and smearing of Gr on sliding specimen surface forms a tribolayer due to self lubricating property.

The wear rate of composites increases with an increase in applied load. During initial stages of sliding, the asperities that are not able to resist the shear forces deform and fill the valley and part of the asperities fracture. In addition, the projected SiC_p along with Gr detaches itself from the surface of the specimen. As the sliding distance increases, the fractured SiC_p lies between the

[DOI: 10.22068/ijmse.14.2.41]

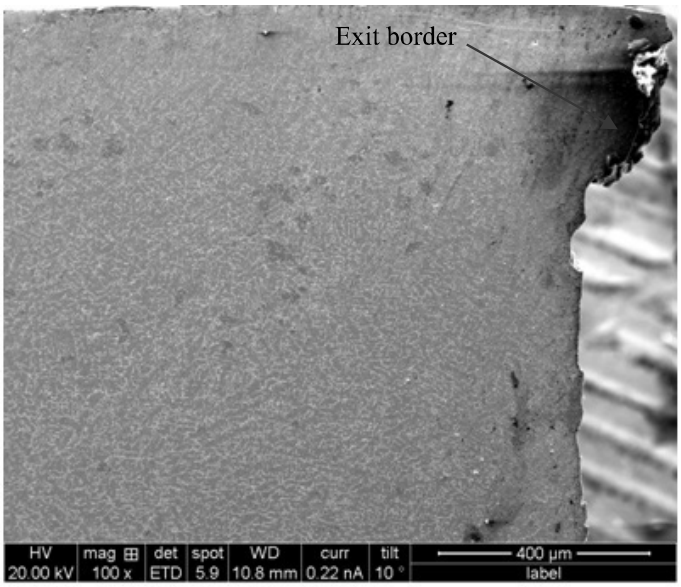

Fig. 14. Worn-out surfaces of composite at exit border

specimen and the counterface and act as an abrasive medium. They plough the surface of the specimen causing wear by the removal of small fragments of specimen material. Hence, wear rate increases linearly during the initial stage of sliding distance. As sliding distance increases further, SiC_p which were rigidly held to the specimen were subjected to less wear. The ratio of contact area of the base alloy to that of SiC_p with the counter face decreases. Hence SiC_p takes more load and resist wear for longer time in comparison to the base alloy. Hence, at higher sliding distance, wear rate decreses. These results agrees well with the general trend of wear behavior as suggested by earlier reasearchers [27-28,35].

The wear debris in composites (Fig. 16) is finer than the base alloy (Fig. 16). The presence of particles indicate that severe wear was not observed exhibiting mild wear in composite specimen. This is due to the reinforcements scattered in matrix material minimises the size of the wear particles. It reduces the wear rate of the composites when compared to the base alloy [33-34]. The wear rate increases for base alloy with an increase of sliding distance. While at longer sliding distance a stable tribolayer on composite

15.(a)

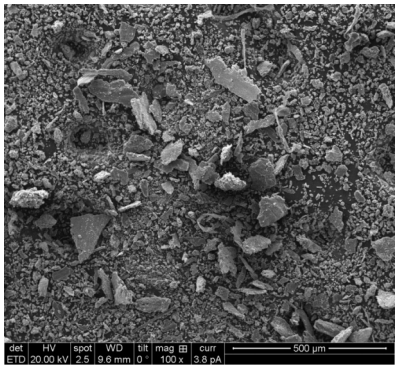

15.(b)

Fig. 15. SEM of wear debris (a) base alloy and (b) composite

[DOI: 10.22068/ijmse.14.2.41]

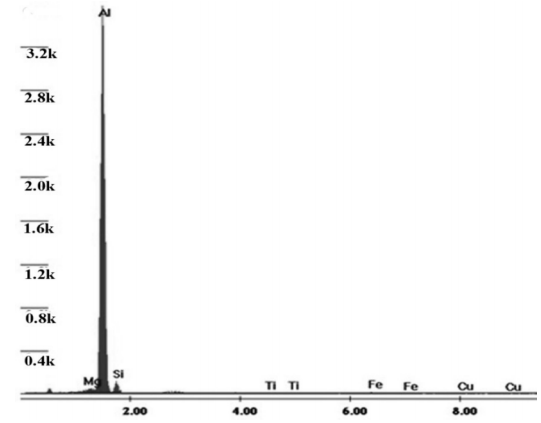

(a)

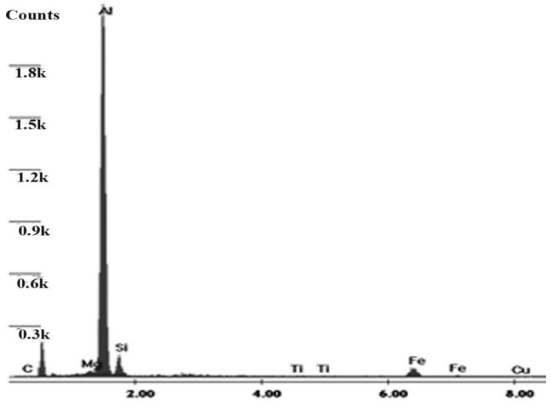

(b)

Fig. 16. EDS analysis of worn out surfaces (a) base alloy and (b) composite

reduces the wear rate. The unstable tribolayer leads to metal-to-metal contact that leads to increase in wear rate of composites.

EDS analysis of the worn out surfaces of base alloy and composites is shown in Fig.16. The EDS analysis of the worn out surfaces of base alloy (Fig. 16a) shows a low intensity of Si peak and high intensity of Al peak. The high Al peak indicates plastic deformation of base alloy during sliding. The EDS spectrum of composites is shown in Fig. 16b. The 'C' peak is observed in Fig. 16b, that indicates the presence of Gr (solid lubricant). The moderate intensity of the 'Si' peak indicates that fractured SiCp was noticed on specimen surface. However, a noticeable Fe peaks is also observed (Fig. 16b) as the steel counter surface material is abraded by the SiC_p. At higher loads, the hard SiC_p fractures and get trapped between steel counter face and the specimen.

The iron from the rotating disc is abraded by the fractured SiC_p, and Fe particles penetrate the surface of the specimen. At higher sliding speed, the fractured particles squeeze out onto the surface of composites forming a mechanical mixed layer (MML) (Fig.16b), these mechanisms are absent in the base alloy (Fig. 16a). The similar mechanism was observed from the earlier researchers [5, 28-37].

5. CONCLUSIONS

The following conclusions were drawn from the experimental data using a statistical technique of ANOVA using Minitab software.

1. The composite aged at T6-9 hrs provides higher hardness and gives MMCs the superior wear resistance and improved tribological behavior when compared to the base alloy.
2. The most significant factor that influences the wear rate of base alloy was sliding distance (56.81%), sliding speed (21.21%) and applied load (17.25%) and interaction factor D*L (1.1%) had nominal effect. For composites sliding distance (53.49%), sliding speed (20.21%) and applied load (18.32%) were the significant factors while there was no significant effect of interactions. The sliding distance is the most significant factor that influences the wear rate for both base alloy and composites.
3. For base alloy a large shear strain is induced in the subsurface region during sliding wear process causing severe plastic deformation.
4. The fractured SiC_p relives the shear strain in the deformed zone. The graphite present in the sub-surface region can form solid lubricant films on the worn-out surfaces thereby resisting plastic deformation in the subsurface region.
5. The powdered SiC_p along with ferrous

[DOI: 10.22068/ijmse.14.2.41]

oxides from the counterface, aluminium oxides from the specimen and graphite are mixed, forming a mechanically mixed layer (MML) reduces the wear rate of the composites.

6. Wear debris reveals that base alloy exhibited thin plate like structures due to the plastic deformation of matrix. In composites fine particles emerged to forms a stable MML which reduces the wear rate of the composites.
7. It is confirmed by EDS analysis of the worn out surfaces of composites that the presence of reinforcements along with iron were observed.

REFERENCES

1. Rohatgi, P. K., "Metal Matrix Composites". Defence Science Journal, 1993, 43 (4), 323-349.
2. Surappa, M. K., "Aluminium Matrix Composites: Challenges and Opportunities". Sadhana., 2003, 28 (1&2), 319-334.
3. Tjong, S. C.,Wu, S. Q. and Liao, H. C., "Wear Behaviour of an Al-12% Si Alloy Reinforced with a low Volume fraction of SiC Particles." Composite Science and Technology., 1997, 57, 1551-1558.
4. Pramila Bai, B. N., "Dry Sliding Wear of A356-Al-SiC_p Composites". Wear., 157, 1992, 295-304.
5. Surappa, M. K, Prasad, S. V. and Rohatgi, P. K., "Wear and Abrasion of Cast Al-Alumina Particle Composites". Wear., 1982, 77, 295-302.
6. Ravikiran, A. and Surappa, M. K., "Effect of Sliding Speed on Wear behaviour of A356 Al-30 wt.% SiCp MMC". Wear., 1997, 206, 33-38.
7. Natarajan, N., Vijayarangan, S. and Rajendran, I., "Wear behaviour of A356/25SiC_p Aluminium Matrix Composites Sliding Against Automobile Friction Material". Wear., 2006, 261, 812-822.
8. Wilson, S. and Alpas, A. T., "Effect of Temperature on the Sliding Wear Performance of Al Alloys and Al Matrix Composites". Wear., 1996, 196, 270-278.
9. Zhan, Y. and Zhang, G., "The role of Graphite Particles in the high Temperature Wear of Copper hybrid Composites Against Steel". Materials and Design., 2006, 27, 79-84.
10. Akhlaghi, F. and Bidaki, A. Z., "Influence of Graphite Content on the Dry Sliding and Oil Impregnated Sliding Wear Behaviour of Al 2024-Graphite Composites Produced by In Situ Powder Metallurgy Method". Wear., 2009, 266, 37-45.
11. Yang, J. B., Lin, C. B., Wang, T. C. and Chu, H. Y., The Tribological Characteristics of A356.2Al Alloy/Gr(P) Composites. Wear., 2004, 257, 941-952.
12. Liu, Y. B., Hu, J. D., Cao, Z. Y. and Rohatgi, P. K., "Wear Resistance of laser Processed Al-Si-Graphite Composites". Wear., 1997, 206, 83-86.
13. Rajaram, G., kumaran ,S., Srinivasa Rao, T. and Kamaraj, M., Studies on high Temperature Wear and its Mechanism of Al-Si/Graphite Composite under Dry Sliding Conditions. Tribology International., 2010, 43 (11), 2152-2158.
14. Jinfeng, L., Longtao, J., Wu, G., Shoufu, T. and Chen, G., "Effect of Graphitic Particle Reinforcement on Dry Sliding Wear of SiC/Gr/Al Composites". Rare Metal materials and Engineering., 2009, 38, 1894-1898.
15. Guo, M. L. T. and Tsao, C. Y. A., "Tribological Behaviour of Self-Lubricating Aluminium /SiC /Graphite Hybrid Composites Synthesized by the Semi-Solid Powder-Densification Method". Composites Science and Technology., 2000, 60, 65-74.
16. Basavarajappa, S., Chandramohan, G., Prasanna Kumar, M., Ashwin, M. and Prabu, M., "Dry Sliding Wear behavior of Al 2219/SiCp-Gr Hybrid Metal Matrix Composites". JMEPEG., 2006, 668-674.
17. Suresha, S. and Sridhara, B. K., "Effect of Addition of Graphite Particulates on the Wear behaviour in Aluminium–Silicon Carbide-Graphite Composites". Materials and Design., 2010, 31, 1804-1812.
18. Ames, W. and Alpas, A. T., "Wear Mechanisms in Hybrid Composites of Graphite-20 Pct SiC in A356 Aluminium Alloy". Metallurgical and Materials Transaction., 1995, 26A, 85-98.
19. Riahi, A. R. and Alpas, A. T., "The role of Tribo- layers on the Sliding Wear behavior of Graphitic Aluminum Matrix Composites". Wear., 2001, 251, 1396-1407.

[DOI: 10.22068/ijmse.14.2.41]

20. Gomez De Salazer, J. M. and Barrena, M. I., "Influence of Heat treatments on the Wear behaviour of an AA6092/SiC_p Composite". Wear., 2004, 256, 286-293.
21. Lin, C. B, Chang, R. J. and Weng, W. P., "A Study on Process and Tribological behaviour of Al alloy/Gr.(P) Composites". Wear., 1998, 217, 167-174.
22. Benal, M. M. and Shivanand, H. K., "Effect of Reinforcement Content and Ageing Durations on Wear Characteristics of Al (6061) based Hybrid Composites". Wear., 2007, 262, 759-763.
23. Viswanatha, B. M., Prasanna Kumar, M., Basavarajappa, S., Kiran, T. S., "Efffect of Ageing on Dry Sliding Wear Behaviour of Al-MMC for Disc Brake". Tribology Industry., 2014, 36 (1), 40-48.
24. Mahdavi Soheil. and Farshad Akhlaghi., "Effect of SiC content on the Processing, Compaction Behavior and Properties of Al6061/SiC/Gr Hybrid Composites". Journal of Materials Science., 2011, 46 (5), 1502-1511.
25. Venkataraman, B. and Sunderarajan, G., "Correlation between the Characteristics of the Mechanically Mixed Layer and Wear behaviour of Aluminium Al-7075 alloy and Al-MMC's". Wear., 2000, 245;22-38.
26. Kiran. T. S., Prasanna Kumar, M., Basavarajappa, S. and Viswanatha, B. M., "Dry Sliding Wear behavior of Heat Treated Hybrid Composites using Taguchi". Materials & Design., 2014, 63, 294-304.
27. Dharmalingam, S., Subramanian, R., Somasundara Vinoth, K. and Anandavel B., "Optimization of Tribological Properties in Aluminum Hybrid Metal Matrix Composites using Gray-Taguchi Method". JMEPEG., 2011, 20 (8), 1457.
28. Sahin, Y., Tribological behaviour of Metal Matrix and its Composite. Materials and Design., 2007, 28, 348-1352.
29. Ravindran, P., Manisekar, K., Narayanasamy, P., Selvakumar, N. and Narayanasamy, R., "Application of Factorial Techniques to Study the Wear of Al Hybrid Composites with Graphite Addition". Materials and Design., 2012, 39, 42-54.
30. Suresha, S. and Sridhara, B. K., "Friction characteristics of Aluminium Silicon Carbide and Graphite hybrid composites. Materials and Design"., 2012, 34, 576-583.
31. Ravikiran, A. and Surappa, M. K., "Effect of sliding speed on wear beahaviour of A356 Al-30 wt.% SiC_p MMC". Wear., 1997, 206, 33-38.
32. Hashim, J., Looney, L. and Hashmi, M. S. J., "Metal Matrix Composites: Production by the Stir Casting Method". Journal of Materials Processing Technology., 1999, 92-93, 1-7.
33. Hashim, J., Looney, L., Hashmi, M. S. J., "The Enhancement of Wettability of SiC particles in Cast Aluminium Matrix Composites". Journal of Materials processing Technology., 2001, 119, 329-335.
34. Basavarajappa, S. and Chandramohan, G., "Application of Taguchi techniques to Study Dry Sliding Wear Behaviour of Metal Matrix Composite". Materials and Design., 2007, 28, 1393-1398.
35. Basavarajappa, S. and Chandramohan, G., "Dry Sliding Wear Behavior of Hybrid Metal Matrix Composites". Materials Science., 2005, 11 (3), 253-257.
36. Sahin, Y. and Ozdin, K., A model for the Abrasive Wear Behaviour of Aluminium based Composites, Materials and Design., 2008, 29,728-733.
37. Ravindran, P., Manisekar, K., Narayanasamy, P. and Narayanasamy, R., "Tribological Behavior of Powder Metallurgy-Processed Aluminium Hybrid Composites with the Addition of Graphite Solid lubricant". Ceramic International., 2013, 39, 1169-1182.
38. Rao, R. N., Das, S., Mondal, D. P. and Dixit, G., "Effect of Heat Treatment on the Sliding Wear Behavior of Aluminium alloy (Al-Zn-Mg) hard particle Composite. Tribology International", 2010, 43, 330-339.

[DOI: 10.22068/ijmse.14.2.41]

Iranian Journal of Materials Science and Engineering (IJMSE)

Instructions for Authors

Aims and Scope:
Iranian Journal of Materials Science and Engineering is published quarterly by the Iran University of Science and Technology (IUST), Iranian Metallurgical Society and Iranian Ceramic Society and publishes original scientific research papers in the broad area of Engineering Materials.

How to publish your article in IJMSE on line:
Go to the home page of IJMSE via the following link," ijmse.iust.ac.ir " and click the key provided for "Authors", and then click the key for" Authors' Guidelines", to see how to arrange and submit your article.
The language of the journal is English. Papers should deal with original research not previously published or being considered for publication elsewhere. Manuscripts should be submitted online along with a set of all original illustrations, photographs and drawings. The text should be typed using Word (version 6 and onwards) including tables and captions.

Types of Articles
Article will be published in the following categories:
1- Research Papers: A full paper must be subdivided into sections, e.g. Introduction, Experimental Procedure, Results, Discussion and Conclusion. The research papers including tables and figures should not exceed 15 pages.
2- Technical Notes: Short scientific notes, such as useful methods with special application in Materials Sciences and Engineering, or brief extension of a research/theory can be published as short notes. Abstracts and conclusion sections are compulsory.

Manuscript Organization
Cover Letter: Authors must prepare and submit, with their manuscript, a cover letter which includes the following information:

TITLE OF THE SUBMITTED MANUSCRIPT
•LIST OF ALL AUTHORS' NAMES AND AFFILIATIONS
•A VERY BRIEF (<100 words) DESCRIPTION OF THE ESSENCE OF YOUR APPROACH

The Text: Should be written in English, clearly typed (font size 11 points) and double-spaced throughout with at least 2.5 cm margins. All the pages should be consecutively numbered and Align text to the left. Authors should use abbreviated form of figure "i.e. Fig." within the text.
Main Text Headings: The manuscript should be divided as follow:
TITLE: A brief, descriptive, concise title of the article is required in capital letters.

FULL NAME OF AUTHORS AND THEIR AFFILIATION:
The name of the author(s) including academics (i.e. Students; lecturers and professors) or other professional affiliations should be appeared under the title, for example M. R. JAHANGIRI1, H. ARABI2, S. M. A. BOUTORABI3. The institutes' that the authors are affiliated should be addressed via the corresponding number appeared on the authors names after the authors names. Information's such as postal addresses and E-mails should be included for all of the authors. In addition telephone number and the fax number (If available) of the corresponding author to whom all correspondence will be sent must be given.
ABSTRACT: Abstract is a concise summary of the whole paper and should briefly states the objective, approach and gives the summary of results and conclusions drawn.
KEY WORDS: A list of 3-6 key words must be given under the abstract section.
GRAPHICAL ABSTRACTS:A Graphical Abstract is a single, concise, pictorial and visual summary of the main findings of the article. This could either be the concluding figure from the article or a figure that is specially designed for the purpose, which captures the content of the article for readers at a single glance. Please see examples below.
The Graphical Abstract will be displayed in online search result lists, the online contents list and the online article, but will not (yet) appear in the article PDF file or print.

Author instructions
A Graphical Abstract should allow readers to quickly gain an understanding of the main take-home message of the paper and is intended to encourage browsing, promote interdisciplinary scholarship, and help readers identify more quickly which papers are most relevant to their research interests.
Authors must provide an image that clearly represents the work described in the paper. A key figure from the original paper, summarizing the content can also be submitted as a graphical abstract.
Graphical Abstracts should be submitted as a separate file in EES by selecting "Graphical Abstracts" from the drop-down list when uploading files.
Specifications:
A Graphical Abstract should be a one-image file and should visualize one process or make one point clear. For ease of browsing, the Graphical Abstract should have a clear start and end, preferably "reading" from top to bottom or left to right. Try to reduce distracting and cluttering elements as much as possible.
Example 1:

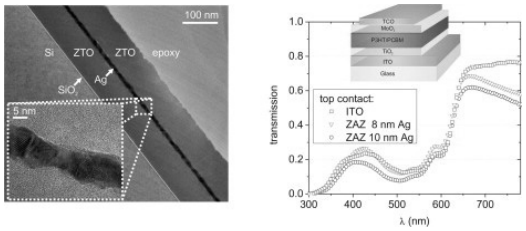

HIGHLIGHTS:
Highlights are a short collection of bullet points that convey the core findings and provide readers with a quick textual overview of the article. These three to five bullet points describe the essence of the research (e.g. results or conclusions) and highlight what is distinctive about it.
Highlights will be displayed in online search result lists, the contents list and in the online article, but will not (yet) appear in the article PDF file or print.
Author Instructions: Highlights should be submitted as a separate source file in EES (i.e. Microsoft Word not PDF) by selecting "Highlights" from the drop-down list when uploading files. Please adhere to the specifications below
Specifications:
Include 3 to 5 highlights.
There should be a maximum of 85 characters, including spaces, per highlight.
Only the core results of the paper should be covered.
Examples
Biochimica et Biophysica Acta (BBA), Bioenergetics, Volume 1807, Issue 10, October 2011, 1364-1369
Highlights
A conformational two-state mechanism for proton pumping complex I is proposed.
The mechanism relies on stabilization changes of anionic ubiquinone intermediates.
Electron-transfer and protonation should be strictly controlled during turnover.

INTRODUCTION
EXPERIMENTAL PROCEDURE
RESULTS AND DISCUSSION
CONCLUSIONS
ACKNOWLEDGMENT
REFERENCES:
All publications cited and used in the text should be addressed within the text and in the reference section. In the text, each reference should be given an appropriate number within a square bracket [ ] that it appears in the reference section. Abbreviation et al. should be used after the first author name for the references having more than one author in the text, but all the names should be given in the reference section. The list of references should be arranged numerically. References must consist of names and initials

[DOI: 10.22068/ijmse.14.2.41]

of all authors, title of paper referred to, abbreviated title of periodicals, year of the publication, volume number, finally the first and the last page numbers of the article.

REFERENCES REFERRING TO PAPER:
1. Davami, P, Praaq, W. V., Keizer, K., Ommen, J. G. V., Ross, J. R. H. and Burggraaf, A. J., Reactor Studies Using Vanadia Modified Titania and Alumina Catalytically Active Membranes for the Reduction of Nitrogen Oxide with Ammonia. J. Appl. Catal., 1991, 74, 249-251

REFERENCES REFERRING TO CONFERENCE PAPER:
2. Rigaud, M., Palco, S. and Wang, N., "Spinel formation in the MgO-Al_2O_3 system relevant to basic castables" Proceedings of the Unified Int. Tech.Conf.on Refractories (UNITECR '95), Kyoto, Japan, 1995, 387–392.

REFERENCES REFERRING TO BOOK:
3. Ulmer, G. C., Chromium spinel. High Temperature Oxides, Part I, Magnesia, Lime and Chromium Refractories, ed. A. M. Alper. New York, USA, 1970, 252–315

REFERENCES REFERRING TO NETWORK: TITLE, AUTHOR, WEB ADDRESS:
4. "Influence of Grain Phase on Slag Corrosion of Low Cement Castable Refractories", Sarpoolaky, H. and Lee, W. E., http://webmail.iust.ac.ir

REFERENCES REFERRING TO PATENT:
6. Smith, M. Hejazi, J and Golestani, F., Alumina-spinel monolithic refractory, USPatent 01716543988, 2009

TABLES AND TABLES' CAPTIONS: Tables should be typed double-spaced on a separate sheet and numbered consecutively with English numerals at the end of text. All tables should be keyed in to the text. A short descriptive caption should be given above each table and any footnotes and explanations underneath.

FIGURES AND FIGURES'S LEGEND: Figures should be numbered and keyed into the text. All the illustrations (photos, diagrams, schematics) must be submitted within the text with suitable resolution. Color figures cannot be accepted. All figures should be bright and clear. Please note that dark colors against a dark background cannot be reproduced well. Each graph should be prepared in Microsoft Excel program and then embedded to the text.

Copyright Transfer Agreement: Upon acceptance of an article by the journal, the author(s) will be asked to transfer the copy right of the article to the publisher on behalf of any and all co-authors, and must warrant that they are aware of and in agreement with all the contents of the article and consent to their names appearing on it. The copy right form is the last step of verification of your paper submission.

[DOI: 10.22068/ijmse.14.2.41]

[DOI: 10.22068/ijmse.14.2.41]